وزارة التعليم العالي و البحث العلمي

People's Democratic Republic of Algeria

Ministry of Higher Education and Scientific Research

جامعة سعد دحلب البليدة

SAAD DAHLAB UNIVERSITY OF BLIDA 1

Faculty of Sciences

Department of Physics

Laboratory of Theoretical Physics and Interaction of Radiation with Matter

DOCTORAL THESIS

Speciality**:** Fundamental and Applied Physics

Presented by

BENAROUS Samiha

THEME

Improving gamma spectrometry performance for accurate environmental measurements: Case of Algerian phosphate deposits.

Defended on September 25th, 2022

Approved by:

SIDOUMOU Mohamed	Professor, U. of Blida 1	President
IMADALOU Mourad	MCA, U. of Blida 1	Examiner
BELGAID Mohamed	Professor , USTHB	Examiner
KHELIFI Rachid	Professor, U. of Blida 1	Supervisor
AZBOUCHE Ahmed	MRA / Senior researcher , CRNA	Co-Supervisor
CHEGROUCHE Salah	Expert researcher, Head of CRND	Guest

Blida 2022

ملخص

يندرج هذا العمل ضمن إطار مشروع تعدين فوسفات وطني ضخم يتم تنفيذه بحلول عام 2020 في شرق الجزائر. تتميز رواسب الفوسفات عمومًا بتركيزات عالية من النويدات المشعة مقارنة بالمستويات الطبيعية. لذلك، يمثل قياس وقياسات اليورانيوم والثوريوم والبوتاسيوم مهمة حيوية لكل من المسح الإشعاعي ورسم خرائط النويدات المشعة لرواسب الفوسفات الجزائرية.

خلال هذا العمل، سيتم قياس النشاط الإشعاعي الطبيعي من خلال تقنية قياس الطيف غاما. من أجل قياسات دقيقة، يؤكد هذا العمل على تحسين أداء الكاشف من خلال تحسين القياسات باستخدام محاكاة مونت كارلو (MCNP). هناك حاجة إلى تحديد دقيق لكفاءة الكاشف لتحديد نشاط المصدر المشع بشكل موثوق. تم استخدام MCNP5 لإنشاء تكوين واقعي نموذجي لكاشف HPGe. تم تطوير إجراء كامل لتحسين متغيرات الكريستال مثل البعد النشط وسمك الطبقة الميتة، وبالتالي تحديد عوامل تصحيح الكفاءة. تم التحقق من صحة نموذج الكاشف من خلال مقارنة نتائج المحاكاة مع القيم التجريبية المقاسة للمصادر النقطية والمصدر المعد في المختبر. تم استخدام EDXRF في هذه الدراسة لتحديد التركيبة الأولية المدمجة في مدخلات MCNP.

تتم مقارنة كلتا النتيجتين اللتين تم الحصول عليهما من قياس النشاط الإشعاعي باستخدام كاشف HPGe والتركيب الأولي للقيمة التي تم الحصول عليها بواسطة تحليل تنشيط النيوترون الآلي (INAA) والتي يُقال إنها تقنية نووية أكثر حساسية وغير مدمرة وتستخدم عمومًا كطريقة مرجعية اختبار دقة الطرق التحليلية الأخرى. تم العثور على اتفاق عادل بين النتائج التي تم الحصول عليها بكلتا التقنيات النووية

من المتوقع أن تقوم نتائج هذه الدراسة بتقييم التوزيع الكلي لليورانيوم والثوريوم والبوتاسيوم في رواسب الفوسفات لاستراتيجيات الاستكشاف وتقييم الموارد وتنميتها المستدامة.

كلمات☐مفتاحية: مقياس طيف جاما. كاشف ؛ HPGe نجاعة؛ MCNP ؛ فوسفات؛ ED-XRF ؛ INAA ؛ مسح إشعاعي رسم خرائط النويدات المشعة.

Abstract

This thesis work falls within the framework of a national Phosphate mining megaproject implemented by 2020 in the eastern of Algeria. Phosphate deposits are generally characterized by enhanced radionuclide concentrations compared to natural levels. Therefore, Uranium, Thorium, and Potassium quantification and measurements represent a vital task for both radiological survey and radionuclides mapping of the Algerian phosphate deposits.

The natural radioactivity measurement will be accomplished through Gamma spectrometry technique. For accurate measurements, this work emphasizes the improvement of the detector performance via the optimization of configuration irradiation and measurements using the Monte Carlo (MCNP) simulation. Precise determination of detection efficiency is needed to determine reliably the activity of a radioactive source. MCNP5 was used to create a typically realistic configuration of the HPGe detector. A full procedure was developed to optimize the Crystal parameters such the active dimension, Dead layer thickness, and thus to define efficiency correction factors (coincidence summing effect…). The detector model was validated by comparison of simulated efficiencies with measured experimental values for point sources and extended source standard prepared in the laboratory. EDXRF has been employed in this study for the determination of the elemental composition introduced in the MCNP input.

The results obtained from the radioactivity measurement using HPGe detector are compared to the value obtained by Instrumental Neutron Activation Analysis (INAA) which is reported to be the more sensitive and non-destructive nuclear technique and generally used as a reference method to test the accuracy of other analytical methods. A fair agreement was found between results obtained with both nuclear techniques

The outputs from this study are expected to assess the total distribution of uranium, thorium and potassium in phosphate deposit for exploration strategies, resource evaluation and their sustainable development.

Keywords : Gamma spectrometry; HPGe detector; Efficiency; MCNP; Phosphate; ED-XRF; INAA; radiological survey; radionuclides mapping.

Résumé

Ce travail de thèse s'inscrit dans le cadre d'un mégaprojet national d'exploitation des phosphates mis en œuvre en 2020 dans l'est de l'Algérie. Les gisements de phosphate sont généralement caractérisés par des concentrations de radionucléides accrues par rapport aux niveaux naturels. Par conséquent, la quantification et les mesures de l'activité de l'Uranium, Thorium et du Potassium représentent une tâche vitale à la fois pour l'étude radiologique et la cartographie des radionucléides des gisements de phosphate algériens. La mesure de la radioactivité naturelle sera réalisée par la technique de spectrométrie gamma. Pour des mesures précises, ce travail met l'accent sur l'amélioration des performances du détecteur via l'optimisation la configuration de mesure à l'aide de la simulation Monte Carlo (MCNP). Une détermination précise de l'efficacité de détection est nécessaire pour déduire de manière fiable l'activité d'une source radioactive. MCNP5 a été utilisé pour créer une configuration typiquement réaliste du détecteur HPGe. Une procédure complète a été développée pour optimiser les paramètres du cristal tels que la dimension active du Crystal, l'épaisseur de la couche morte, et ainsi définir des facteurs de correction d'efficacité (effet de sommation de coïncidence…). Le modèle de détecteur a été validé par comparaison des efficacités simulées avec les valeurs expérimentales mesurées pour des sources ponctuelles et source étendue préparée au laboratoire. EDXRF a été utilisé dans cette étude pour la détermination de la composition élémentaire intégrée dans l'input MCNP. Les résultats obtenus à partir de la mesure de la radioactivité à l'aide du détecteur HPGe sont comparés à la valeur obtenue par l'analyse par activation neutronique instrumentale (INAA) qui est signalée comme la technique nucléaire la plus sensible et non destructive et généralement utilisée comme méthode de référence pour tester l'exactitude d'autres méthodes d'analyse. Un juste accord a été trouvé entre les résultats obtenus avec les deux techniques nucléaires.

Les résultats de cette étude devraient évaluer la distribution totale de l'uranium, du thorium et du potassium dans les gisements de phosphate pour les stratégies d'exploration, l'évaluation des ressources et leur développement durable.

Mots clés : Spectrométrie gamma ; détecteur HPGe ; Efficacité ; MCNP ; Phosphate ; ED-XRF ; INAA ; Surveillance radiologique ; cartographie des radionucléides.

Acknowledgements

I would like to thank God Almighty for giving me strength, wisdom and knowledge to work on this thesis.

Throughout the writing of this dissertation I have received a great amount of assistance and support.

Firstly, I would like to express my sincere gratitude to my supervisor, RACHID KHELIFI, Professor at Blida 1 university and my Co-supervisor AZBOUCHE AHMED, Senior researcher at CRNA. for their trust which allowed me to carry out this challenging research work in less than two years, for their continuous support, motivation, valuable consultations. I have been extremely lucky to have supervisors with unparalleled knowledge in the field, who cared so much about my work, and who responded to my questions and queries so promptly.

I would also like to thank my head of laboratory at the USDB 1, Professor SIDOUMOU, both for welcoming me to the Lpthirm laboratory, and for having done me the honour of chairing the jury of this thesis.

My deep gratitude addressed to Mr. BELGAID Professor at the Faculty of Physics of the USTHB, for accepting to judge this work and being part of the jury.

The expression of my deep respect are addressed to. Mr. IMADALOU, MCA at the USDB 1 for accepting to review this work.

I would also like to thank Mr CHEGROUCHE, expert Researcher/ and Director of the CRND for his support and for the honour he done to me by participation in this jury.

My appreciation goes to the CRNA-DAN team for accepting me into the research centre and for providing me with the opportunity to join their research group. Without their support, it would not have been possible to conduct this work.

Completing this work would have been all the more difficult were it not for the support and friendship provided by the members of the nuclear technique laboratory at CRNA, in particular A. ARABI and Z. MELZI, I am indebted to them for their help.

Words fail to express my gratitude to Mr. BOUMEHDI, engineer from CRND. At many stages in the course of this research project I benefited from his well knowledge in the field of geology.

Ralph Waldo Emerson

Enthusiasm is one of the most powerful engines of success. When you do a thing, do it with all your might. Put your whole soul into it. Stamp it with your own personality. Be active, be energetic, be enthusiastic and faithful, and you will accomplish your objective. Nothing great was ever achieved without enthusiasm.

Table of contents

Abstract

Acknowledgment

Table of contents

List of figures

List of tables

List of abbreviations

Figure List

Chapter IV

Table List

List of abbreviations

BEH   : Bled El Hadba

DL   : Dead layer

ED-XRF   : Energy Dispersive X-Ray Fluorescence

HPGe   : High Purity Germanium

INAA   : Instrumental Neutron Activation Analysis

NORM   : naturally occurring radio materials

Ppm   : part per million

SI   : international system

Introduction

The world is nowadays facing unprecedented economic challenges. Global energy demand is expected to rise by over 50 per cent by 2040 [1]. The extent of the ultimately recoverable natural resources is the subject of numerous researches worldwide [2]. Mining industry pursues to respond to the contemporary social objective of supplying the mineral raw materials that are required for economic development while reducing the ecological hazard. Phosphate deposits are deemed to be one of the world's most important non-renewable resources. Phosphorus-based minerals are mainly used in the manufacturing of P-based fertilizers [3], detergents, food and beverages as well as in metal treatment (coating). Elemental phosphorus is used as a process input to produce a wide array of phosphorus chemicals. Worldwide, more than 85% of the world's current production of phosphate ore is quarried from sedimentary deposits [4].

Algeria, third largest oil producer in Africa, and one of the main producers of phosphate, has been heavily involved in the development of its domestic phosphate exploitation, processing and production to meet both national and international demand [5].
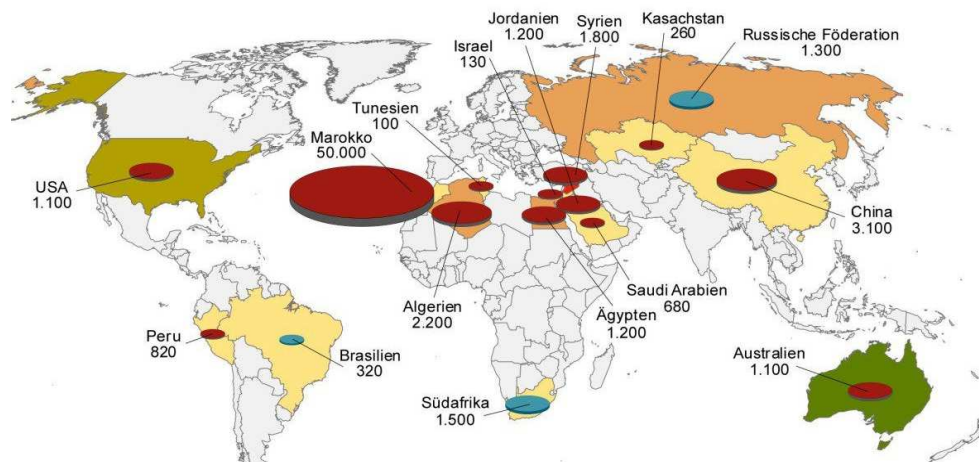
Figure 1.1. Distribution of phosphate minerals worldwide.

The Phosphate megaproject in Tébessa region was implemented by 2020 to boost Algeria's phosphate industry's competitiveness in global and continental markets. The ambition was significant enough to increase the national production of phosphates from 1 to 10 million tons per year. Algerian phosphate deposits have been formed during the upper Cretaceous-Eocene period, similarly to those of the Maghreb and the continental margin of the Arabian and the

African platforms [6,7]. The phosphate open-pit mining basin of Djebel Onk is located in eastern Algeria, next to the Algerian-Tunisian border. It contains five main deposits: Kef Es Sennoun and Djemi Djema deposits situated on the Southern anticline limb of the Djebel Onk anticline, the Djebel Onk Northern deposit situated on Northern anticline limb, Oued Betita and Bled El-Hadba deposits [7]. The latter is the subject of our study and is located at about 14 km to the East of the Djebel Onk anticline [6]. In the different Djebel Onk sedimentary phosphate deposits, several types of ores are often formed under different physico-chemical conditions [3,6].

Radioactivity in phosphate deposits has been investigated since the early 1900s. At those times, it was already known that phosphate deposits were normally characterized by higher radionuclide concentrations compared to natural levels [8,9]. Phosphate ore contains naturally occurring radioactive materials NORM, which may include primordial radionuclides such as uranium, thorium, their radioactive decay products, and potassium [10]. The concentration of uranium in phosphate ranges from 37 to 4,900 Bq kg^{-1} for ^{238}U and from 100 to 10,000 Bq kg^{-1} for ^{226}Ra. Concentration of natural radionuclides in phosphate samples differ from one sample to another depending on its chemical composition, its density, the collection site and the sampling depth [4, 11,12]. It is widely believed that the radioactivity associated to sedimentary phosphate increases with increasing P$_2$O$_5$ content, or is favoured by the adsorption and the co-precipitation of uranium with calcium [11]. Mining of phosphate, processing it into intermediate / end products, and the treatment of those products can all give rise to workers' occupational exposure issues [11,13].
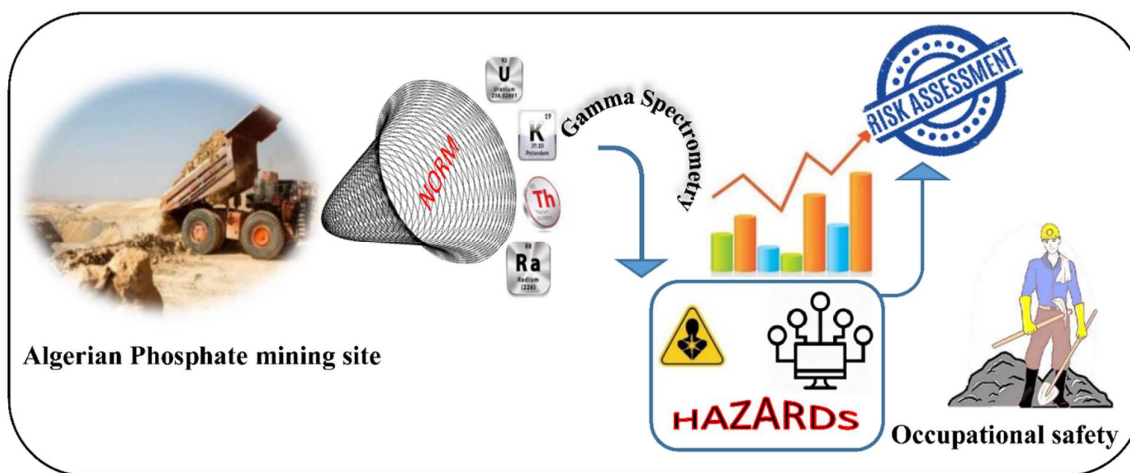
Figure 1.2. *Process of occupational exposure issues*

Establishing a baseline for radioactivity from radionuclides naturally enriched deposits, is important in the phosphate mining context in order to assess radiation doses to humans and to the environment during and after mining [10,14]. This information is particularly valuable in rehabilitation planning and developing closure criteria with regard to radiation protection purposes [9,15,16].

Due to the high penetration of photons, gamma spectrometry is of great importance in the detection and the measurement of natural radioactivity. High Purity Germanium (HPGe) based high resolution gamma spectrometry systems are extensively used for radioactivity analysis. This technique has an advantage over the other methods (such as alpha spectrometry, gross alpha counting, gross beta counting etc.), since it is non-destructive and does not require any pre-treatment. Also, the activity of numerous radionuclides can be determined simultaneously in any given sample. It is simple, fast and sensitive, but necessitates relatively large sample amounts and long spectrum acquisition time for low level radioactivity measurement [17]. The efficiency (FEPE) is a complex function characterized by the Ge detector (its dimensions and composition) and measurement conditions (composition and geometry of the source). There are several methods used for determination of FEPE, based on the energy of emitted gamma-rays and the sample geometry [18]. They can be realised by measurement of a "radionuclide standard" of similar geometry and gamma-ray energies as a studied sample, usually referred as a relative method. Nevertheless, the experimental determination of the response function of HPGe detectors presents some difficulties. It demands the availability of standards sources of a mix of radionuclide in the same counting geometry that the samples will be measured. Another difficulty is the peak sum effect, which is the occurrence of two or more photons interacting within the detector's crystal simultaneously. These events are common for isotopes that emit multiple gamma rays in a single event, especially when the radiation source is placed close to the detector [19]. These events affect the activity results and need to be taken into account. Another method for the FEPE determination is to use a commercially available software, which adopt semi-empirical approach combining advantages of both the absolute (detector characterization by Monte Carlo) and the relative (experimental comparison with known source) methods [20]. The Monte Carlo method is broadly used for photons and particles transport. It became a powerful tool, very flexible and enables the analysis of a wide energy range with quick FEPE calculation for any new geometry or matrix without a need of using additional standards. When applied together with a gamma spectrometry system, provides means to determine the

detector's response function, optimizing both time and financial resources and reducing the amount of radioactive wastes produced [21]. An accurate detector model should be developed in order to obtain good accuracy in the output of the calibration simulation. An important parameter in the detector model is the thickness of any absorber layer surrounding the germanium crystal particularly, the thickness of the inactive germanium layer, since this parameter has a large influence on the results of calibration simulations [22]. One of the major problems to overcome in any detector calibration simulation is the lack of accurate data regarding the germanium crystal as details of the detector geometry are usually not well known. In particular, the calculated efficiency is very sensitive to the thickness of the germanium dead layer; a layer of inactive germanium that is not useful for detection, but which strongly attenuates photons [22, 23]. The DL in p-type HPGe is formed by the diffusion of contact material, usually lithium atoms, into the germanium crystal, however, it cannot be simply identified as a depth of the Li-diffused layer. It is described as a layer consisting of the actual DL (charge collection efficiency is zero) and the partially active layer, or the effective DL (zone of the low charge collection efficiency). The thickness of this region depends on the Ge detector impurity level and diode production process; therefore, it can be different for each detector [24].

This work establishes a methodology and presents a detailed procedure for modelling a semiconductor HPGe co-axial detector using the MCNP5 Monte Carlo computer code. In this regards, primary calculations were performed to optimize detector parameters affecting the accuracy of the results. The validated model will be applied for the establishing of a first of kind NORM distribution in a non-exploited phosphate open pit mine (Bled El Hadba). Accordingly, this research is devoted as a systematic study by applying Kriging as a spatial interpolation method for generating original radionuclides distribution's maps in the BEH investigated deposit. This approach helps in scanning vast areas and in identifying zones with higher radiation levels, if any, and to define the associated potential radiological hazards. Also in this work, radioactive measurements acquired by the spectrometric gamma technique were subjected to statistical analyses for the sake of drawing a valid conclusion vis-à-vis the nature and the significance of the radioactive elements' distribution in Bled El-Hadba phosphate deposits. The information provided in this work will serve as the basis for creating a common understanding, and to assist regulatory bodies and industry operators in implementing a graded occupational health and safety approach for the protection of both the miners and the environment.

This thesis comprises of three primary research chapters and a summary discussing and outlining the conclusions and future work directions is then provided. The chapters are as follows:

Chapter 1: Theory. Provides a comprehensive review of the different type of Radiation matter interactions as well as neutron with matter, and brief introduction to radiation protection. theoretical bases necessary for understanding the radioactivity phenomena will be subjected. Also description of the various radiation detection methods based on semiconductor detectors, scintillators detectors will be provided.

Chapter 2: Methodology. Details all the nuclear technics employed throughout this research, including both practical and theoretical details.

Chapter 3: experiments and MCNP simulations. describes the radiometric measurements, experimental set-up and the methodology used in this study. As well as the Monte Carlo simulations approaches devoted to the study and evaluation of the germanium dead layer thickness after two decades of operation. Self-absorption and coincidence summing factors will be discussed. The experimental measurements will be confronted with the modeling calculations of the detection geometries by Monte Carlo. All the results are compared to the measurements by Instrumental neutron activation analysis as a technique of accuracy validation

Chapter 4: Application. The optimized model will be applied for the establishing of a first of kind NORM distribution in a non-exploited phosphate open pit mine (Bled El Hadba). Radioactivity of K-40, U-235, U-238, Ra-226 and Th-232 will be used to the assessement of radiological hazard in the area and then subjected to statistical analyses for the sake of drawing a valid conclusion vis-à-vis the nature and the significance of the radioactive elements' distribution in Bled El-Hadba phosphate deposits.

Conclusion and further work. This chapter provides a summary of the key findings and results achieved. Proposals for future work directions drawn from the thesis project are also outlined and considered.

Chapter I: Theory

The ways in which radiation interacts with the target are reflected both in the nature of the radiation itself and in the structure of atoms. This relationship between "projectile" and "target" was exploited by Rutherford (1911) when he used alpha particles as a radiation probe to investigate the structure of the atom. His work led to the discovery of the nucleus. This chapter will focus on the understanding of certain aspects of radiation penetration through matter by bearing in mind the special properties of the atomic target that is presented.

I.1. The sources of radionuclides and radiation

I.1.1. Primordial Radioactivity and Natural Sources of Radionuclides

primordial radionuclides, ^{40}K, ^{238}U and ^{232}Th are of importance due to their abundance and relative ease of detection and measurement through their daughter products and their characteristic gamma photon emission. The different geochemical and geophysical behaviour of these three radionuclides and their decay series makes them useful for characterising geological formations. Primordial radionuclides are those which appeared at the time of the formation of the Earth. As the Earth is about 4.7×10^9 years old, radionuclides with a half- life of 10^8 years or greater will still be present in measurable quantities. There are four transuranic decay series which are genetically independent, the thorium, uranium, neptunium and actinium series.

In the thorium series, the longest lived member is ^{232}Th with a half -life of 1.39×10^{10} years permitting it to occur naturally. ^{232}Th has a very long half- life and decays via alpha particle emission to ^{228}Ra. The decay of ^{228}Ra is via Beta emission and is rather weak and difficult to detect, being obscured by its daughter ^{228}Ac. ^{228}Ac decays rapidly (6.13 hrs) via a number of electrons and associated gamma rays to ^{228}Th. ^{228}Th is also a decay product through alpha decay of ^{232}U and electron capture of ^{228}Pa. The remaining members of the decay series are all short lived decaying via alpha particle decay to ^{212}Pb which is the longest lived member of the remaining decay series with a half-life of 10.64 hours. ^{212}Pb decays via Beta emission to ^{212}Bi of which 33.7 % decays to ^{208}Tl via alpha particle emission and 66.3 % decays to ^{212}Po via Beta emission [31] .

The Uranium series is the longest known series, starting with ^{238}U, and passing twice through Z=92 via an alpha and Beta decay sequence. ^{238}U has a long half -life of 4.47×10^9 years which permits it to exist naturally today and its abundance is 99.27 %. ^{238}U emits alpha particles only. Beta emission is introduced by the immediate daughters of ^{234}Th and ^{234}Pa. 98% of the ^{234}Pa decays directly to the ground state of ^{234}U, whilst the isomer of ^{234}Pa exhibits a complex Beta, and conversion electron spectrum. A series of four alpha emissions follows through ^{230}Th, ^{226}Ra, ^{222}Rn and ^{218}Po. The next series of decays occurs via a mixture of alpha and Beta decays and predominates through ^{214}Pb, ^{214}Bi, and rapidly reach equilibrium with ^{222}Rn.

Among all the other long lived primordial radionuclides occurring in nature, ^{40}K is the only one which exists in abundance and is readily detectable through its gamma emissions. 11%

of ^{40}K decays to ^{40}Ar via β^+ with 1.46 MeV gamma ray emission and 89% decays to ^{40}Ca via β^- decay.

I.1.2. Anthropogenic Radionuclides

In terms of global pollution, the radionuclides, such as ^{137}Cs, introduced into the atmosphere from weapons testing during the late decades, when the majority of weapons testing took place above the ground, are likely to have been the most significant contribution to environmental radioactivity levels. However, incidents such as Chernobyl created pollution levels which are important on a continental scale, with some fractional contribution to worldwide levels. Anthropogenic radionuclide releases into the environment are distributed through natural atmospheric, erosional and tidal processes. Subsequent depositional patterns may be characteristic of whichever environmental processes and pathways predominate.

^{137}Cs also formed as a consequence of fission within nuclear reactors and forms from the decay of ^{137}Xe which decays with a half-life of 3.82 min to ^{137}Cs via beta particle emission and a complex series of low yield gamma-rays. ^{137}Cs itself decays via beta particle decay of which 85.21 % of the decays result in a gamma ray of energy 661.165 keV.

I.1.3. Radioactive decay modes

The radioactive decay is a spontaneous change within the nucleus of an atom which results in the emission of particles or electromagnetic radiation. The rate of decay or transformation of a radionuclide is described by its activity. The unit of activity is the Becquerel (Bq), defined as one disintegration per second. The activity of a pure radionuclide decreases exponentially with time. If N represents the number of atoms of a radionuclide in a sample at any given time, then the change dN is the number during a short time dt, is proportional to N and to dt. The probability that a given nucleus will decay per unit time is called the decay constant λ. If λ is taken as the constant of proportionality then:

$$\frac{dN}{dt} = -\lambda N \tag{I.1}$$

The solution of this equation is:

$$N(t) = N_0 e^{-\lambda t} \tag{I.2}$$

where N_0 = number of atoms at t = 0. One concept used extensively with radioisotopes in the half-life $T_{1/2}$ ($T = \frac{\ln 2}{\lambda}$), defined as the time it takes for half of a certain number of nuclei to decay.

$$A = \lambda N = A_0 e^{-\lambda t} \tag{I.3}$$

The units of activity are the Becquerel (Bq), equal to 1 decay/s, or the Curie (Ci) equal to 3.7 x 10^{10} Bq. The Becquerel is the SI unit. The term specific activity (A_s) is used frequently. It may have the following meanings in case of solid matter:

$$A_s = \frac{A}{m} \; (^{Bq}/_{kg}) \tag{I.4}$$

I.1.4. Radioactive equilibrium

The transition from the excited to the low excited ground creates a nuclear equilibrium whereby the ratio of the father to the daughter will be constant. The radioactive equilibrium is not established immediately, but it only takes place after a transition period. Moreover, there are two types of nuclear equilibrium that can be distinguished. Firstly, it consists of transient equilibrium that occurs when the half-life of the parent is only a few times greater than the half-life of the daughter, the condition of transient equilibrium will occur [25,26]. During the period of interest, the parent will undergo radioactive decay. Daughter activity will build and establish a state of equilibrium with the parent activity. This type of equilibrium is applied in medical imaging. Transient equilibrium differs from secular equilibrium. The latter assume that the radioactive material is forming at an almost constant rate. Radioactive nuclei undergo transitions at exactly the same rate they are forming, and a condition of equilibrium is established. The amount of radioactive material will then remain constant regardless of elapsed time. Under this condition, the activity is equal to the rate of formation and is referred to as the saturation activity. The important point is that the maximum activity of a radioactive material is determined by the rate (nuclei per second) at which the material is being formed. Although it is true that the activity gradually builds with time, a point is reached at which build-up stops and the activity remains at the saturation level.

I.2. Interaction of radiation with matter

The majority of the radioisotopes emit gamma rays, with a variety of energies and intensities. In the appropriate conversion medium of the detectors three mechanisms are possible: the photoelectric effect, the Compton effect and the pair production [25].

From Figure I.1, it can be seen that low energy photons interact mostly via the photoelectric effect, while the intermediate and high energy photons interact through Compton and pair production effects respectively.
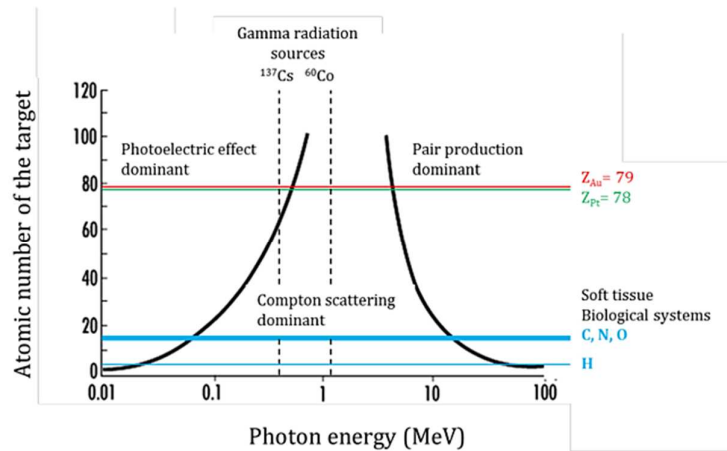
Figure I.1. *Processes involved in the interaction of photons with matter as function of the incident energy and atomic number of the target.*

These interaction mechanisms are described in detail in the following sections.

I.2.1. Photoelectric effect

In the photoelectric effect the incident photon interacts with the atom of the absorber material. The incident photon gets absorbed and at the same time an electron is emitted from one of the bound shells. The emitted electron is also known as photoelectron [25]. An empty space is created due to the ejection of the photoelectron but it is filled very quickly, in an order of time of picoseconds, either by a free electron or by electrons from other shells of the atom.

The latter method is the mechanism behind the creation of characteristic X-rays. The photoelectric process is the dominant way of interaction for photons belonging to the low energy domain. Furthermore, it is also prevalent for high atomic number (Z) materials.
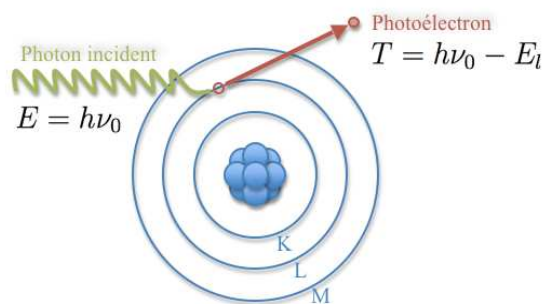
Figure I.2.*Photoelectric effect*

The kinetic energy of the outgoing electron is given by :

$$E = E_v - E_l = h\nu - E_l \tag{I.5}$$

Where E_v is the energy of incoming photon, E_l is the binding energy of the electron. The photoelectric effect is the phenomenon that is more of interest for this thesis, since it is the main effect that is being taken advantage of, inside a semiconductor, which is going to be analysed in more detail in next sections.

I.2.2. Compton effect

In the Compton scattering the incident photon gives only part of its energy to the electron (also known as recoil electron) of the absorber atom.
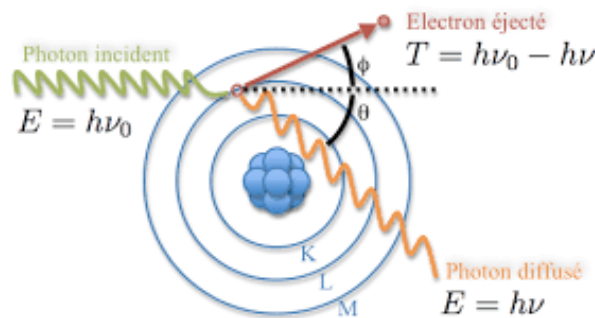
Figure I.3. Compton effect

Classical electromagnetic theory is not able to describe the inelastic component that was observed when electromagnetic radiation was scattered by charged particles. Compton and Debye independently formulated the relationship between the wavelength and the scattering angle of radiation that was impinging on not bound, stationary electrons [26]. The scattered photon energy is given by the following formula:

$$E_\gamma{'} = \frac{E_\gamma}{1+\frac{E_\gamma}{m_0 c^2}(1-\cos\theta)} \tag{I.6}$$

where θ is the angle from the incoming photon's path which has energy E_γ. The new photon is emitted after the collision of the initial photon with the electron of the atom with energy equal to $E_\gamma{'}$. m_0 stands for the electron mass and c stands for the speed of light.

I.2.3. Pair Production

In the pair production mechanism the incident γ ray photon produces a pair of an electron and positron. For this purpose, the incident γ ray photon has to exceed at least twice the rest-mass of an electron which is equal to 1.022 MeV.
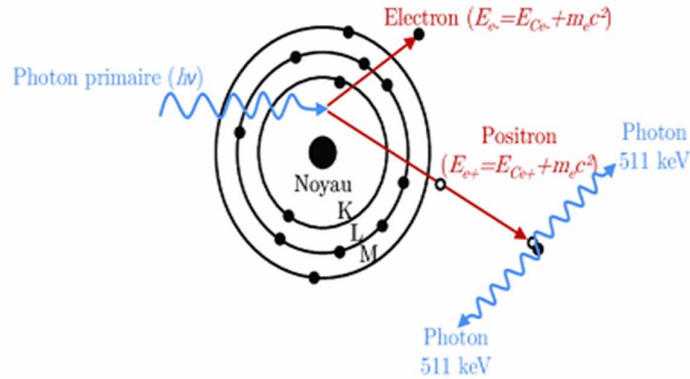
Figure I.4. Pair production

 For the produced positron usually the case is that it will annihilate with an electron in the detector material. Thus, two γ ray photons of 0.511 MeV each will be created. The produced electron on the other hand will travel through matter until it loses entirely its kinetic energy via ionization, electron excitation, or bremsstrahlung radiation

I.2.4. Photon beam attenuation

The absorption of photons in matter depends on the nature of the medium and the energy of the incident photons. It is expressed as a function of an attenuation coefficient μ which represents the fraction of incident photons interacting per unit length [29]. This coefficient takes into account the cross sections of the four interaction processes described above.

For an incident beam of intensity I_0, the intensity of photons I passing through a material of thickness x without interaction, is given by:

$$I = I_0 e^{-\mu x} \tag{I.7}$$

$$\mu = n\sigma_{tot} = \frac{\mu}{\rho} = \frac{N_A}{A_M}(\sigma_{Co} + \sigma_{Ph} + \sigma_{pp}) \tag{I.8}$$

A_M: is the atomic number of the element. σ_{Co} Compton cross section , σ_{Ph} photoelectric cross section, σ_{pp} pair production cross section.

I.3. Interaction of Neutron with matter

The neutron is a fermion-type particle with spin s=1/2, it is also an electrically neutral particle with a mass heavier than the mass of the electron and comparable to that of the proton. Its mass at rest is equal to mc^2 =939.56 MeV.

I.3.1. Neutron Sources and Classifications

Neutron sources fall into two main categories. The first category is isotopic and includes (a, n), fission; the second covers neutron generators. The most practical neutron source is a nuclear reactor, which produces neutrons via the nuclear fission process.   Neutrons originate in the active part of the reactor core and neutron emission occurs through thermal nuclear fission with certain heavy elements in which the generated compound nucleus is split into smaller parts through a neutron penetration and capture [27]. Each fission process generates fission fragments (lighter nuclei), two or three free neutrons, a number of gamma rays and neutrinos whereas most fission energy is distributed to the fission fragments. Free neutrons from fission reaction can then initiate further nuclear interaction and the fission fragments undergo nuclear decay producing additional radioactive products. Emitted neutrons in a fission process have a distribution of kinetic energies from 0 to 14 MeV.

Neutrons are classified according to their energies because (i) the type of neutron interaction with the matter is energy dependent and (ii) energy-dependent cross sections are needed to calculate the reaction rate. In general, the energy of neutrons existing in a reactor core is divided in three regions: thermal, epithermal and fast region. The most common classification is shown in table II.1.

Table II.1. Neutron characterization according to energy range

Type of neutrons	Energy range
Thermal	$< 0.5 \ eV$
Epithermal	$0.5 - 10 \ keV$
Intermediate	$1 \ - 100 \ keV$
Fast	$0.1 \ - 20 \ MeV$
Very fast	$> 20 \ MeV$

 Ultra cold neutrons are totally reflected at any incident angle on any material and cold neutrons are reflected at an optimum incident angle. After a number of collisions with nuclei in a medium, neutrons arrive at the thermal energy level, provided that they are not absorbed.

Thermal neutrons often have much larger effective cross sections than fast neutrons and are important for activity calculation. Fast neutrons with a kinetic energy level up to 20 MeV are produced by nuclear fission with a mean energy of 2 MeV and by nuclear fusion which is not discussed in this work. Fast neutrons can be transformed into thermal neutrons via moderation [27]. Neutrons are chargeless particles that interact either in the form of scattering or through a nuclear reaction with a nucleus in the material. The kinetic energy of the neutron plays an important role in the interaction process. The neutron interactions create charged particles or γ rays which in turn can be detected by a detector.

I.3.2. Neutron Interaction with Matter

In contrast to emitted gammas, which mainly interact with the electrons in the shell, the neutron interacts only with the nuclei of the surrounding atoms or molecules in the form of absorption or scattering. They pass through the atomic electron cloud and interact directly with the nucleus.

With the interaction process, a compound nucleus is formed through incident neutrons and target nucleus [28].

Scattering process

In the case of the scattering process, neutrons change direction and energy, and continue along another straight line. The nucleus is either left in the ground state (elastic scattering) or in an excited state (inelastic scattering).

Absorption processes

By absorption processes neutrons cease to exist and the whole energy of the neutron is dissipated by the collision. During neutron absorption free neutrons are captured by a nucleus, causing a nuclear reaction and converting the atom into another isotope. The out coming nuclide is often an unstable isotope which can decay immediately or with a certain half- life into another nuclide. As a result of the des-excitation of an unstable radionuclide generated by neutron absorption, various secondary particles such as gamma- photons or beta particles are emitted. Different types of neutron absorption are of importance for the calculation of material activation and consequently significant for the existing work.

Radiative Neutron Capture (n, γ)

In general, thermal neutron capture (absorption of a neutron) or radiative capture is the most important type of activation reaction since they efficiently utilize neutrons in a neutron field. In this reaction an isotope of mass A captures a neutron to produce a compound nucleus of mass A+1. The newly formed and excited nucleus subsequently decays by emitting a cascade of high-energy gammas

$$\,^1_0 n + \,^A_Z X \rightarrow \,^{A+1}_Z X + \gamma \tag{I.9}$$

For each type of nuclear reaction, in general scattering and absorption, and each type of nuclide a microscopic cross section can be defined, so that the total microscopic cross section [14] is determined as:

$$\sigma_t = \sigma_{scattering} + \sigma_{absorption} \tag{I.10}$$

The radiative capture cross section varies for a large number of nuclides as the inverse square root of incident neutron energy.

I.4. Radiation Detectors

The detection and quantification of radionuclides present in a source is dependent upon the detection of gamma photon energy and the relative abundance of these photons. The detection of gamma rays is critically dependent upon the gamma ray photon undergoing an interaction that transfers all or part of the photon energy to an electron in the absorbing material. Thus, to serve as a gamma ray spectrometer, a detector must act as a conversion medium in which incident gamma rays have a high probability of interacting to yield one or more fast electrons and at the same time act as a detector for these secondary electrons. There are principally two detectors of major importance in the detection of gamma rays: i) inorganic scintillators, such as sodium iodide thallium activated crystals (NaI(T1)); and ii) solid state semiconductors such as the hyper pure germanium (HPGe). NaI(T1) detectors have a higher sensitivity but poorer energy resolution than HPGe detector. Hence, the choice of gamma detector is based upon: i) the required resolving power; ii) the detector efficiency; and iii) the simplicity of the arrangement. Relative efficiency comparisons between detector types are often made by comparison with the intrinsic efficiency of a 3" x 3" NaI(T1) detector at 1333 keV (^{60}Co) [26-28].

I.4.1. Semiconductor (Solid State) Detectors.

The principle of semiconductor detectors is based on the semiconductor energy band gap principle, where electrons in the valence band are excited by ionization and cross the forbidden band to the conduction band and are subsequently collected by the influence of an electric field. Germanium (Ge) is the preferred material for this because of its high Z. Highest purity Ge was typically p-type (excess of holes) which could be effectively neutralised by the ion drift method, where lithium (valency 5) was drifted through Ge (valency 4) to provide a compensated (intrinsic) layer. This process was carried out in different geometries to provide coaxial open ended or single ended detectors. To avoid the redistribution of Li, these detectors are maintained at temperature of 77 K. Today germanium is available at very high purities, and reverse biasing at 1000 V or more provides a depletion zone (intrinsic) of 10 mm or more providing high purity germanium. The impurities which remain still cause excess leakage current and hence still require the detectors to be operated at liquid nitrogen temperatures. The detector is mounted in a vacuum chamber which is attached to or inserted into a LN_2 Dewar. The sensitive detector surfaces are thus protected from moisture and other contaminants.
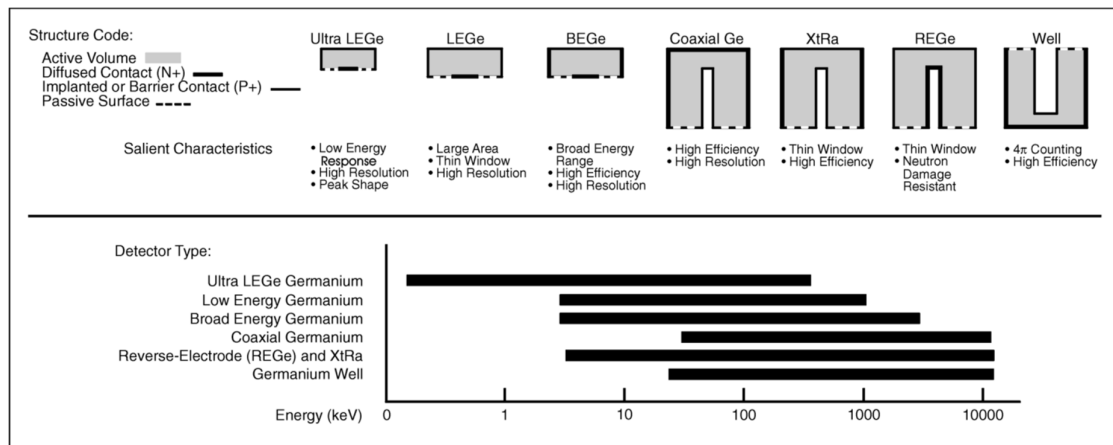
Figure II.5. Detector Geometries

A wide variety of detector types which are described in Figure 1 illustrates the various detector geometries that are available.

Ultra-LEGe detector extends the performance range of Ge detectors down to a few hundred electron volts, providing resolution, peak shape, and peak-to-background ratios once thought to be unattainable with semiconductor detectors. The Low Energy Germanium Detector (LEGe) offers major advantages over conventional planar or coaxial detectors in many applications. The LEGe detector is fabricated with a thin contact on the front face.

Since preamplifier noise is a function of detector capacitance, the LEGe affords lower noise and consequently better resolution at low and moderate energies than any other detector geometry. Unlike grooved planar detectors, there is virtually no dead germanium beyond the active region. This, and the fact that the side surface is charge collecting rather than insulating, results in fewer long-rise time pulses with improved

count rate performance and peak-to-background ratios. the LEGe is usually equipped with a thin Be window [29].

The conventional coaxial germanium detector is often referred to as Pure Ge, HPGe, Intrinsic Ge, or Hyper pure Ge. Regardless of the superlative used, the detector is basically a cylinder of germanium with an n-type contact on the outer surface, and a p-type contact on the surface of an axial well. The germanium has a net impurity level of only about 10^{10} atoms/cm^3 so that with moderate reverse bias, the entire volume between the electrodes is depleted, and an electric field extends across this active region. Photon interaction within this region produces charge carriers which are swept by the electric field to their collecting electrodes where a charge sensitive preamplifier converts this charge into a voltage pulse proportional to the energy deposited in the detector. The n and p contacts or electrodes are typically diffused lithium and implanted boron respectively. The outer n-type diffused lithium contact is about 0.5 mm thick. The inner contact is about 0.3 microns thick [29].

I.4.2. Scintillation Detectors

Interaction of radiation with a scintillator detector crystal can result in an electron being elevated from the valence band to the conduction band, thus leaving a hole in the valence band. In a pure crystal such as NaI, the return of the electron into the valence band is an inefficient process and results in the emission of a photon, a condition known as scintillation. However, typical forbidden band widths in pure crystals lead to resulting photon emissions with too high an energy to lie within the visible region. To enhance the probability of visible photon emission during the des-excitation process, small amounts of an impurity or "activator" such as thallium (Tl) are commonly added to the inorganic scintillator. The impurities create energy states within the forbidden band through which the electron can de-excite back to the valence band. Thus the transition is less than the full forbidden band gap, and the transition will give rise to a visible photon which forms the basis of the scintillation process [30].

NaI(Tl) has the highest light yield of all known scintillation materials. It has a linear response to electrons and gamma rays. Although NaI(Tl) can be easily machined into required sizes and

shapes, it is fragile and easily damaged through mechanical and thermal shocks and is also hygroscopic. The light collection from a scintillator must be as efficient as possible and be reflected towards the photomultiplier tube which converts the light signals into electrical signals. To achieve this, the scintillator must be as transparent as possible and surrounded by a reflector usually graded MgO powder. The highest light transfer between crystal and photomultiplier tube is achieved through direct coupling. The photomultiplier consists of two electronic systems mounted within the same unit: i) a photosensitive cathode which converts the photons into photoelectrons; ii) a multiplicator tube where the electrons are repeatedly multiplied by secondary emission from dynodes [30].

I.5. Detector operational characteristics

I.5.1. Energy resolution

The energy resolution of a detector expresses its ability to separate two neighbouring energy lines. In the case of a gamma spectrum, the effect of the resolution of a detector clearly appears on the shape of the spectrum, in particular on the total absorption peak. We then define the resolution of a detector by:

$$R\% = \frac{FWHM}{E} * 100 \tag{I.11}$$

FWHM is the width at half height of the corresponding peak.

I.5.2. Detection efficiency

The detection efficiency is one of the most key energetic characteristics for radiation measurement. When incident radiation is detected, a fraction of it can pass through the sensitive volume without interacting with the detector due to the nature of the radiation or the type of detector. Under these conditions, it is necessary to define the detection efficiency (absolute efficiency ε_{abs} or of the intrinsic efficiency ε_{int}).

The absolute efficiency represents the number of radiations detected on the number of radiations emitted by the source, it is defined by the following relation:

$$\varepsilon_a = \frac{\text{number of radiations detected}}{\text{number of radiations emitted}} \tag{I.12}$$

The intrinsic efficiency is defined by the number of radiations detected over the number of radiations having penetrated the detector; according to the following equation

$$\varepsilon_i = \frac{\text{number of radiations detected}}{\text{number of radiations penetrated the detector}} \tag{I.13}$$

The number of rays having penetrated the detector is obtained by calculating the source-detector geometry and from the number of rays emitted by the source. This geometry defines the solid detection angle Ω. The relationship between the two absolute and intrinsic efficiencies is:

$$\varepsilon_i = \varepsilon_a \frac{4\pi}{\Omega}$$
(I.14)

In the case of a point source located at a distance (d) on the axis of a cylindrical detector of radius (a), the solid angle of detection is given by the following relation:

$$\Omega = 2\pi \left(1 - \frac{d}{\sqrt{d^2 + a^2}}\right)$$
(I.15)

The response of the detector as a function of the energy of the incident radiation can be characterized by its efficiency. Knowledge of this response is very important for quantitative radiation measurements.

Chapter II
Nuclear Analysis Techniques

Having reviewed in chapter 2 the interaction of radiations with matter. This chapter discusses the traditional techniques used to measure environmental radioactivity. A wide range of measurement techniques is available today for the scientist to determine levels and distributions of environmental radioactivity. This chapter discusses the broad theory and methods behind the three techniques used for the measurement of environmental radioactivity, through gamma spectrometry, neutron activation analysis and X-ray fluorescence as techniques frequently used for monitoring aspect.

II.1. Gamma ray Spectrometry

Gamma spectrometry is one of the most powerful radiometric techniques available. The non-destructive method enables both quantitative determination and identification of the majority of radioisotopes. Compared to other radiometric techniques, it has a great advantage in being able to detect minor isotopes, even in the presence of a large background from a multitude of other radioactive elements without any need for separating the isotopes [6,28]. This has enabled the technique to be used as the standard tool in nearly all disciplines where radioisotopes are analyzed. The technique plays an important role in environmental radioactivity, nuclear safety and reactor monitoring, nuclear medicine, geology.

II.1.1. Instrumentation for Gamma spectrometry based HPGe Detectors.
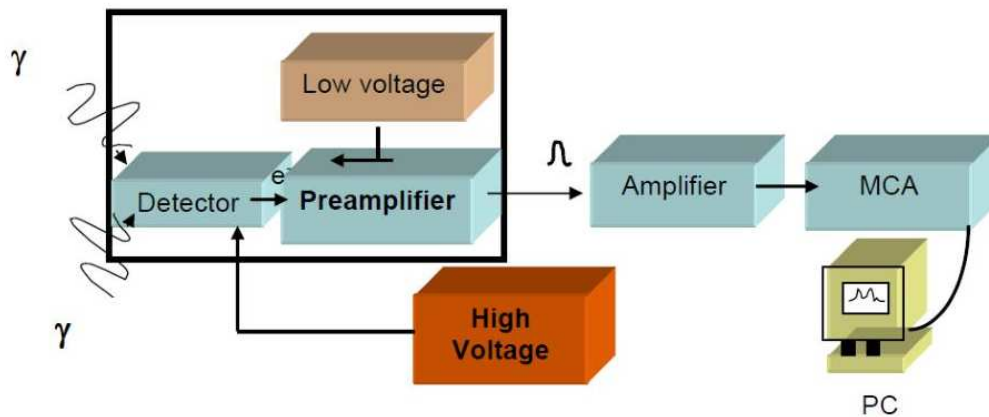
Figure II.1.The Main Components of a Gamma spectrometry system

Electronics

The nuclear electronics required to power semiconductor detectors and process their signal information are usually housed within a Nuclear Instrument Module (NIM) Bin which also acts as an ac to dc converter. The primary interconnections between modules and components are carried out using shielded coaxial cables. The shielded construction is designed to minimize pick-up of noise from stray electric and electromagnetic fields, which is of paramount importance with signal cables. The high voltage or detector bias is commonly up to 5000 volts. Extreme stability is not required as fluctuations in the voltage supply do not lead to changes in photopeak position.

Amplifiers

Amplifiers contain pulse shaping networks and amplify the signal from the detector. Their location with respect to the detector can affect the signal to noise ratio. Thus the amplifier is divided into two. The first part or preamplifier is placed close to the detector which minimizes the capacitive load on the detector. In addition, the preamplifier provides a high impedance to the detector whilst providing a low impedance output to drive successive components. The output signal is typically a pulse with an exponential tail. The rise time of the output is kept as short as possible, usually equal to that of the charge collection time on the detector itself. It is through this process that the preamplifier maximises the signal to noise ratio. The main part of the amplifier, is positioned further away along with the rest of the nuclear electronics required. The amplifier must allow for the selection of the optimal pulse shaping network for an optimum resolving power consistent with the noise characteristics for a given detector preamplifier combination at one end, and the practical count rate requirements for experimental conditions at the other. This flexibility is taken into account with commercially available amplifiers with pulse shaping methods and RC time constant adjustable over a range of 0.1 to 10 [is. This allows the ready selection of the best signal to noise ratio. For high counting rates a delay line differentiation circuit or second RC circuit should be provided. The amplifier accepts tail pulses as an input and produces a shaped linear pulse with standard polarity and span. The amplification factor or gain required varies greatly with application, but is typically a factor of between 100-5000. This gain can be adjusted and if the product of the input and gain exceeds the maximum designed output amplitude, the amplifier will saturate and produce a distorted output pulse. Linear amplification will only be realised for those pulses which are short of this saturation level. An additional requirement for high resolution gamma spectroscopy is base line restoration between pulses at high counting rates to reduce the signal to noise ratio and the deterioration in the photo-peak resolution [28].

Signal Processing and Output

The output pulses from the amplifier are converted to a digital number by an Analogue to Digital Converter (ADC). The digital number is proportional to the amplitude of the pulse at the input to the ADC. The performance of the ADC is characterised by the speed of the conversion, the linearity of the conversion and the resolution or fineness of the conversion. The resolution depends upon the number of channels the ADC can subdivide into. The stability of the ADC must be such as to ensure that a pulse of constant amplitude will be stored in a certain single channel. The ADC forms a key part of the Multi-Channel Analyzer (MCA) and

determines its performance. The MCA is a device used for recording and storing data which is then used for displaying pulse height distribution measurements or spectra. The number of channels available is usually a power of 2. By providing a large number of channels, the width of one channel can be made very small and the resulting discrete spectrum will be a close approximation to the continuous distribution. Therefore, if at least 4 channels are required to be over the Full Width Half Maxima (FWHM), one would require at least 100 channels for a detector with a 4% energy resolution. Similarly, for an energy resolution of 0.4%, 1000 channels are required. Once a pulse has been processed by the ADC, the analyzer control circuits seek out the memory location corresponding to the digitised amplitude stored in the address scaler, and the location is incremented by one. A plot of the content of each channel (number of pulses) versus the channel number will be the same representation of the differential pulse height distribution of the input pulses. Inevitably, during times of high count rate, some fraction of the input pulses will be lost to dead time. Hence, any attempt to quantitatively measure the number of pulses presented to the analyzer must take into consideration the dead time.

Digital Spectrum Analyzer (DSA 1000)

The DSA-1000 is a full included 16K channel integrated Multichannel Analyzer based on advanced digital signal processing techniques (DSP). When connected with the computer of choice, the DSA-1000 becomes a complete spectroscopy workstation, capable of highest quality acquisition and analysis. The device interfaces to all existing detector technologies. Unlike conventional systems, which digitize the signals at the end of the signal processing chain, the DSA-1000 digitizes the preamplifier signals at the front of the signal processing chain. This approach minimizes the amount of analog circuitry resulting in increased stability, accuracy and reproducibility. The DSA-1000 is operated through the Genie 2000 spectroscopy software which provides the user with ultimate flexibility.

II.1.1. Spectral characteristics

the spectral characteristics are consequences of radiation scattering within the detector. The photo-peak or full energy peak is the result of primary (unscattered) photons interacting wholly with the detector crystal resulting in complete absorption. The width of the photopeak is usually described in terms of the *full width at half maximum* (FWHM) and determines the energy resolving characteristics of the detector. The size of the photopeak is a function of source geometry as well as upon the size of the detector. The smaller the detector, the fewer the number

of photons interacting wholly with the crystal, resulting in a larger scattered Compton contribution to the spectrum.
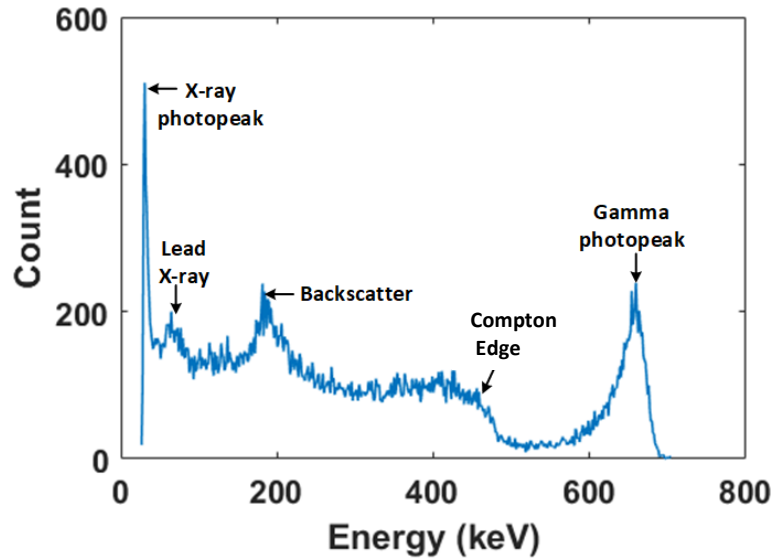
Figure II.2. *Schematic representation of gamma ray spectrum observed from a pure 137Cs [26]*

The Compton continuum is made up of the Compton edge, the back-scatter peak and the accumulation of photons which have undergone many scattering events. The Compton edge is in a characteristic position away from the photopeak. It represents the maximum possible energy an electron can possess after a single Compton interaction within the detector crystal or can. The shape of the continuum is also characteristic of the detector material. If the mean free path of a photon is much greater than that of the dimensions of the crystal, then the photo fraction (photopeak area/total area) will be very small. If the detector crystal is large compared to the photon mean free path, then the photo fraction will be larger.

Thus the size of the photo peak and Compton continuum is also a function of crystal size. When pair production is prevalent (ie. photon energy > $2m_0c^2$), a double escape peak will develop at a point (hv - $2m_0c^2$) in the spectrum of small detectors because of the escape of both annihilation photons without further interaction. If one of these annihilation photons is totally absorbed, this will result in a single escape peak at (hu -m_oc^2) [28, 29]. Other factors can complicate the spectral response characteristics, and these are summation effects and effects of surrounding materials. Summation effects are additional peaks caused by the coincidental interaction and detection of two or more gamma ray photons. This can be caused by: i) isotopes which emit multiple cascade

gamma rays in which the life time of the intermediate state is so short that they are emitted in coincidence and deposit their energy in the detector in a time that is short compared with the response time of the detector, ii) the accidental combination of two separate events in a time that is short compared to the resolving time of the detector. This chance coincidence increases with increasing counting rate. The summed peak from these two possibilities will be observed in the spectrum at a point which coincides with the sum of the two individual gamma-ray energies. The size of the sum peak will have an intensity proportional to the square of the counting rate. A continuum will also develop due to partial interactions with the detector. The backscatter peak is a consequence of scattering within the source, air path and can around the detector crystal. As the scattering angle increases there is a tendency for the resulting photon energy interacting with the detector to tend towards 180-200 keV, irrespective of the original primary photon energy [32].

II.2. Instrumental Neutron Activation Analysis

Von Hevesy and Levy (1936) proposed Neutron Activation Analysis (NAA) for the analysis of dysprosium in rare earths using an isotopic neutron source. Since this historical experiment, NAA has been developed as a highly valuable analytical technique, especially with the advent of nuclear reactors. Nuclear reactors offer high neutron fluxes so that extremely small quantities of a large number of elements can be determined at a time.

Today INAA is widely applied in biomedical, environmental, industrial, geological and archaeological fields. Due to its sensitivity, precision and accuracy it is considered an ideal method for the determination of a large number of trace elements in several materials.

II.2.1. Principle and theory

Instrumental Nuclear Activation Analysis techniques include those methods that use nuclear reaction to form product radionuclides or excited states of the target nucleus as the basis for analytical determination. In this process, an element is bombarded with neutrons an excited intermediate element is formed.

$$\ _{Z}^{A}X + \ _{0}^{1}n \rightarrow \ _{Z}^{A+1}X^* \rightarrow \ _{Z}^{A+1}X + \gamma$$
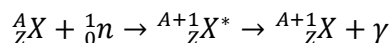
The radioactive product may decay via alpha, beta, delayed neutron emission processes. All these may be accompanied by gamma emission. The gamma rays emitted in the delayed neutron emission process may be known as delayed gamma rays. The qualitative characteristics of INAA are the energies of the emitted γ-rays (E) and the half-life of the nuclide ($T_{1/2}$) while the

quantitative characteristic is the intensity (I), which is the number of γ quanta of energy E measured per unit time [28].

When irradiating a sample in a reactor, the reaction rate (n, γ) per nucleus (in s-1) is given by:

$$R_0 = N_0 \int_0^\infty \Phi(E)\sigma(E)dE \tag{II.1}$$

$\Phi(E)$ represents the two components of the thermal and epithermal neutron flux.

For a flux of thermal neutrons, the reaction rate is given by:

$$R_0 = N_0 \Phi_{th}\sigma_{th} \tag{II.2}$$

σ_{th} is the thermal neutron capture cross section.

The reaction rate of the epithermal component is given by the following relationship

$$R_0 = N_0 \Phi_{epi} I_0 \tag{II.3}$$

I_0 is the resonance integral, and $N_0 = \frac{m\theta N_A}{M}$

The reaction rate in a sample irradiated in the reactor is given by the following relationship:

$$R_0 = R_{th} + R_{epi} = N_0 (\Phi_{epi} I_0 + \Phi_{th}\sigma_{th}) \tag{II.4}$$

The variation in the number of radioisotopes formed during the irradiation is given by the following expression:

$$\frac{dN(t)}{dt} = R - \lambda(t) \tag{II.5}$$

The given equation is a first order differential equation which can be easily solved by taking into account the initial conditions : $N(t = 0) = 0$

The number of nuclei produced at the end of irradiation is given by the following relationship:

$$N(t) = \frac{R}{\lambda}\left(1 - e^{-\lambda t_i}\right) \tag{II.6}$$

$S = (1 - e^{-\lambda t_i})$ is the saturation factor.

The saturation activity As is obtained when $ti \gg T_{1/2}$; it is given by the following relation:

$$A_s = \frac{m\theta N_A}{M} (\Phi_{epi} I_0 + \Phi_{th}\sigma_{th}) \tag{II.7}$$

The equation of the activity of a radioelement produced after a decay time t_d is given by the following relation:

$$A(t) = A_s S D \tag{II.8}$$

Where $D = e^{-\lambda t_d}$ is the decay factor.

After irradiation and appropriate radioactive decay, the γ energy spectrum is measured by counting the sample with a high resolution (to separate various γ-transitions of close-by energies) γ-detection system.

II.2.2. Qualitative analysis

Qualitative analysis consists of identifying the gamma-emitting elements contained in the analysed sample. The INAA technique provides highly resolved analysis of elemental composition by the identification of characteristic γ-ray energies associated with different isotopes. Often, there can be two or more radioelements which emit gammas of the same energy, producing interference in the gamma spectrum of the irradiated sample. This phenomenon generates confusion in the identification of the elements which requires a real correction of these interferences to correctly identify the elements composing the irradiated sample. In neutron activation analysis technique, two types of interference can be observed: 1st order interference and second order interference.

There are radioelements which can be produced by several ways of nuclear reactions, these reactions lead to the same final products and classified as first-order interference reactions. This type of interference can be corrected in spectrum analysis by taking into account the cross section of radioelements produced by fast neutrons.

Second-order interference poses a serious analytical problem if the irradiation time is relatively long under a high neutron flux ($\Phi > 10^{13} \, n \, cm^{-2} s^{-1}$). The radioelement produced by the neutron capture reaction can decay during irradiation giving a radioelement that can be produced by radiative capture reaction. This reaction can increase the activity after irradiation of the radioelement, which constitutes a significant source of error leading to an overestimation of the concentration of this element in the sample.

II.2.3. Quantitative analysis

During spectrometric measurements of the analysed samples, the intensity Np of the photoelectric peak measured using a gamma ray detector of efficiency ε is given by the following expression:

$$N_p = A_s S \varepsilon \gamma \int_{t_d}^{t_d+t_c} e^{-\lambda t_d} \, dt_d \qquad \qquad \text{(II.9)}$$

The integration of this expression taking into account the integration limits gives us the area of the characteristic peak of the element to be assayed according to the following relationship:

$$N_p = A_s \varepsilon \gamma \ SDC \tag{II.10}$$

$C = \frac{(1-e^{-\lambda t_c})}{\lambda}$, t_c is the count factor.

The amount of an element in a sample can be obtained from either the Absolute method or the relative method.

Absolute Method

The absolute method uses the basic neutron activation equation and, therefore, relies on the nuclear constants obtained from literature in addition to an accurate knowledge of the efficiency of the gamma detector and the neutron flux at the irradiation position.

the relationship between the net area of the gamma peak of a detected radioelement and the mass of the element is therefore written:

$$N_p = \frac{m\theta N_A \varepsilon \gamma}{M\lambda}(\Phi_{epi} I_0 + \Phi_{th}\sigma_{th})(1 - e^{-\lambda t_i})(e^{-\lambda t_d})(1 - e^{-\lambda t_c}) \tag{II.11}$$

The concentration of the element in the analysed sample is therefore given by the following relation:

$$m = \frac{M\lambda N_p}{\theta N_A \varepsilon \gamma (\Phi_{epi} I_0 + \Phi_{th}\sigma_{th})(1 - e^{-\lambda t_i})(e^{-\lambda t_d})(1 - e^{-\lambda t_c})} \tag{II.12}$$

The accuracy of measurement in this mode depends, therefore, on the accuracy of the nuclear constants, the accurate knowledge of the efficiency of the detector, the neutron flux, the counting statistics and source to detector geometry. For most elements, the errors in nuclear constants are less than 5%.

Relative Method

Most INAA experts normally use the relative method. In this approach, a standard containing a known amount of the element to be determined is irradiated along with the samples. It is assumed that the neutron flux, cross-sections, irradiation times and all other variables associated with counting are constant for the standard and the sample for a particular sample-to-detector geometry at the irradiation position. The equation for quantifying the amount of an element in a sample, using the relative method is [33]:

$$\frac{N_{sam}}{N_{st}} = \frac{m_{sam}(e^{-\lambda td})_{sam}}{m_{st}(e^{-\lambda td})_{st}}$$

(II.13)

m_{std} and m_{sam} are the masses of the element in the standard and sample.

II.3. X-ray fluorescence technique

X-ray Fluorescence is a well-established nondestructive analytical technique of X-ray emission spectroscopy. This technique is a powerful tool for rapid multielement nondestructive analyses and enable simultaneous detection of many elements in a solid or liquid with high-detection sensitivities, even in those cases where only small sample amounts are available. The fluoresced X-rays from the sample are collected and displayed with either energy dispersive or wavelength dispersive detector systems. The elements are identified by the wavelengths (qualitative) of the emitted X-rays while the concentrations of the elements present in the sample are determined by the intensity of those X-rays (quantitative).

Improvements in the sensitivity of spectrometers, coupled with development of computers, have expanded the field of XRF analysis. It has now widespread applications and plays an important role in many fields, such as industrial production of materials, prospecting resources, environmental monitoring, study of art and archaeology, and crime investigations.

II.3.1. Theoretical basics

When an analyte is irradiated by X-rays, an electron in the inner shell of an atom is removed and the hole created is filled by an electron in the outer shell. Excess energy is released in the form of X-rays whose energy is characteristic to each element. The intensity of the characteristic (fluorescent) X-rays is in proportion to the number of atoms of each element. Therefore XRF analysis is both a qualitative and a quantitative analytical technique, which has the capability of simultaneous, multi-elemental, non-destructive analysis in a wide concentration range from 100 % down to ppm level. The characteristic X-ray lines are superimposed on the continuous bremsstrahlung X-ray spectrum. The maximum energy of the electrons is defined by the accelerating voltage [33].

II.3.2. Bremsstrahlung radiation

Bremsstrahlung interactions, the primary source of x-ray photons from an x-ray tube, are produced by the sudden stopping, breaking or slowing of high-speed electrons at the target.

When the electrons from the filament strike the tungsten target, x-ray photons are created if they either hit a target nucleus directly (rare) or their path takes them close to the nucleus. If a high speed electron hits the nucleus of a target atom, all its kinetic energy is transformed into a single x-ray photon. (Total absorption has occurred). Thus, the energy of the resultant photon (keV) is numerically equal to the energy of the electron. This in turn is equal to the kilo-voltage applied across the x-ray tube at the instant of its passage. This happens rarely. Most high-speed electrons have near or wide misses with the nuclei. In these interactions, a negatively charged high-speed electron is attracted toward the positively charged nucleus and loses some of its velocity. This deceleration causes the electron to lose some kinetic energy [26]. The closer the high-speed electron approaches the nuclei, the greater is the electrostatic attraction on the electron, the braking effect, and the greater the energy of the resulting Bremsstrahlung photon. Bremsstrahlung interactions generate x-ray photons with a continuous spectrum of energy.

II.3.3. Characteristic radiation

Characteristic radiation occurs when an electron from the filament displaces an electron from an inner-shell of the tungsten target atom, thereby ionizing the atom. When this happens, another electron in an outer-shell of the tungsten atom is quickly attracted into the void in the deficient inner-shell [33,25,26]. When the displaced electron is replaced by the outer-shell electron, a photon is emitted with an energy equivalent to the difference in the two orbital binding energies.
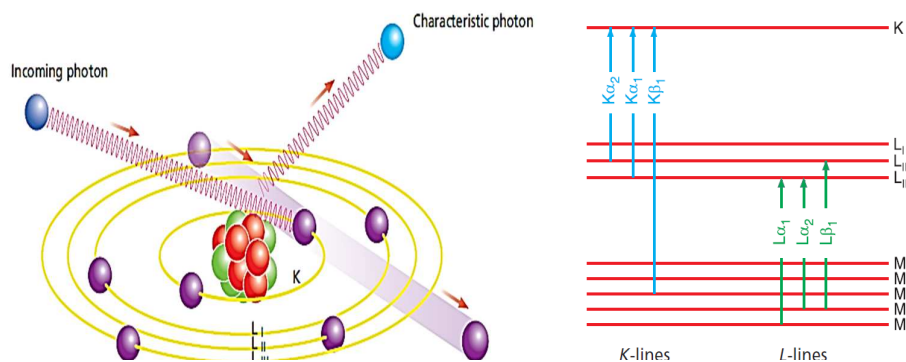
Figure II.3. Process of characteristic radiation production, b) shell lines and permissible transition

Characteristic radiation from the K-shell occurs as discrete increments compared with Bremsstrahlung radiation. The energies of characteristic photons are a function of the energy levels of various electron orbital levels and hence are characteristic of the target atoms.

Characteristic radiation has a higher intensity, is preferred but is only a minor source of radiation from an x-ray tube.

II.3.4. XRF spectrometer

XRF spectrometers fall into two main categories depending on whether they employ a wavelength dispersive approach or an energy dispersive approach. In the wavelength dispersive approach, the fluorescent X-rays from a sample are directed onto the surface of an analyzing crystal. X-rays are diffracted at various angles that depend on the wavelength, according to Bragg's expression. X-ray spectrum is obtained by moving a detector along the diffraction angle. In the energy dispersive approach, the fluorescent X-rays from a sample are directly let into a detector that generates an electronic signal proportional to the energy of X-rays. X-ray spectrum is obtained by measuring the intensity at each energy value with a multi-channel analyzer. The wavelength dispersive instrument has large dimensions and needs long measurement time due to the need for moving the detector, although it has better resolving power than the energy dispersive instrument. On the other hand, the energy dispersive instrument has small dimensions and needs short measurement time. This latter will be used in the present work.
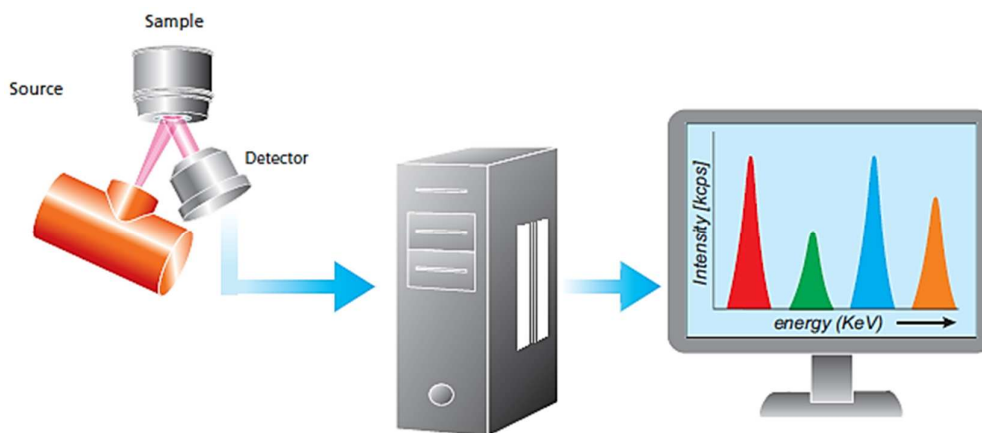
Figure II.4*.Basic designe of ED-XRF spectrometer*

EDXRF spectrometers use a semiconductor material (an x-ray detector) to convert characteristic x-rays into electrical signals. The spectrometer's electronics digitize the signals produced by the detector, and send this information to a PC or internal electronics for display and analysis

<u>X-Ray tube</u>

The most important component of the apparatus is the x-ray tube in order to produce an x-ray source. The basic design of an X-ray tube is shown in Figure II.5.
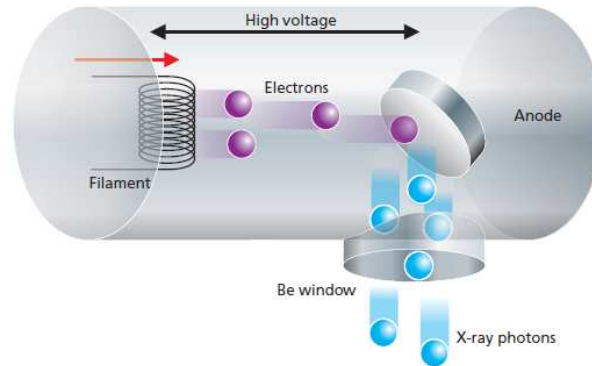
Figure II.5. *designe of X-Ray tube*

It contains a filament (wire) and an anode (target) placed in a vacuum housing. An electrical current heats up the filament and electrons are emitted. A high voltage (20..100 kV) is applied across the filament and the anode, and this high voltage accelerates the electrons towards the anode. When the electrons hit the anode they are decelerated, which causes the emission of X-rays.

<u>X-Ray detector</u>

The function of the x-ray detector is to convert the energies of the x-ray photons into voltage pulses which can then be counted, giving in turn a measurement of the total x-ray flux. Detector used in modern x-ray spectrometers are almost invariably "proportional" detectors, and these have the property that the energy of the incident x-ray photon determines the size of the voltage pluses produced by the detector. Where this is the case, it is possible to employ a means of selecting only a narrow range of voltage pulses, and this may be useful in discriminating against unwanted radiation.

<u>II.3.5. Factors controlling the x-ray beam</u>

The x-ray beam emitted from an x-ray tube may be modified to suit the needs of the application by altering the beam exposure length (timer), exposure rate (mA), beam energy and filtration, beam shape (collimation), and target-patient distance (long or short cone)

Exposure Time

Portrays the changes in the x-ray spectrum that result when the exposure time is increased while the tube current (mA) and voltage (kV) remain constant. When the exposure time is doubled, the number of photons generated is doubled, but the range intensity of photons energies is unchanged. Therefore, changing the time simply controls the "quantity" of the exposure, the number of photons generated.

Tube Current (mA)

Illustrates the changes in the spectrum of photons that result from increasing tube current (mA) while maintaining constant tube voltage (kV) and exposure time. As the mA setting is increased, more power is applied to the filament, which heats up and releases more electrons that collide with the target to produce ration. A linear relationship exists between mA and radiation output. The quantity of radiation produced is expressed as the product of time and tube current. The quantity of radiation remains constant regardless of variations in mA and time as long as their product remains constant.

Tube Voltage

Increasing the Tube Voltage increases the potential difference between the cathode and anode, thus increasing the energy of each electron when it strikes the target. The greater the potential difference the faster the electrons travel from the cathode to the anode. This results in an increased efficiency of conversion of electron energy into x-ray photons, and thus an increase in the number of photons generated, their maximal energy.

The increased number of high-energy photons produced per unit time by use of higher kV results from the greater efficiency in the production of Bremsstrahlung photons that occurs when increased number of higher-energy electrons interact with the target. The ability of x-ray photons to penetrate matter depends on their energy. High-energy x-ray photons have a greater probability of penetrating matter, whereas relatively low energy photons have a greater probability of being absorbed.

II.3.6. Qualitative analysis

Measurement of fluorescence radiation energy makes it possible to identify the different elements constituting the irradiated sample. These energies are given by Moseley's law:

$$E_{min} = Rh\,(z - \sigma)^2\,[\frac{1}{n^2} - \frac{1}{m^2}] \tag{II.14}$$

Where

Rh: Rydberg's constant
Z: atomic number
σ: Screen constant of the atom.

II.3.7. Quantitative analysis

The intensity of the characteristic line of any element present in the sample is proportional to its concentration. If there is no interaction of the radiation with the matrix (medium surrounding element), the intensity measured will be directly proportional to the concentration according to the following relationship:

$$I = K \times C \tag{II.15}$$

K: the sensitivity of the ED-XRF device
C: the concentration of an element
I: the intensity of an element

This intensity is likely to be modified by matrix effects (absorption of primary and secondary X-rays). Among the correction methods used, we can cite the external standard method, and internal standard.

External standards method

Based on the use of standard compounds containing identified elements, at known concentrations. The irradiation of the standards and the samples to be analysed under the same conditions, allows the calculation of the unknown concentrations of the elements constituting the sample. The expression of the concentration of the element to be assayed in the sample becomes:

$$C_x = C_{st} \times \frac{I_x}{I_{st}} \tag{II.15}$$

Where :

C_x : Concentration of the element in the sample.
C_{st} : Concentration of the element in the standard.
I_x : Intensity of the element in the sample.
I_{st} : Intensity of the element in the standard.

Internal standard method

This method consists of adding an element to the sample in a known proportion in such a way that it does not interfere with the elements of interest. The concentrations of the elements present are calculated from the areas of the X-rays taking into account the sensitivity and absorption factors. In general, the concentration of any element is given by the expression below:

$$\frac{Ix}{Ist} = \frac{\sigma_x \times \varepsilon_x \times C_x}{\sigma_{st} \times \varepsilon_{st} \times C_{st}} \tag{II.16}$$

σ_{st}: X-ray production cross section of the standard element;

σ_x: X-ray production cross section of the element sought;

ε_{st}: Detector efficiency for the characteristic X-ray energy of the standard element;

ε_x: Detector efficiency for the characteristic X-ray energy of the search element.

Chapter III

Experiments and Monte Carlo simulation

This chapter provides a general description of Monte Carlo simulation methods. Emphasis will be placed on the codes implemented in this work, namely the MCNP 5 (Monte Carlo N Particles) code developed by the Los Alomos National Laboratory. The chapter describes the radiometric measurements, experimental set-up and the methodology used in this study. As well as the Monte Carlo simulations approaches devoted to the study and evaluation of the germanium dead layer thickness after two decades of operation. Self-absorption and coincidence summing factors will be discussed. The experimental measurements will be confronted with the modelling calculations of the detection geometries by Monte Carlo. All the results are compared to the measurements by Instrumental neutron activation analysis as a technique of accuracy validation

III.1. Laboratory standard preparation

Sample preparation may seem, from first impression, the most routine aspect of an analytical protocol. However, it is critical that analysts realize and remember that a measurement is only as good as the sample preparation that has preceded it. If an aliquant taken for analysis does not represent the original sample precisely, the results of this analysis are doubtful.

In this work, a Certified mixed radioactive source from the Czech Metrology Institute provided by International Atomic Energy Agency (IAEA) was used for the standard preparation.

The mixed source is in the form of radioactive solution in a 100 ml bottle. The carrier solution consists of 20 mg of Cd, Ce, Co, Cs, Sr,Y chlorids/l , and 20 mgH_2SnCl_6/l , also 20 mg of Sm $(NO_3)_3$/l, 30 mgCl$_3$/ l + 144gCl/ l in distilled water. The density of the solution is 1.065 g/cm^3 .

Table III.1: characteristic of the mixed source

Radionuclide	Half life	Activity (kBq)
Am-241	432.6 (year)	13.72
Cd-109	461.9 (days)	53.08
Ce-139	137.64 (days)	6.317
Co-57	271.8 (days)	4.348
Co-60	5.27 (years)	8.38
Sn-113	115.09 (days)	8.49
Cs-137	30.05 (years)	6.907
Sr-85	64.85 (days)	12.93
Y-88	109.6 (days)	21.62
Cr-51	27.704 (days)	63.3

An amount of 19 mL of radioactive solution were mixed to 171.3 g of a phosphate matrix in a cylindrical plastic container; the standard preparation is described in Figure III.1.

Standard preparation

^{241}Am	7%	
^{51}Cr	32%	
^{88}Y	11%	
^{85}Sr	7%	
^{113}Sn	4%	
^{137}Cs	3%	
^{60}Co	4%	
^{57}Co	2%	
^{139}Ce	3%	
^{109}Cd	27%	
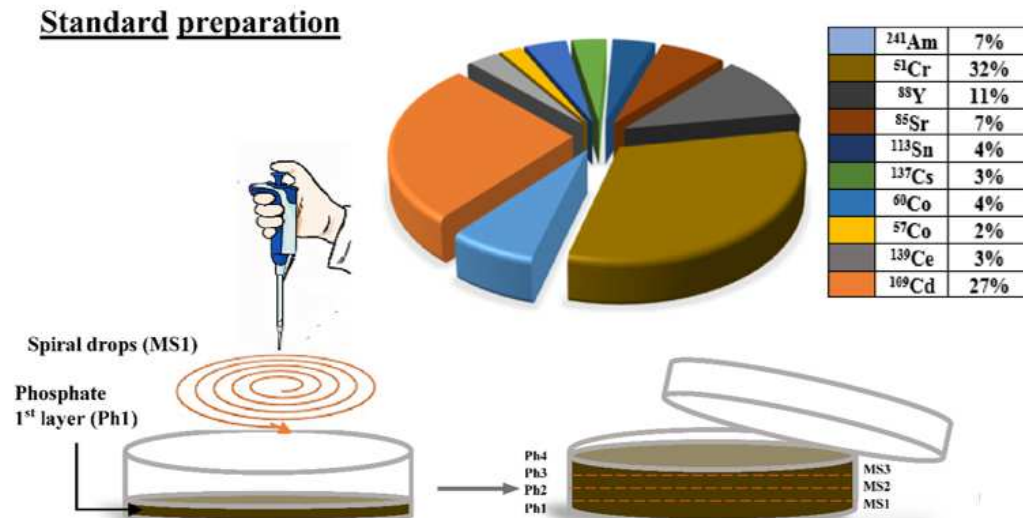
Figure. III.1 *Preparation of the calibration standards.*

An equal portion of the liquid source was homogeneously dropped in spiral motion on phosphate layers to ensure a uniform spatial distribution of the radioactive source in the matrix. The Source was packaged in cylindrical geometry sample holders (petri bottle).

III.3. Gamma spectrometry system

The experiments were carried out in the Algiers Nuclear Research Centre (CRNA), Nuclear Applications' Division. Low level specific activity measurement was performed using a gamma ray spectrometry system consisting of a Co-axial P-type high purity germanium (HPGe) detector (GX-3519 manufactured by Canberra™). The detector has a 35% relative efficiency and a resolution of 1.8 keV for the ^{60}Co gamma ray at 1332 keV [26].

The detector is connected to a DSA-LX Canberra (Digital Signal Analyzer) that ensures all conventional associated electronics tasks. All the equipment is monitored by a Genie2000 software.

Figure III.2. *Gamma Spectrometer*

The detector is kept in a 100 mm thick lead shielding cavity with inner layers of tin and copper respectively1 mm and 1.6 mm thick, meant to reduce the contribution from Pb X-rays [27,28]. The detector was calibrated in absolute efficiency.

III.3.1. Energy calibration

The first step of the work before all the measurements is the energy calibration of the gamma spectrometry chain. This energy calibration consists of determining the energy line as a function of the channel number; this operation is carried out using a point radioactive source whose gamma energies are well known. In this case, it is preferable to use standard sources which can cover a very wide energy spectrum from 30 keV to 1500 keV. In the present work, the energy calibration was carried out with a source of [152]Eu. The gamma spectrum was collected during a time of 3600 seconds. The calibration line giving the energy as a function of the channel number was determined by adjusting the experimental points using the least squares method. In table below, we give the main gamma energies of the [152]Eu source used for the energy calibration.

Table III.2. gamma energies of the [152]Eu source used for the energy calibration

E (keV)	Channel
121,78	330
344,31	930
778,87	2103
964,01	2603
1112,04	3003
1408,02	3803

The curve in figure III.3 illustrates the evolution of the energy of gamma photons as a function of the position of the corresponding channel.
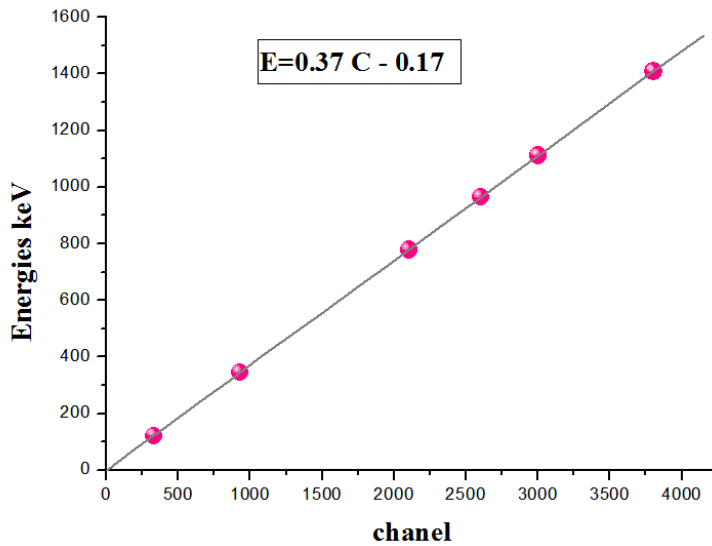
Figure III.3. *Energy of gamma photons as a function of channel position.*

III.3.2. Efficiency calibration

The absolute efficiency of the detector is defined by the ratio of the number of photons detected to the number of photons emitted by the source, this definition is translated by the following relationship:

$$\varepsilon = \frac{N/t_c}{A*\gamma} \tag{III.1}$$

Where ε is the detector efficiency; N the intensity of the total absorption peak; A is the source activity at measurement time; γ: Branching ratio; t_c: Collection time.

The activity at collection time is corrected by the decay time of the source from the date of manufacture. The error on the measured efficiency is calculated from the error propagation law. The uncertainty on the measurement of the efficiency of the detector is given by the following relationship:

$$\frac{\Delta\varepsilon}{\varepsilon} = \left[\left(\frac{\Delta N}{N}\right)^2 + \left(\frac{\Delta A}{A}\right)^2 + \left(\frac{\Delta\gamma}{\gamma}\right)^2 + \left(\frac{\Delta t_c}{t_c}\right)^2\right]^{1/2} \tag{III.2}$$

To establish the relationship between efficiency and energy, it is necessary to acquire a calibrated energy spectrum of known standard radioactive sources, for a long enough time

to obtain peaks with a small uncertainty. The HPGe detector used in this work was calibrated using the standard source prepared previously in order to obtain the experimental calibration curve and to compare it thereafter with the results calculated by the MCNP code. The fixed counting time for the cylindrical source is 5000 seconds. In Figure IV.4, we present the experimental spectrum of the mixed source in phosphate measured during a time of 5000 seconds
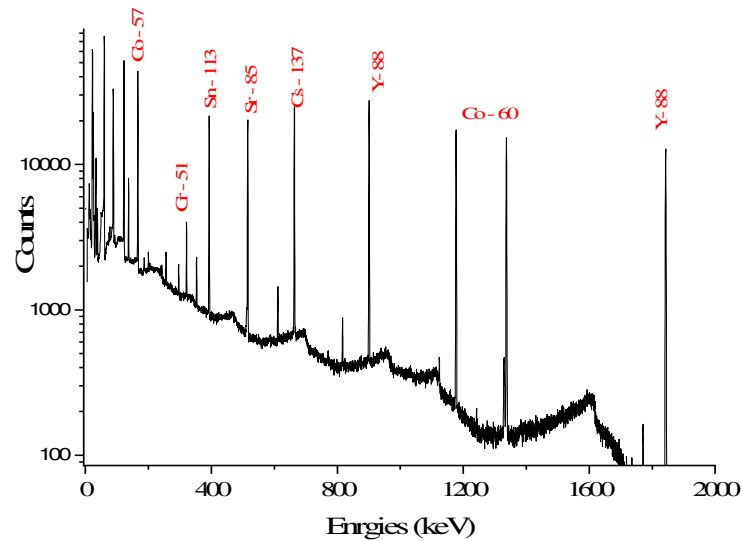
Figure III.4. Experimental spectrum of the mixed source in phosphate matrix.

The efficiencies measured by the mixed sources in phosphate matrix are plotted in the efficiency curve Figure III.5
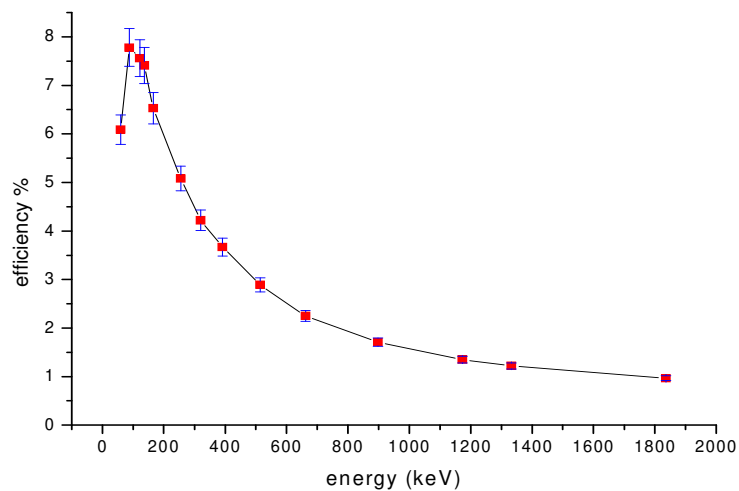
Figure III.5. Experimental efficiency curve

and reported in table III.3

Table III.3. Experimental efficiency of the detector in cylinder geometry

Element	Energies (keV)	$T_{1/2}$ (days)	$A_s(t)$ (Bq)	ε_{exp} (%)
^{241}Am	59.84	158007.15	2349,9	5.87 ± 0.32
^{109}Cd	88	461.9	7763,8	7.43 ± 0.40
^{57}Co	122.06	271.81	569,3	7.56 ± 0.37
^{57}Co	136.45	271.81	569,3	7.41 ± 0.38
^{139}Ce	165.85	137.641	636,3	6.55 ± 0.31
^{113}Sn	255.17	115.09	770,6	4.77 ± 0.39
^{51}Cr	320.08	27.704	774,02	3.96 ± 0.17
^{113}Sn	391.69	115.09	770,59	3.45 ± 0.17
^{85}Sr	514	64.85	717,29	2.78 ± 0.12
^{137}Cs	661.65	10975.76	1175,73	2.13 ± 0.11
^{88}Y	898.04	106.63	1865,84	1.6 ± 0.08
^{60}Co	1173,23	1925,327	1383,14	1.26 ± 0.07
^{60}Co	1332,5	1925,327	1383,14	1.14 ± 0.06
^{88}Y	1836,06	106,63	1865,84	0.91 ± 0.05

III.4. Monte Carlo simulation

III.4.1. Introduction

The Monte Carlo simulation method owes its name to Metropolis and Ulam in the 1940s, these authors are the first to have described this method for military applications concerning the first atomic bombs. These techniques are now being introduced in many fields of application, which may have little in common. They involve the generation of pseudo-random numbers that are shaped according to certain probability density functions that are associated with a model. The latter is often a real physical system, but can for example be a mathematical system, or any imaginary world governed by laws that can be expressed in discrete terms that can be used on a calculating machine. It is necessary to differentiate these methods of statistical simulation from the conventional methods of numerical discretization which are in most cases applied to the partial differential equations describing the system.

The idea of using random simulations is directly linked to the complexity of interactions in a given medium. The use of conventional analytical expressions to describe these interactions is limited, and often requires approximations. When applying the principle of

simulation to particle transport, it is possible to extract data on all the parameters used in the simulation. This type of data is often difficult or impossible to derive from deterministic calculation methods or experimental measurements.

III.4.2. MCNP Code

The Monte Carlo N-Particle (MCNP) computer code is a particle transport code with powerful three dimensional geometry and source modeling capabilities that can be applied to reactor physics, shielding, criticality, environmental nuclear waste cleanup, medical imaging, and numerous other related areas.

The advantages provided by Monte Carlo codes are the taking into account of the elementary physical phenomena involved during each interaction and the possibility of a very precise description of the geometry and the chemical or elementary composition of the target materials in their real environment. These advantages allow the precise and targeted determination of the physical quantities sought, in particular the components inaccessible to the experiment.

Monte Carlo N-Particles tracks neutral particles (photons, neutrons), electrons and positrons. Some heavy charged particles were later introduced in its MCNPX version. It is directly linked to the origin of the Manhattan Project. This code is one of the most widely used particle transport calculation codes for modeling calculations. Its fields of application are varied, whether nuclear detection, dosimetry, nuclear physics, reactor calculations or any other nuclear installation. Simulation calculations are based on the transport of neutrons, photons and electrons alone or combined in complex three-dimensional configurations composed of various materials.

III.4.3. MCNP5 input file format

Creating a MCNP input file with a line editor is both tedious and error prone as it entails arduous descriptions of geometry, tallies, sources, and optimization parameters. These input files may contain thousands of lines, and once the input file is created, substantial additional time is often required to plot and test the geometry and to correct any errors. The MCNP input file describes the problem geometry, specifies the materials and source, and defines the results you desire from the calculation. The geometry is constructed by defining cells that are bounded by one or more surfaces. Cells can be filled with a material or be void. An

MCNP input file has three major sections: cell cards, surface cards, and data cards. A one-line title card precedes the cell card section.

An input file has the following form:

> *Message Block*
> *Blank line delimiter*
> *One- line problem title card*
> *Cell cards*
> •
> •
> *Blank line delimiter*
> *Surface cards*
> •
> •
> *Blank line delimiter*
> *Data cards*
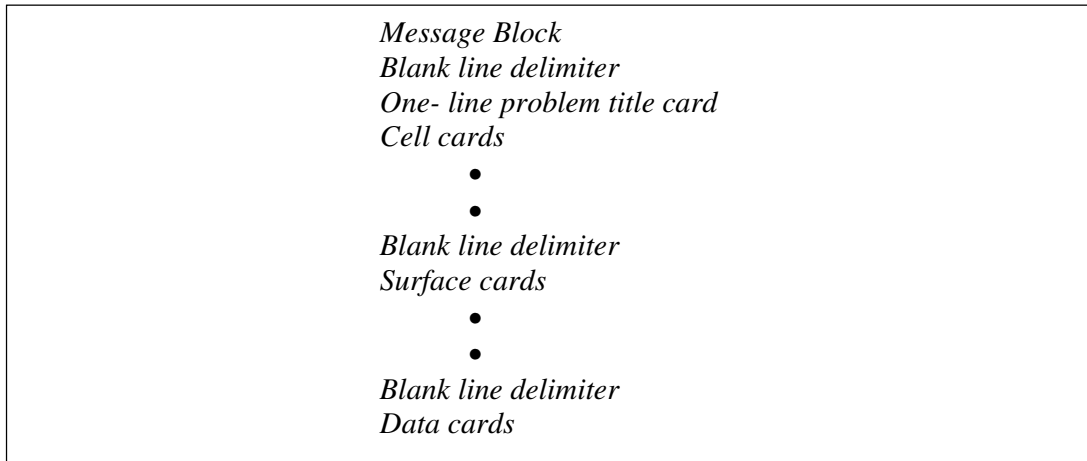
Cell Cards

The first section after the title card is for the cell cards and has no blank line delimiter at the front of it. Cells are used to define the shape and material content of physical space. The specific format for a cell card is:

> *J   m   d   geom   params*
>
> *j*   *cell number*
> *m*   *material number (0 if cell is a void)*
> *d*   *material density*
> *geom*   *list of all signed surface numbers that specify a cell*
> *params*   *optional specification*
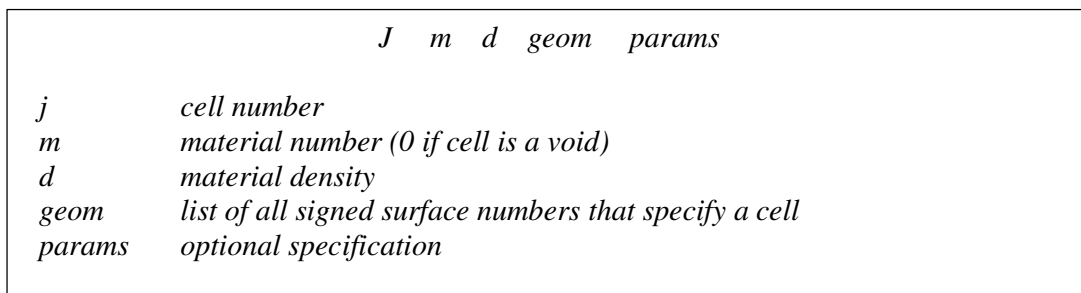
Surface Cards

Surfaces are the geometric shapes used to form the boundaries of the problem being modelled

> *j   a   list*
> *j*   *Surface number*
> *a*   *Surface type (plane, sphere, cylinder, …)*
> *list*   *Surface description: radius, dimensions (in cm) …*
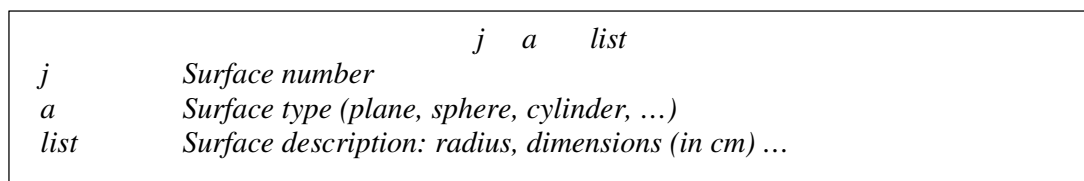
Source Specification Cards

A source definition card SDEF is one of four available methods of defining starting particles

The SDEF card defines the basic source parameters, some of which are

POS	*x y z default is 0 0 0*
CEL	*starting cell number*
ERG	*starting energy default is 14 MeV*
PAR	*source particle type 1 for N, N P, N P E; 2 for P, P E; 3 for E*

Tally Specification Cards

The tally cards are used to specify what you want to learn from the Monte Carlo calculation. The tallies are identified by tally type and particle type. all the tally cards and fully describtion are given bellow.

F1:N or F1:P or F1:E	*Surface current*
F2:N or F2:P or F2:E	*Surface flux*
F4:N or F4:P or F4:E	*Track length estimate of cell flux*
F5a:N or F5a:P	*Flux at a point (point detector)*
F6:N or F6:P or F6:N,P	*Track length estimate of energy deposition*
F7:N	*Track length estimate of fission energy deposition*
F8:P or F8:E or F8:P,E	*Energy distribution of pulses created in a detector*

Materials Specification

The following card is used to specify the isotopic composition for all cells containing material m.

	Mm ZAID fraction
m	*corresponds to the material number on the cell card.*
ZAID	*used to identify the element or nuclide desired. The form of the number is ZZZAAA , where ZZZ is the atomic number of the element or nuclide, AAA is the mass number of the nuclide, ignored for photons and electrons*
Fraction	*the elemental composition, and may be normalized to 1*

III.5. HPGe detector simulation procedure

Some of the data required for the detector's simulation are found in its certificate provided by the manufacturer, which describes its characteristics and dimension. Table III.4
The simulation parameters will be described in details in order to properly present the procedure used.

Table III.4. Detector's characteristics and dimension.

Detector parameters	Dimension (mm)
Germanium diameter	60.5
Germanium length	61
Dead layer thickness	0.004
Hole diameter	12
Hole length	51
Aluminium casing thickness	1.5
Carbon epoxy thickness	0.5
Germanium to aluminium end-cap	5

The detector characteristics which are provided by the manufacturer include: the material, geometry and dimensions of the detector and its components. Usually, such details are not precisely provided by the manufacturer. Hence, the generated simulation model might not represent the typical detector although it gives accurate results for specific adapted cases. In addition, some provided data may change with time such as the thickness of the dead layer which requires re-characterization of the detector
The simulation was performed using the MCNP5 code in PE mode (photon and electron mode), this mode is recommended for the transport of low energy photons, the cut-off energy for the photons is fixed at 1 keV to promote all types of interactions of photons with the germanium crystal (photoelectric interaction, Compton scattering and the pair creation effect for high energy photons), the number of simulated particles is fixed at 10^8 particles to obtain a simulation error of less than 1%.

When using MCNP5, a Gaussian broadening given by the Gaussian Energy Broadening (GEB) equation is applied to account for the experimental resolution of the Ge (HP) detector for each photon energy.

The experimental data of Full Width at Half Maximum (FWHM) was fitted by the following function [1]

$$FWHM\,(MeV) = a + b\sqrt{E + cE^2}$$

(III.3)

Where: a= 0.707 10^{-3} MeV, b= 0.946 10^{-3} MeV$^{1/2}$, c=0 provided by genie2000 software.

III.5.1. Simulation without detector adjustment

The first model was based only on the CANBERRA information shown in table 1. In the simulation, the crystal in the detector and its surrounding materials, including the absorbing materials, were taken into consideration. The crystal had rounded edges, but no description was obtainable from the schematic illustration provided by the manufacturer.

The mathematical description is composed of torus, spheres, planes, and cylinders blended together. The complete MCNP5 input code can be find in Appendix 01. The schematic figure of the detector's structure reproduced in MCNP5 simulation is shown in Figure III.6
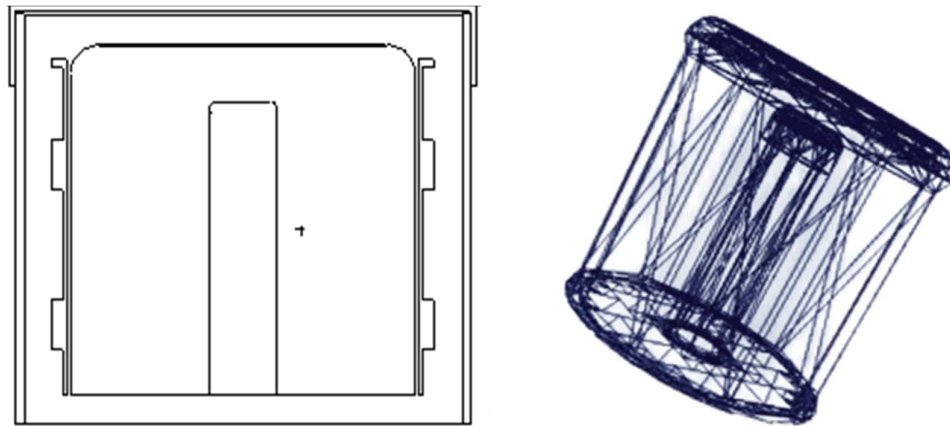
Figure III.6:schematic figure of the detector's structure reproduced in MCNP5 simulation

ln order to determine the influence of the detector parameter on the efficiency, MCNP5 efficiency calculated was compared to the experimental efficiency, for photon energy ranging from 50 keV to 2000 keV.

 MCNP results before adjustment are given in table III.5.

Table III.5: MCNP efficiency results before adjustment compared to experimental results

Element	Energies (keV)	$T_{1/2}$ (days)	$A_s(t)$ (Bq)	ε_{exp} (%)	ε_{MCNP} (%)
^{241}Am	59.84	158007.15	2349,9	5.87 ± 0.32	6,81 ± 0,13
^{109}Cd	88	461.9	7763,8	7.43 ± 0.40	9,36 ± 0,18
^{57}Co	122.06	271.81	569,3	7.56 ± 0.37	9,37 ± 0,19
^{57}Co	136.45	271.81	569,3	7.41 ± 0.38	9,36 ± 0,18
^{139}Ce	165.85	137.641	636,3	6.55 ± 0.31	8,37 ± 0,16
^{113}Sn	255.17	115.09	770,6	4.77 ± 0.39	6,3 ± 0,12
^{51}Cr	320.08	27.704	774,02	3.96 ± 0.17	5,19 ± 0,10
^{113}Sn	391.69	115.09	770,59	3.45 ± 0.17	4,42 ± 0,08
^{85}Sr	514	64.85	717,29	2.78 ± 0.12	3,5 ± 0,07
^{137}Cs	661.65	10975.76	1175,73	2.13 ± 0.11	2,92 ± 0,05
^{88}Y	898.04	106.63	1865,84	1.6 ± 0.08	2,29 ± 0,04
^{60}Co	1173,23	1925,327	1383,14	1.26 ± 0.07	1,91 ± 0,03
^{60}Co	1332,5	1925,327	1383,14	1.14 ± 0.06	1,74 ± 0,03
^{88}Y	1836,06	106,63	1865,84	0.91 ± 0.05	1,35 ± 0,02

As Figure IV.7, shows, in reference to the experimental efficiencies, significant differences between experimental results and MCNP5 calculations were observed.

Such discrepancy is usually attributed to:

- The errors associated with the values supplied by manufacturer,
- Incomplete charge collection in the crystal,
- An underestimation of the thickness of the dead layer caused by the p-contact and often the degradation of the detector over time
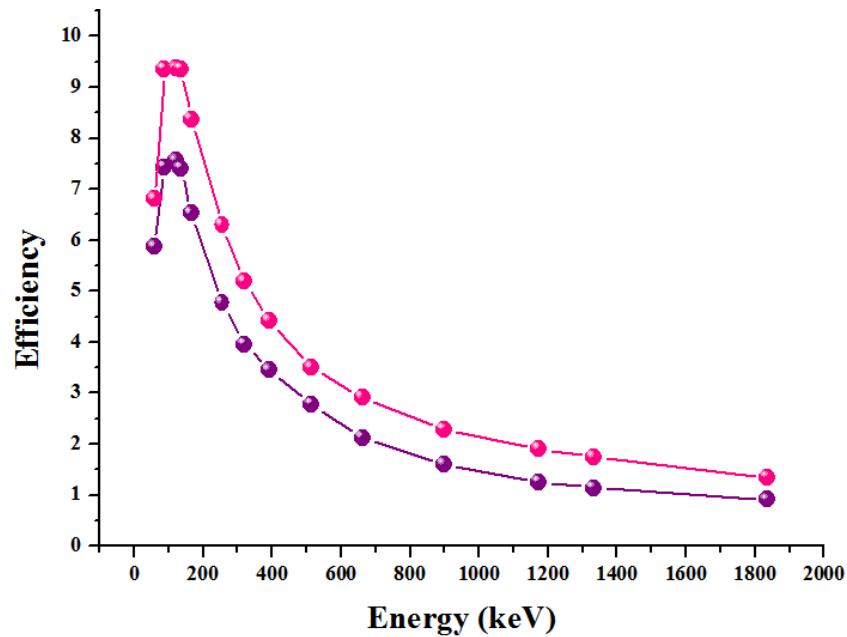
Figure III.7*: MCNP5 efficiency curve (in pink) in reference to the Experimental efficiency curve (in purple) based on the manufacturer dimensions*

creating a mathematical model for a radiation detector with an acceptable accuracy is a main objective for many of gamma ray spectrometer's users.

The approach for accomplishing such target is important, since many factors should be included while reaching the improved model.

Optimization of detector model to give accurate values for the efficiency at specific gamma ray energy may interrupt the detector response at other energies. This effect could be explained while dealing with the dead layer thickness of the detector since the attenuation effects are higher for smaller gamma rays energies.

Therefore, the approach for building the optimized model is to investigate the main and most effective parameters and construct the model with minimal variations for the data provided by the constructer.

To reduce the disagreements between the calculated and measured efficiencies seen in Fig III.7, the dead-layer thickness in the second model should be scaled up.

III.5.2. Dead layer thickness adjustment

In order to evaluate how a dead-layer variation affects the efficiency determination a set of certified point sources was used to optimize the mathematical model of the HPGe detector. The specifications and characteristics of the point sources are given in Table IV.6.

Table III. 6 : specifications and characteristics of the point sources.

R-element	Energie kev	γ (abondance)	ε_{ab} experimental		
Am 241	59,54	0,359	5,20E-04	±	2,60E-05
Cs 137	661,6	0,851	8,25E-04	±	4,12E-05
Co 60	1332,4	0,9998	5,63E-04	±	2,81E-05
	1173,2	0,9985	6,13E-04	±	3,07E-05
Ba-133	356	0,6205	1,20E-03	±	5,99E-05
	80	0,329	1,60E-03	±	8,01E-05
	302,85	0,1834	1,35E-03	±	6,73E-05
	383,8485	0,0894	1,13E-03	±	5,64E-05
	276,3989	0,0716	1,35E-03	±	6,76E-05
Eu-152	121,7817	0,2853	7,77E-04	±	3,89E-05
	1408,013	0,2087	5,78E-04	±	2,89E-05
	964,057	0,1451	6,92E-04	±	3,46E-05
	1112,076	0,1367	6,39E-04	±	3,20E-05
	1085,837	0,1011	6,53E-04	±	3,26E-05

For the measurement configuration of the point-like source, a distance of 135 mm was selected to exclude the coincidence summing effects. The coincidence summing effects can be considered as insignificant at this distance. Therefore, the optimization of the detector model is not affected by the coincidence summing effects.

When we considered a dead layer with a homogeneous thickness (uniform thickness of germanium material), it was very difficult to achieve agreement between simulated and measured detection efficiencies at both low and high photon energies at the same time. Therefore, we relied on using the approach of inhomogeneous dead layers (non-uniform thickness). However, the most significant dead layer thickness in the case of P-type HPGe detector is located on the outer surface of the Ge-crystal, owing to the overlapping of the weakness of the electrical field and lithium-diffused layer in the same region.

III.6. Optimisation Procedure and Calculations

In the present study, a procedure was proposed for optimizing the model of p-type HPGe detector. three parameters of this detector model including the thickness of the lateral dead-layer, the thickness of the top dead-layer, and the Hole length were adjusted step-by-step to achieve the optimized detector model. It is worth noting that the lateral dead-layer and the top dead-layer were adjusted separately and different thicknesses of these layers were expected.

The steps for this procedure were summarized in:

Adjusting thikness of the lateral dead layer using high energies 1300-1500 keV

Adjusting Hole lenght for medium to high enegies 200-1000 keV

Adjusting thikness of the Frontal dead layer using low energies 59 keV
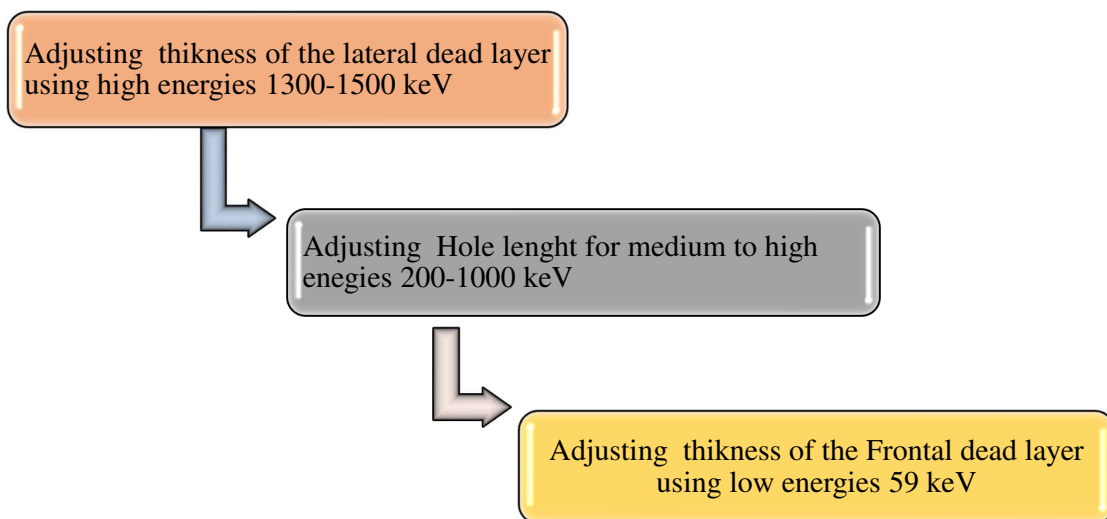
Figure III.8. *Optimisation Procedure of HPGe co-axial P-type detector*

For the adjustment of each parameter, Monte Carlo simulations were performed with the variations in the value of interested parameter to calculate the FEP efficiencies. It should be noted that the order of the steps for adjusting the parameters is essential.

III.6.1. Adjusting the thickness of lateral dead‑layer

The first adjustment was made for the thickness of the lateral dead-layer. For this adjustment, high energies of 1332,5 keV from Co-60 and 1408.06 keV from Eu-152 were considered for the measurement configuration of the point-like source at a distance of 135 mm.
 These energies were selected because the influence of the top dead-layer and the distance from crystal to front end-cap on their values is insignificant.
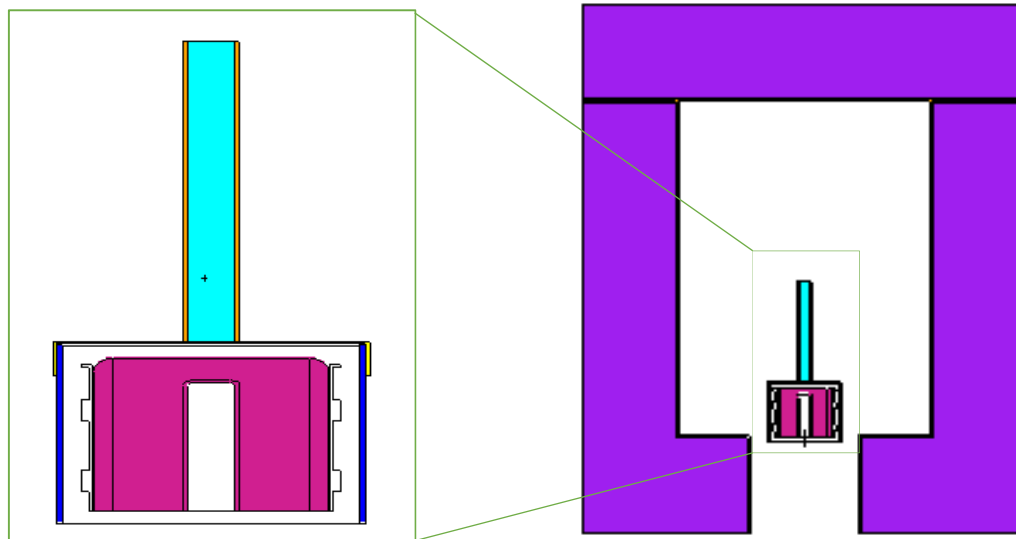
Figure III.9*: Measurement configuration of HPGe detector and the schielding*

The results calculated for the simulated efficiency with the photon energy of 1332.5 -1408,06 keV were shown in the following table:

Table III.7 : Efficiency (E-04) dependency with lateral dead layer variation

Source	E (keV)	ε_{exp}	ε_{MCNP}					
			0 µm	500µm	900µm	1mm	2 mm	3 mm
Co 60	1332.5	5,63E-04	2,00E-03	1,85E-03	1,67E-03	9,30E-04	8,10E-04	6,10E-04
Eu-152	1408.06	5,78E-04	1,80E-03	1,72E-03	1,58E-03	8,52E-04	6,88E-04	5,94E-04

The changes were started from of 500µm to 3 mm with a step of 1 mm. at 3 mm change in the thickness of the lateral dead-layer from the manufacturer's specification, our simulated results showed that the relative deviations in efficiency are 8% at 1332.5 keV, and 2% at 1408.06 keV, Basically, with the photon energy high enough, the attenuation of photon intensity within the absorber layers between the source and the active volume of the detector can be ignored. Therefore, it can be deduced that the effect of the top dead-layer on the FEP efficiencies at high energies is negligible.

III.6.2. Adjusting the Detector Hole depth

The hole depth of the detector is not only a geometry factor but it affects the efficiency of the detector as well, since the active volume of the detector is changed with it. Moreover, as the hole depth is changed, the response of the detector changes differently with different gamma ray energies.

The reason for this could be understood based on the fact that gamma rays with relatively higher energies are absorbed at deeper locations in the detector body than those with relatively lower energies. At such locations the effect of detector hole is not the same. For the hole depth adjustment, medium energies were considered: 661.65 keV of Cs-137, 276.36 -384.84 keV of Ba-133, 1173.22 of Co-60 and 964.06 of Eu-152. From the calculations it was found that the simulated efficiencies vary differently with the hole depth.

As shown in table IV.8, as the hole depth increased about 2 mm, the simulated results showed a relative efficiency deviation of less than 8%.

Table III.8 : Efficiency dependency with DL of the hole

Source	E (keV)	ε_{exp}	0 µm	1 mm	2 mm
Cs 137	661,65	8,25E-04	1.93E-03	1,20E-03	8,73E-04
Ba-133	356,01	1,20E-03	2.08 E-03	1,46E-03	1,17E-03
	302,85	1,35E-03	2.2 E-03	1,92E-03	1,30E-03
	383,84	1,13E-03	1.98 E-03	1,64E-03	1,13E-03
	276,39	1,35E-03	2.43E-03	1,67E-03	1,29E-03
Co-60	1173,22	6,13E-04	1.23 E-03	9,80E-04	6,80E-04
Eu-152	964,06	6,92E-04	1.79 E-03	1,60E-03	7,30E-04
	1112,07	6,39E-04	1.29 E-03	1,08E-03	7,10E-04
	1085,83	6,53E-04	1.43 E-03	1,10E-03	7,00E-04
	121,78	7,77E-04	1.62 E-03	1,20E-03	8,50E-04

III.6.3. Adjusting the thickness of top dead‑layer

It is important to note that the most difficult area in the dead layer adjustment is situated in the top of the crystal surface, where the counting efficiency is very sensitive to any dead layer thickness variation. A small variation in the dead layer thickness of this region leads to a big variation to the efficiency value. Therefore, if the outer top dead layer is well adjusted, then it is less-difficult to adjust the others.

Table III.9 : Efficiency dependency with entrance dead layer variation

ε_{sim} MCNP 5 (10^{-4})								
Source	E (keV)	ε_{exp}	0 µm	50µm	100µm	150µm	200µm	250 µm
Am- 241	59,54	5,20	5.6	5.47	5.35	5,21	5,08	5.00

After several adjustments table above, by increasing the dead layer thickness until reaching a shift of 0.1%, The value of the frontal dead layer thickness was finally optimized to 150 µm.
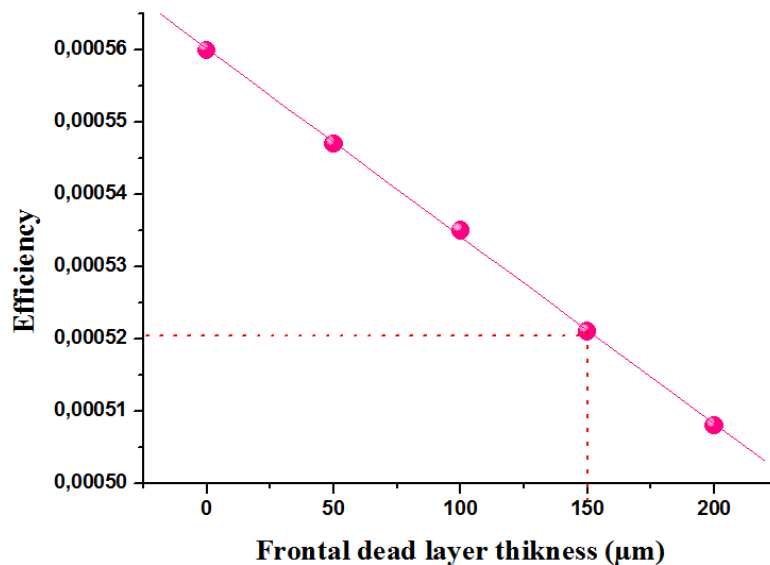
Figure III.10: *The linear dependence of the simulated efficiency on the thickness of the top dead layer for 59 KeV*

III.7. Simulation of detector - Extended source model

The previously developed MC model for detector –point like source configuration was applied to calculate the full peak energy efficiency for mixed source in voluminous phosphate matrix.

The detection efficiency was determined by changing the shape of the source and the source-detector distance. The detector geometry is given in figure III.11. The mixed source in voluminous phosphate matrix was described in section III.1.
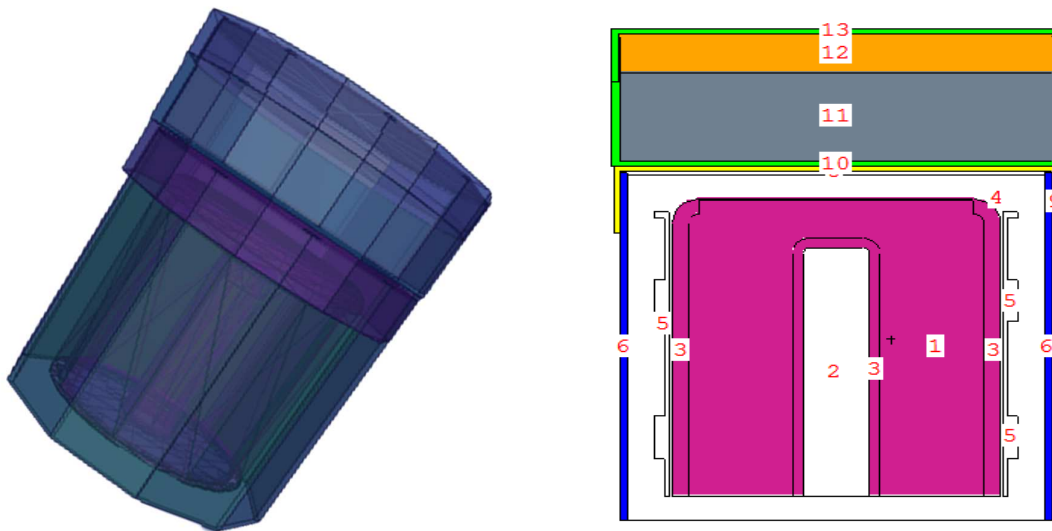
Figure III.11: Optimised detector configuration

the multi-gamma phosphate standard was sealed in a cylindrical geometry, with dimensions covering the detector surface (see figure III.11).

in order to build material card for the MCNP 5 code, ED- XRF technique was used to determine the chemical composition of the phosphate matrix. Figure III.12 shows a spectrum acquired with the ARL QUANT'X Spectrometer. In this case an excitation voltage of 50 kV, thick Cu filter and a measurement time of 300 s was used. The excellent spectral resolution and associated peak-to-background ratios allows for element lines that are well separated. The total measurement time per sample is 25 minutes. Measurement time per condition can be tailored according to specific application requirements.
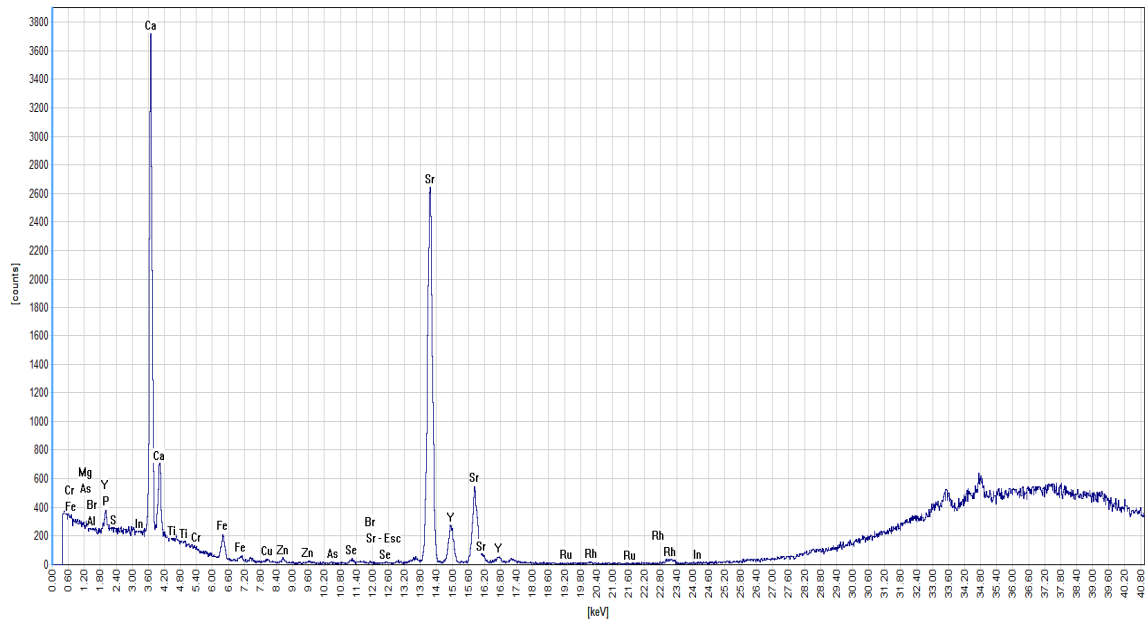
Figure III.12*: Phosphate matrix spectrum acquired with the ARL QUANT'X Spectrometer*

The obtained quantitative results used in MCNP Material card are given in table III.10. The tally inserted in the input file for phosphate voluminous source was created following the same condition as described in section III.5.

Table III.10:   Chemical composition of the phosphate matrix

Standard	Bulk Density	Composition %	
Phosphate	1.56 g/cm^3	P_2O_5	30,35
		CO_2	6,1
		SO_3	3,1
		CaO	50,95
		MgO	0,8
		Fe_2O_3	0,39
		Al_2O_3	0,42
		Na_2O	1,1
		K_2O	0,1
		SiO_2	1,85
		F	3,88

III.7.1. Validation of MCNP simulation

The experimental measurements allowed us to validate the results simulated by the MCNP5 code. The first validation step consists in simulating a qualitative spectrum of the source in order to compare it with the spectrum obtained by experiment. For this, we have introduced in SDEF card 14 gamma energies with their intensities. Figure III-13 illustrates a qualitative comparison between the simulated and measured spectrum.
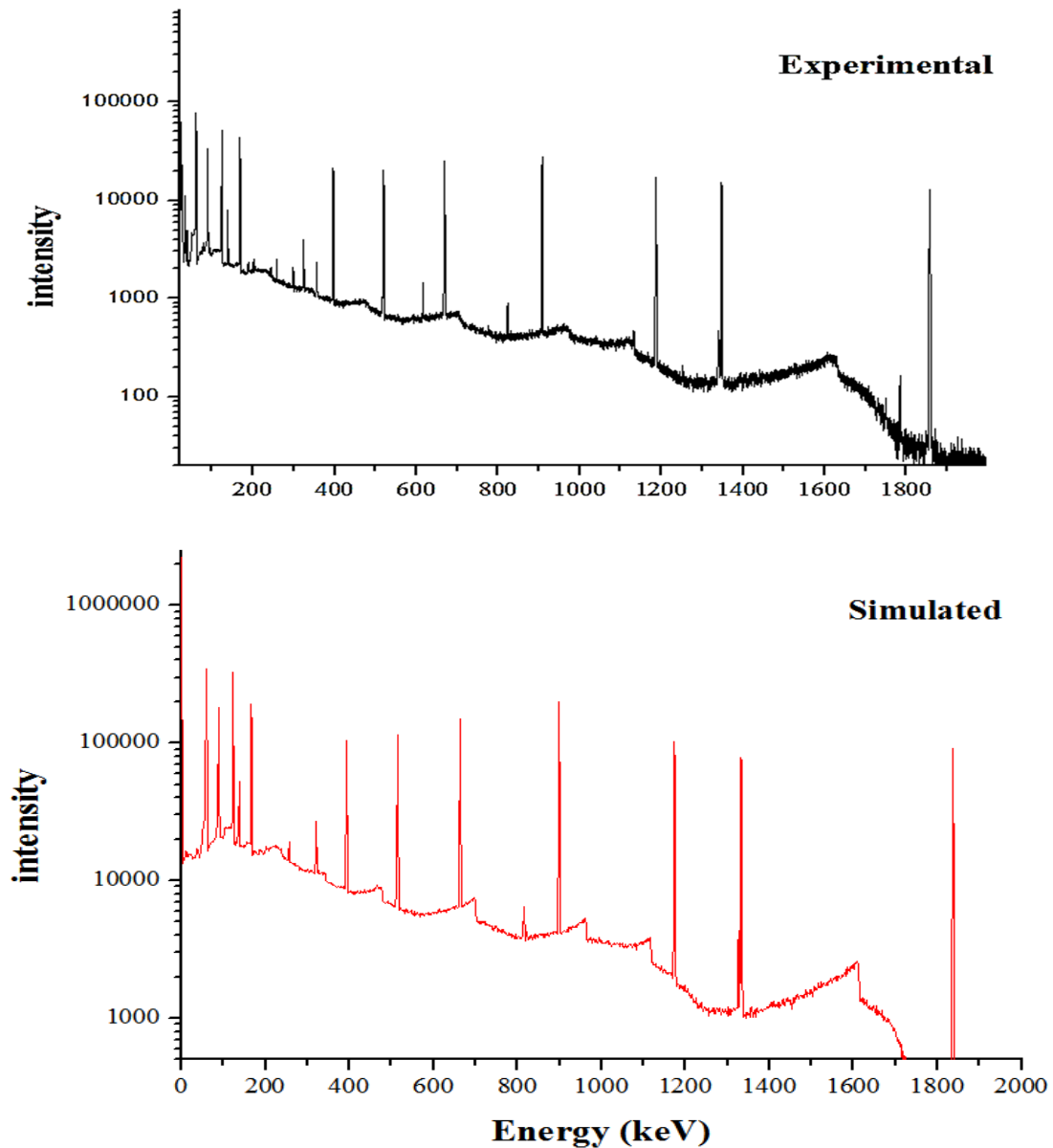
Figure III.13*: Qualitative comparison between the simulated and measured spectrum*

Once the qualitative spectrum is obtained, we proceeded to the energy-by-energy simulation to determine the simulated detector efficiencies in the phosphate matrix.

The MCNP efficiencies for the mixed source energies were computed using the optimized detector geometry. Figure III.14 shows the efficiency curves obtained experimentally and by simulation for the coaxial HPGe detector.
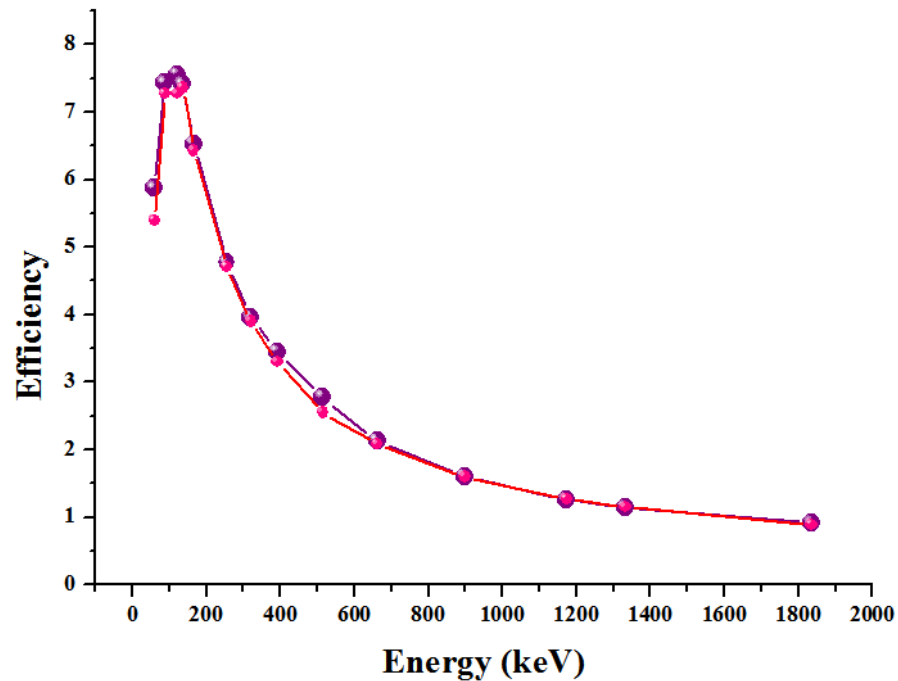
Figure III.14: Comparison between experimental and simulated efficiency for cylindrical voluminous source

Despite the change of the source shape and the source detector distance, Fig above shows that the difference between simulated efficiencies obtained from our optimized detector geometry and measured efficiencies is less than 2% on average. The agreement between simulated and experimental efficiencies is sufficiently enough to validate the model for point and extended source geometry. From the obtained results it is clear that the most effective factor which could be adjusted to optimize the detector model is the thickness of the dead layer of the detector. In addition, the detector model has to be re-adjusted with a complementary factor in order to optimize the model.

Table III.11: Comparison between experimental and simulated efficiency for cylindrical voluminous source

E (keV)	Source	ε exp %			MCNP %			RD %
[241]Am	59,54	5,87	±	0,294	5,64	±	0,054	3
[109]Cd	88	7,43	±	0,372	7,27	±	0,073	2
[57]Co	122,06	7,56	±	0,378	7,27	±	0,073	4
	136,47	7,41	±	0,371	7,36	±	0,074	1
[139]Ce	165,86	6,53	±	0,327	6,43	±	0,064	1
[113]Sn	255,17	4,77	±	0,239	4,71	±	0,047	1
[51]Cr	320,08	3,96	±	0,198	3,9	±	0,039	1
[113]Sn	391,67	3,45	±	0,173	3,38	±	0,033	4
[85]Sr	514	2,78	±	0,139	2,69	±	0,026	3
[137]Cs	661,66	2,13	±	0,107	2,08	±	0,021	2
[88]Y	898,06	1,6	±	0,080	1,68	±	0,016	4
[60]Co	1173,23	1,26	±	0,063	1,3	±	0,013	1
[60]Co	1332,49	1,14	±	0,057	1,17	±	0,012	1
[88]Y	1836,06	0,91	±	0,046	0,87	±	0,009	2

This funding implies that the accuracy of the initial model is not sufficient for the calculation of efficiency using Monte Carlo simulations. By using the optimized model, the relative deviations between experimental and simulated efficiencies are less than 4% for all measurement configurations, and the average relative deviation is less than 2%. These results demonstrate that the optimized model is precise and reliable to calculate the efficiency with photon energy in the range of 50–2000 keV using Monte Carlo simulations. Note that the relative deviation (RD) between the experimental efficiency (ε_{exp}) and the simulated efficiency ($\varepsilon_{Sim.}$) is calculated by the following formula:

$$RD = \frac{(\varepsilon_{exp}-\varepsilon_{sim})}{\varepsilon_{exp}} \times 100 \qquad (III.4)$$

III.8. Influence of Coincidence Summing effect on the efficiency

The increased solid angle of a close source-to-detector counting geometry increases sensitivity of X-ray and Y-ray spectrometry, but it also causes loss or gain of counts of emissions originating in a decay cascade. The signals of the separate emissions are treated as one and do not appear in their respective peaks. Instead, these emissions appear elsewhere in the spectrum as increased background or as virtual peak sums. The phenomenon is called coincidence summing (CS). The amount of CS, which depends on decay scheme, increases

with solid angle, because two or more emissions of a decay cascade have a greater chance of being detected together the closer the sample is to the detector.

Table III.12: Influence of Coincidence Summing effect on the efficiency

E (keV)	Source	ε_{exp} %	ε_{MCNP} %	$\varepsilon_{MCNP}/\varepsilon_{exp}$
^{241}Am	59,54	5,87	5,64	0,98
^{109}Cd	88	7,43	7,27	0,98
^{57}Co	122,06	7,56	7,27	0,96
	136,47	7,41	7,36	0,98
^{139}Ce	165,86	6,53	6,43	0,99
^{113}Sn	255,17	4,77	4,71	0,99
^{51}Cr	320,08	3,96	3,9	0,99
^{113}Sn	391,67	3,45	3,38	0,98
^{85}Sr	514	2,78	2,69	0,98
^{137}Cs	661,66	2,13	2,08	0,98
^{88}Y	898,06	1,6	1,67	1,05
^{60}Co	1173,23	1,26	1,3	1,03
	1332,49	1,14	1,17	1,03
^{88}Y	1836,06	0,91	0,87	0,95

The effect of distancing a source from a detector reduces CS by reducing solid angle but not by reducing count rate which has no effect on CS. CS is unrelated to pile-up, which is detection of two or more photons together but from different decays. The result in table III.11 were used to evaluate the CS factor calculated following the formula:

$$F_{Cs} = \varepsilon_{MCNP}/\varepsilon_{exp} \tag{III.5}$$

III.9. Influence of sample density on the efficiency

The self-attenuation correction factors for each photon energy and each sample geometry can be obtained experimentally, but this involves preparing and measuring a great number of samples of different densities. Standard radioactive samples, if available, are costly and would need to be renewed, especially when the radionuclides have short half-lives. To overcome these problems, MCNP5 simulation is the effective tool to be used. In order to evaluate the corrections for photon attenuation in typical natural samples, we performed simulations of the peak efficiency in imaginary materials with different values of the density, Table III.13 shows the simulated efficiency for the different densities

Table III.13: The dependence of density variation on the efficiency

E (kev)	Density g/cm³									
	0,6	1	1,2	1,3	1,4	1,56	1,6	1,8	1,9	2
59	6,5	6,02	5,8	5,79	5,7	5,64	5,36	5,14	5,03	4,92
88	8,29	7,87	7,65	7,55	7,44	7,27	7,23	7,01	6,9	6,8
122	8,26	7,85	7,64	7,54	7,44	7,27	7,23	7,02	6,92	6,81
136	7,74	7,58	7,5	7,46	7,42	7,36	7,34	7,27	7,23	7,19
165	7,33	6,96	6,76	6,67	6,58	6,43	6,38	6,19	6,1	6
255	5,15	4,97	4,88	4,83	4,78	4,71	4,69	4,6	4,55	4,51
320	4,1	4,02	3,98	3,96	3,94	3,9	3,89	3,85	3,83	3,81
392	3,51	3,47	3,42	3,40	3,39	3,38	3,29	3,25	3,23	3,22
514	2,74	2,7	2,68	2,67	2,66	2,65	2,54	2,53	2,52	2,51
662	2,12	2,1	2,098	2,094	2,091	2,08	2,078	2,075	2,073	2,07
898	1,75	1,71	1,70	1,69	1,68	1,67	1,59	1,56	1,54	1,53
1173	1,37	1,36	1,35	1,34	1,31	1,30	1,28	1,26	1,249	1,244
1332	1,22	1,20	1,19	1,18	1,17	1,17	1,14	1,13	1,12	1,11
1836	0,93	0,91	0,9	0,9	0,899	0,87	0,86	0,85	0,84	0,838

These values are shown as a function of the sample density for several photon energies ranging between 59 and 2000 keV.
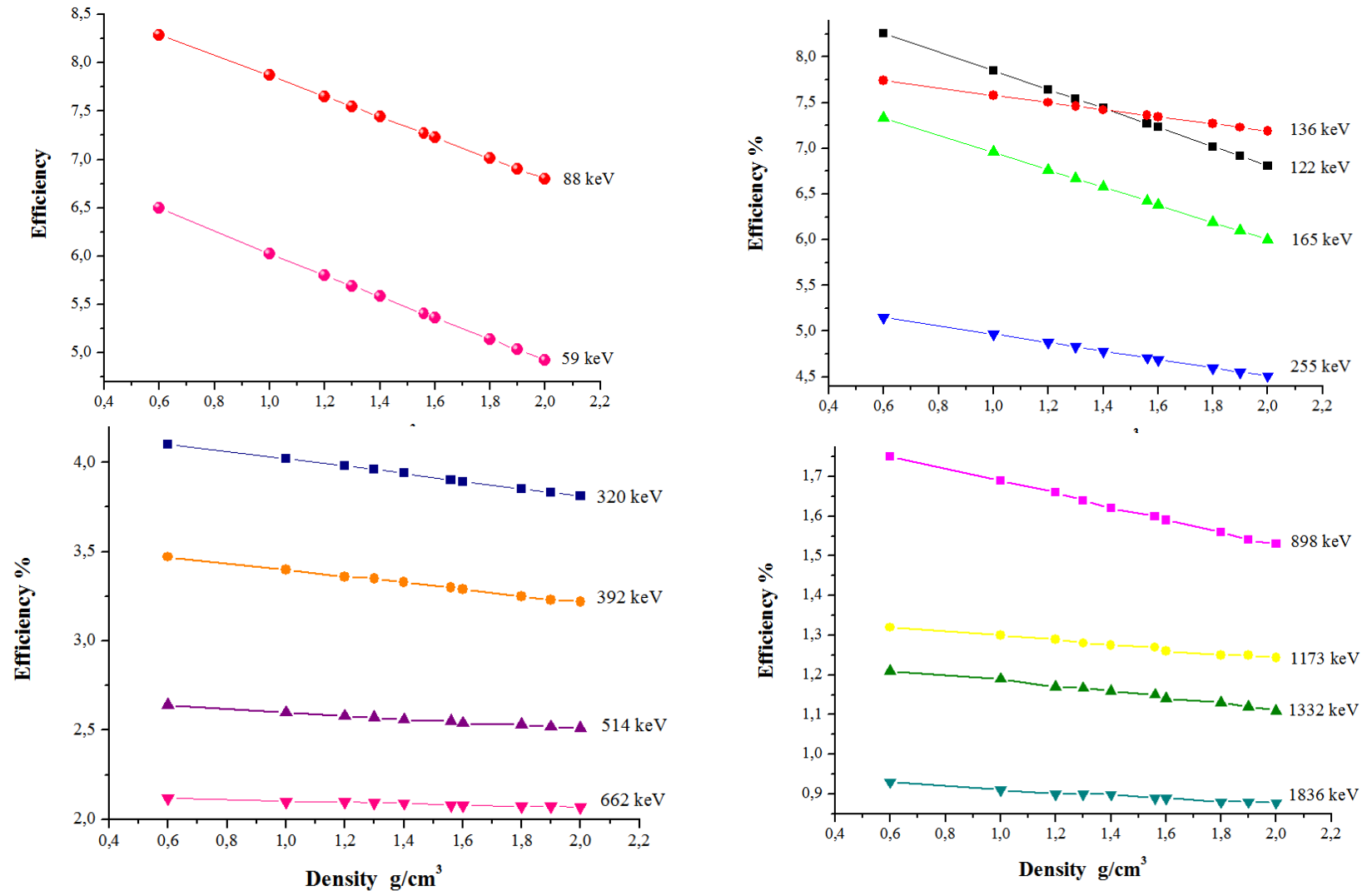
Figure III.15 : density effect on the detector efficiency

 The figure III.15 clearly shows the linear dependence of the efficiency on the density. as expected, Efficiency decreases as density increases This effect is more evident for lower energies 59 keV of ^{241}Am and 88 keV of ^{109}Cd. The self-attenuation correction factor F for a given photon energy and sample density can then be expressed as the ratio between the peak efficiencies for the sample under study and for the standard sample. for our study. We took the standard source to be an aqueous solution with a density of 1 g/cm^3.

Table III.14: Relative Self – absorption Correction factor F for this study

Source	E (kev)	Density g/cm3		
		1 (water)	1,56 (Phosphate)	F
^{241}Am	59	6,02	5,64	0,90
^{109}Cd	88	7,87	7,27	0,92
^{57}Co	122	7,85	7,27	0,92
	136	7,58	7,36	0,93
^{139}Ce	165	6,96	6,43	0,92
^{113}Sn	255	4,97	4,71	0,95
^{51}Cr	320	4,02	3,9	0,97
^{113}Sn	392	3,4	3,38	0,98
^{85}Sr	514	2,6	2,65	0,98
^{137}Cs	662	2,1	2,08	0,99
^{88}Y	898	1,69	1,67	0,99
^{60}Co	1173	1,3	1,38	0,99
	1332	1,19	1,17	0,98
^{88}Y	1836	0,91	0,87	0,98

It is clear that the photon attenuation effects increase considerably with decreasing energy in the region of energies less than 300 keV. An obvious consequence to be drawn from these results is that the self-attenuation correction factors for a particular measuring geometry can be precisely obtained by means of Monte Carlo simulation. And hence, the activity concentration Formula after The self-attenuation correction and Coincidence Summing Correction could be calculated using the following relation:

$$A_s = \frac{N}{\varepsilon\, \gamma\, F\, F_{Cs} t_c\, m}$$

(III.5)

F is self-attenuation correction factor and F$_{Cs}$ is the Coincidence Summing Correction factor.

Chapter IV

Application: Case of phosphate open pit mine

The optimized model will be applied for the establishing of a first of kind NORM distribution in a non-exploited phosphate open pit mine (Bled El Hadba). Radioactivity of K-40. U-235. U-238. Ra-226 and Th-232 will be used to the assessement of radiological hazard in the area and then subjected to statistical analyses for the sake of drawing a valid conclusion vis-à-vis the nature and the significance of the radioactive elements' distribution in Bled El-Hadba phosphate deposits.

IV.1. Geological setting of study area

As an operational open-pit mine since 1965. Djebel Onk site constitutes the most important phosphate deposits in Algeria. both for its reserves and for its ease of access and exploitation. Algerian deposites are located in Tébessa region in the eastern Saharan Atlas. at about 600 kilometers southeast the capital city Algiers [34.35].
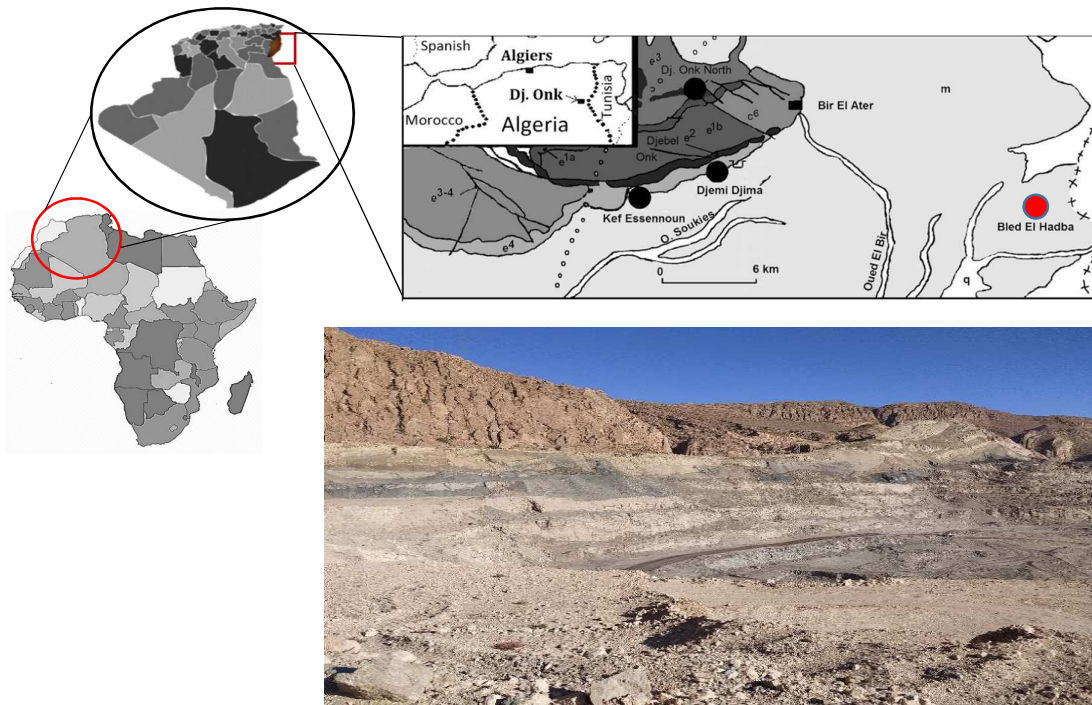
Figure IV. 1. Geological setting of Bled El-Hadba open mine

Phosphates in Tébessa region are a part of a large period of marine phosphatogenesis that occurred in the Tethys Ocean. the host sedimentary formation exist in tertiary marine deposits of the Late Paleocene to Early Eocene ages. During the late Paleocene – early Eocene era. Djebel Onk region belonged to the western part of Gafsa-Metlaoui-Djebel Onk basin. but Dj. Onk basin was distinguished by an important subsidence. which explains the enormous tonnage of the phosphates [36-38]. The phosphate site of Bled El-Hadba is located at the eastern edge of the Saharan Atlas in Tébessa region of Algeria. The phosphate ore deposit is located 14 km to the south-east of Bir El Ater. 14 km from the Djebel Onk treatment plant on the western side of the Djebel Zerga anticline structure. and about 6 km from the Algerian-Tunisian border

(Fig. 1.). The geology of the area was sufficiently described [39.40]. Bled El-Hadba deposit is composed of three main layers whose average thickness is as follows:

- a 6 m deep lower (basal) layer of phosphate. that is deficient in phosphorus pentoxide (P_2O_5) and very dolomitic;

- a 16 m main layer of phosphate. that is rich in P_2O_5 and not very dolomitic;

- 7 m thick very dolomitic top phosphate layer. which is poor P_2O_5.

The facies are generally beige to brown and dark grey to black in the base of the layer. Colour variations are related to organic matter content [40].

IV.2. Sampling and processing

21 samples were collected from the predefined mine.

Figure IV.2. Sampling procedure

The sampling scheme was implemented based on the differences in the facies. It allowed the determination of the correlations between the investigated parameters and both the geological and the geographical features of the mine.
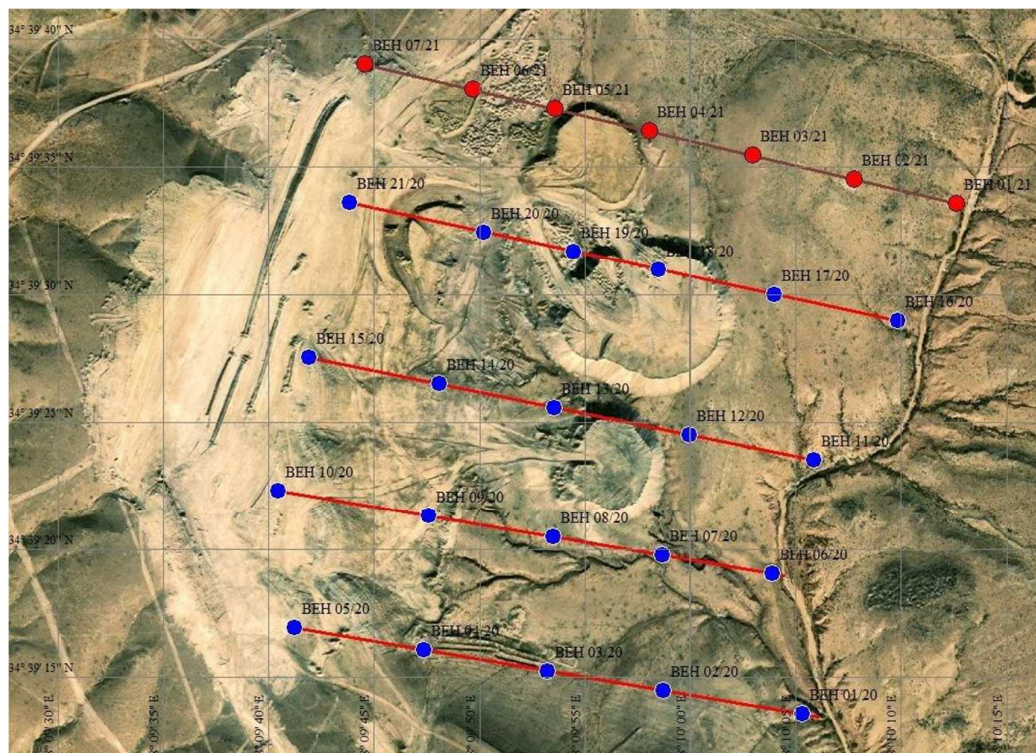
Figure IV.3:.Sampling scheme

The samples were crushed and sieved to fine powder and then packed in a standard cylindrical Petri container.

Figure IV.4.Sample preparation

These containers were hermetically sealed and left for at least 4 weeks (>7 half-lives of ^{222}Rn and ^{224}Ra) before being counted by gamma spectrometry in order to ensure that the daughter products achieve equilibrium with their respective parent radionuclide. The qualitative spectrum of one sample is illustrated in the figure bellow
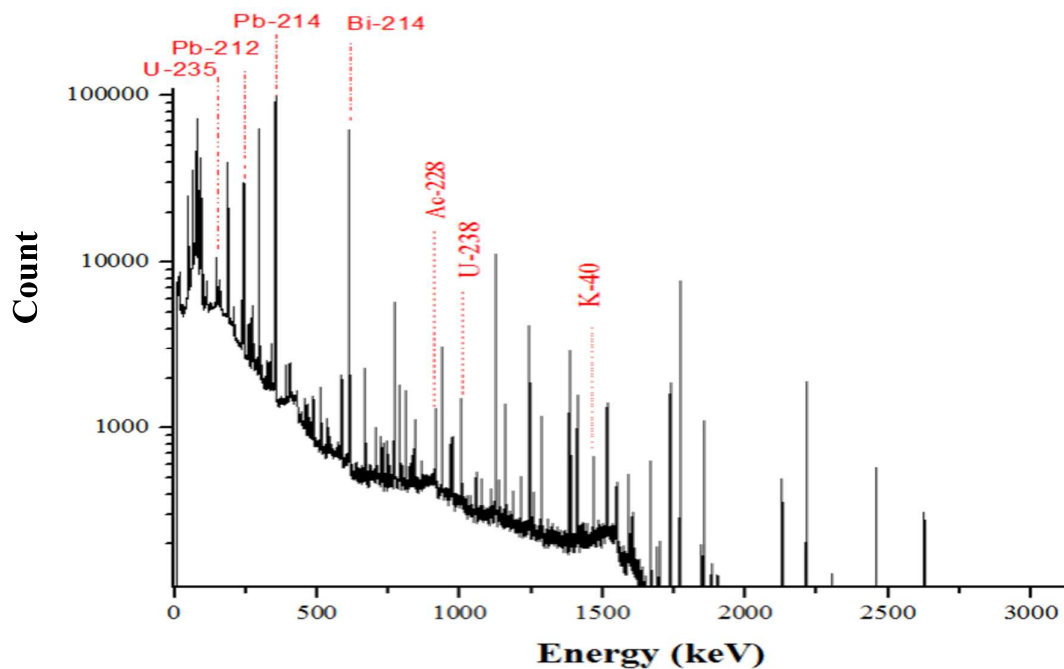
Figure IV.5. *Qualitative spectrum of phosphate sample*

IV.3. Radioactivity measurements

The laboratory environmental γ-ray background was measured during 10 days using the same standard plastic container under identical measurement conditions for background subtraction. After that. all the 21 prepared samples were counted for 24 h under the same counting geometry used for the standard source. The activity concentrations of ^{226}Ra. ^{238}U. and ^{232}Th in each sample can be estimated indirectly. via several gamma-ray lines from their decay products under the assumption of secular equilibrium. The gamma-ray lines at 351.9 keV (37.1%) from ^{214}Pb. and at 609.3 keV (46.1%) from ^{214}Bi were used to assess ^{226}Ra activities. Moreover. ^{232}Th activities were estimated using gamma-ray lines at 911.2 keV (29%) from ^{228}Ac and at 238.6 keV (43.6%) from ^{212}Pb.

The activity concentration of ^{238}U was measured from the γ-ray line [1001 keV (0.6%)] of ^{234m}Pa. which is the immediate daughter of ^{234}Th as it is together with ^{234m}Pa. the best suited radioisotopes for the estimation of ^{238}U. Activity of ^{40}K and ^{235}U were directly determined by

measurement of the single gamma line at 1460.8 keV (10.6%) and 143.76 keV (10.96%) respectively.

the activity concentration of the radionuclides found in the samples was calculated using the following relation:

$$A_s = \frac{N}{\varepsilon \gamma t_c m}$$ (IV.1)

The uncertainty associated with the activity concentration is given by error propagation law according to the following relation:

$$\sigma A = A \sqrt{(\frac{\sigma \varepsilon}{\varepsilon})^2 + (\frac{\sigma N}{N})^2 + (\frac{\sigma \gamma}{\gamma})^2 + (\frac{\sigma t_c}{t_c})^2}$$ (IV.2)

where N is the counting rate for a specific gamma line (count per second) corrected for background. ε is the absolute photo-peak efficiency determined after plotting the efficiency curve. taking into account the self-attenuation of gamma rays and coincidence summing correction . γ is the absolute intensity of the considered gamma-ray line (branching ratio). t_c is the counting time in (s) and m is the sample mass in (kg).

IV.3.1. Activity concentrations of NORM

The distribution and average activity concentrations of NORM in phosphate samples collected from twenty-one (21) point are presented in Table V.1. All values are given in Bq kg^{-1} of dry weight. The activity concentration ranges are 37 ± 2 to 176 ± 10 Bq/kg with an average of 81 $\pm$ 18 Bq·kg^{-1} for Potassium. The measured average activity concentration of ^{235}U. ^{232}Th are respectively 52 ± 8 and 66 ± 6 Bq·kg^{-1}. The thorium-232 shows a high concentration in BEH-2 (85 ± 5 Bq·kg^{-1}). whereas it occurs in small concentrations in BEH-21 (14 ± 1 Bq·kg^{-1}).

The highest concentration for ^{235}U is recorded for BEH-8 (229 ± 13 Bq·kg^{-1}) and the smallest content was found in BEH-21 (7 ± 1 Bq·kg^{-1}). Low ^{235}U contents are attributed to its low natural abundance which is lower than (0.75%). ^{238}U and ^{226}Ra average activity concentrations are 788 $\pm$ 280 and 570 $\pm$169 Bq·kg^{-1} respectively. It is clear that from the results that ^{238}U shows the highest activity concentrations and is the most dominant in all samples due to the accumulation of dissolved uranium and its products. in the form of uranyl complex during the geological formation of the phosphate deposits [37]. except for sample BEH-19 where the activity

concentration of [226]Ra is greater than that of [238]U. This is may be due to the migration of uranium from phosphate rocks of sedimentary origin [38]. The concentration of [238]U in the worldwide phosphate deposits varies in a wide range from 40 to 4.800 Bq·kg^{-1}. Therefore. the results measured here for the 21 samples of phosphate were significant from the radioactivity point of view.

Table IV.1. Activity concentrations (Bq·kg^{-1}) of [238]U. [232]Th. [40]K. [226]Ra. [235]U in Phosphate samples from Bled El-Hadba deposit.

Sample code	^{40}K	^{235}U	^{238}U	^{232}Th	^{226}Ra
BEH-01	37 ± 2	36 ± 3	507 ± 50	71 ± 4	384 ± 20
BEH-02	176 ± 10	44 ± 3	653 ± 56	85 ± 5	487 ± 25
BEH-03	144 ± 9	48 ± 4	859 ± 70	67 ± 4	587 ± 31
BEH-04	87 ± 5	30 ± 2	429 ±42	55 ± 3	366 ± 19
BEH-05	96 ± 6	38 ± 3	688 ± 58	53 ± 3	489 ± 25
BEH-06	113 ± 7	32 ± 3	579 ± 50	59 ± 3	385 ± 20
BEH-07	103 ± 6	65 ± 4	940 ± 72	39 ± 2	795 ± 41
BEH-08	113 ± 8	229 ± 13	3475 ± 205	73 ± 4	2115 ± 110
BEH-09	168 ± 10	41 ± 2	609 ± 55	64 ± 3	440 ± 23
BEH-10	54 ± 4	45 ± 3	710 ± 61	69 ± 4	490 ± 25
BEH-11	44 ± 3	45 ± 3	714 ± 64	79 ± 4	459 ± 24
BEH-12	68 ± 4	38 ± 2	684 ± 58	73 ± 4	445 ± 23
BEH-13	53 ± 4	42 ± 3	626 ± 54	71 ± 3	462 ± 24
BEH-14	47 ± 3	40 ± 2	592 ± 52	71 ± 4	431 ± 22
BEH-15	69 ± 4	42 ± 3	628 ± 58	71 ± 4	457 ± 24
BEH-16	57 ± 4	38 ± 3	622 ± 56	68 ± 4	444 ± 23
BEH-17	61 ± 4	65 ± 4	975 ± 78	80 ± 4	739 ± 38
BEH-18	68 ± 5	59 ± 4	956 ± 72	76 ± 4	737 ± 38
BEH-19	35 ± 2	57 ± 4	608. ± 58	66 ± 3	737 ± 38
BEH-20	64 ± 4	38 ± 3	567 ± 54	69 ± 3	447 ± 23
BEH-21	42 ± 3	7 ± 1	133 ± 20	14 ± 1	83 ± 4
Mean	81 ± 18	52 ± 8	788 ± 280	66 ± 6	570 ± 169
SD	42	43	643	16	388
CV%	51	82	81	23	67

SD : Standard Deviation . CV : coefficient of variability (CV= SD/mean*100). The uncertainty on the mean value is calculated following the formula: $\overline{X \pm t_{ddl}^{\alpha=0.05}(\frac{SD}{\sqrt{N}})}$. The calculated uncertainty results are less than 5%. which is good in gamma spectrometry and envisage the accuracy of the technique. The computed coefficient of variability (CV %) of the radioactive variables exhibits a greatly high value (82 %) for Uranium when compared with Radium (64.7%). A higher coefficient of variability implies a lower degree of homogeneity. The observed relative tendency of uranium-238 towards heterogeneity is interpreted to be attributed to the relatively higher accumulation of U-238 in different layer. This difference could reveal to a probable disequilibrium between U and Ra in the deposit.

Table IV.2. allows one to compare the activity concentrations of ^{238}U. ^{232}Th and ^{40}K in phosphate samples of Bled El-Hadba mine to contents from other studies for different phosphate deposits in the world.

As it can be inferred from the previous table. the activity concentration of ^{226}Ra is much lower than the values reported for Morocco. Tunisia. South Africa. Sudan and Western Sahara. but higher than those reported for Egypt. China. Finland and Russia

Table IV.2. Activity concentrations of ^{226}Ra. ^{235}U. ^{238}U. ^{232}Th and ^{40}K in phosphate deposits from different countries.

Country	Activity concentration (Bq·kg^{-1})					Reference
	^{40}K	^{232}Th	^{235}U	^{238}U	^{226}Ra	
China	-	25	-	150	150	[41]
Egypt	21.4	23.7	-	408	287	[42]
Finland	110	10	-	-	10	[41]
Russia	40	80	-	40	30	[41]
Morocco	10	30	-	1600	1700	[43]
Nigeria	40	20	-	-	558	[44]
Pakistan	206	52	-	550	511	[41]
Saudi Arabia	250	40	-	-	519	[45]
South Africa	4	30	-	1300	1100	[41]
Sudan	52	3		2598	2263	[46]
Tunisia	32	29	-	580	821	[41]
turkey	256	26	-	557	625	[47]
USA /Florida	-	16	-	1500	1600	[41]
Western Sahara	30	7	-	900	900	[41]
Algeria	**81.29**	**65.53**	**51.75**	**788.34**	**570.47**	**Present study**

[232]Th activity concentrations reported in all mentioned countries are lower than our values excluding Russia which shows high values.

The maximum value of ^{40}K activity in the present study is much higher than the values reported for African countries. but lower than the ones reported for Asian countries.

The occurrence of radionuclides at different sampling sites worldwide is mainly due to the geological and geographical differences between the mining areas. and to the variations of chemical and mineral facies for the considered regions.

IV.3.2. Activity Ratios

The variations of concentration ratios were also calculated and reported previously in table IV.3.

Table IV.3: Activity ratio

Sample code	$^{232}Th/^{238}U$	$^{226}Ra/^{238}U$	$^{235}U/^{238}U$
BEH-01	0.1	0.8	0.070 ± 0.01
BEH-02	0.1	0.8	0.067 ± 0.01
BEH-03	0.08	0.7	0.055 ± 0.01
BEH-04	0.1	0.9	0.069 ± 0.01
BEH-05	0.08	0.7	0.055 ± 0.01
BEH-06	0.1	0.7	0.055 ± 0.01
BEH-07	0.04	0.9	0.069 ± 0.01
BEH-08	0.02	0.6	0.065 ± 0.01
BEH-09	0.1	0.7	0.067 ± 0.01
BEH-10	0.1	0.7	0.063 ± 0.01
BEH-11	0.1	0.6	0.063 ± 0.01
BEH-12	0.1	0.7	0.055 ± 0.01
BEH-13	0.1	0.7	0.067 ± 0.01
BEH-14	0.1	0.7	0.067 ± 0.01
BEH-15	0.1	0.7	0.066 ± 0.01
BEH-16	0.1	0.7	0.061 ± 0.01
BEH-17	0.08	0.8	0.066 ± 0.01
BEH-18	0.08	0.8	0.061 ± 0.01
BEH-19	0.1	1.2	0.090 ± 0.03
BEH-20	0.1	0.9	0.067 ± 0.01
BEH-21	0.1	0.6	0.052 ± 0.01
Mean	0.1 ± 0.01	0.7 ± 0.05	0.060 ± 0.02
SD	0.03	0.13	0.008
CV%	28	16	12

<u>^{232}Th/^{238}U</u>

^{38}U and ^{232}Th series commonly occur together in nature. Th/U ratio geochemically reflects any natural depletion or enrichment in uranium and is used also as an indicator of oxidizing and reducing conditions. The analysis of ^{232}Th/^{238}U activity ratio variations revealed that ^{238}U concentration is enriched with respect to ^{232}Th. ratios were found in the range of 0.02−0.14 with an average of 0.1. The average Th/U ratio in sedimentary phosphate rocks is usually around 0.07. When the Th/U ratio is lower than 0.07. an enticement of uranium can be observed [48]. values of Th/U were found to be lower than 2 suggesting that uranium is present in the concentrated form (in higher abundance compared to thorium) [49.50].
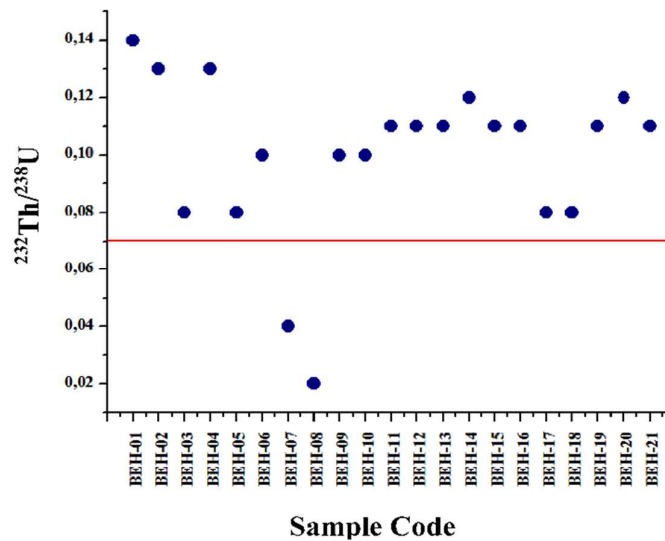
Figure IV.3.*^{232}Th/^{238}U ratio*

The abundances of thorium and uranium normally increase as the pH of the medium where they occur shifts from alkaline to acidic facies. Uranium migrates and moves quicker in the presence of oxygen while thorium is insoluble in an oxidizing medium. An increase in rainfall may lead to more effectiveness in uranium transport and leaching activities. leading with time to an increase in U concentrations in the lowest areas [48].

$\underline{^{226}Ra/^{238}U}$

$^{226}Ra/^{238}U$ ratios are lower than unity for almost all samples. The equilibrium ($^{226}Ra/^{238}U =1$) is not always maintained. Disequilibrium is more frequent and is greater in the superficial part of the deposit than at a depth of more than 10 m. Radioactive disequilibrium or precisely a $^{226}Ra/^{238}U$ ratio lower than 1. arises in the natural radioactive series due to many reasons. The alternative is that there has been a leaching of radium. due to the higher solubility and mobility of ^{226}Ra relative to ^{238}U in the weathering process. confirming their different chemical behaviour in weathering profiles [51].

If secondary U minerals are present in the oxidized zones. Ra might also be leached from these minerals resulting in a net Ra depletion [52].
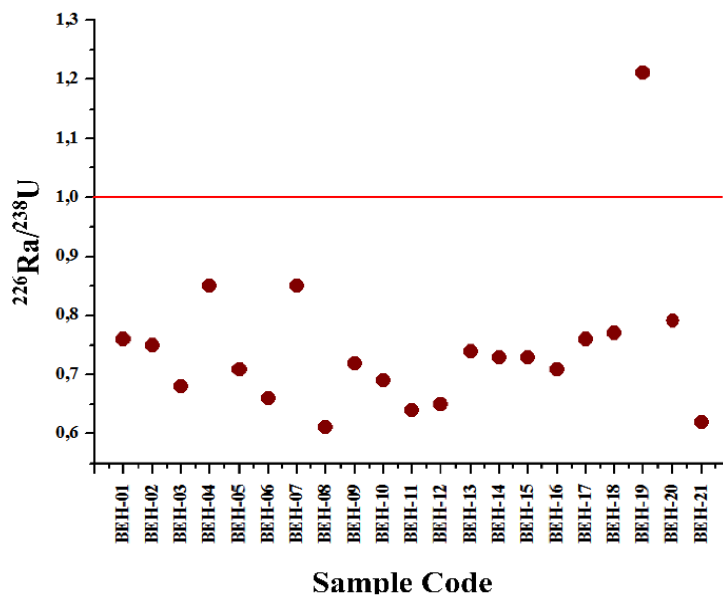
Figure IV.4*. $^{226}Ra/^{238}U$ ratio*

Other reason is the presence of uranium fixative agent such phosphate (P_2O_5) in large amount. Even a recent fractionation (crashing) events could lead to the loss or gain of radionucleides that are mobile in the ambient environmental conditions.

$^{235}U/^{238}U$

The variation of $^{235}U/^{238}U$ has been used as an indicator of natural or anthropogenic contribution of U. Therefore. depletion or enrichment of ^{235}U can be used as a typical fingerprint that allows one to distinguish between natural. enriched and depleted U [53].
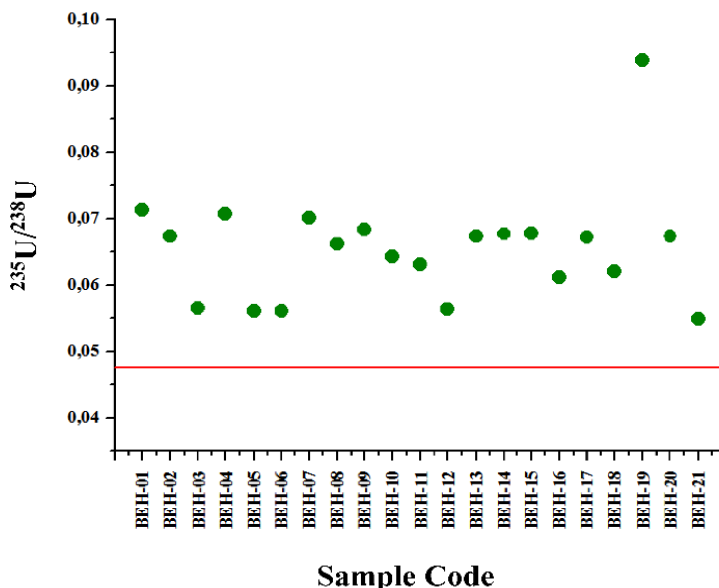
Figure IV.5. $^{235}U/^{238}U$ ratio

An anthropogenic source of U can be detected by slight change of the natural $^{235}U/^{238}U$ that is equal to 0.046 for natural sample. For the phosphate samples that were analysed in the present work. the average value of $^{235}U/^{238}U$ is 0.06.

It appears that the measured value deviates from the natural value of (0.046). This discrepancy is mainly due to the fact that ^{238}U was significantly depleted with respect to ^{235}U. Isotopic ratio can potentially provide an important tool for tracing migration of uranium series radionuclides and transport of groundwater from different aquifers [54].

In closed geological systems, Isotopic ratios of natural radionuclides are preserved. but If the system underwent weathering and various physiochemical conditions, the isotopic ratio will be higher or lower than unity; and this depends on leaching, erosion, and daughter half-life [55]. ^{235}U $/^{238}U$ ratios vary also as a function of uranium fractionation [56].

Table IV.4. [235]U/[238]U activity ratio variation from different environmental sample around the world

Country	sample type	[235]U/[238]U activity ratio	Ref
Syrian coastal area	Phosphate	0,056	[55]
Egypt	Sediments	0,11	[57]
Jordan	Sediment	0,03- 0,06	[58]
Ghana	Groundwater	0,004 - 0,1	[59]
Poland	Soil	0,02-0,09	[60]
Algeria	Phosphate (Altered rock)	0,097	[12]
Morocco	Apatite phosphate	0,07	[43]
china	Plant	0,01-0,1	[61]
Present study	phosphate	0.06	-

Table bellow show the variation of [235]U/[238]U variation from some environmental sample around the world. Results with higher [235]U/[238]U activity ratio could be explained by the enrichment of uranium -235 by the presence of a sorbent (such as the appatite) characterizing the geological region. The mechanism of U isotopes immobilization in apatites or their modifications has a significant influence on the accumulation of autogenic U excess [62]. The activity ratio deviation occur in presently hyper arid regions, some layers may have been altered by meteoric water after deposition [63].

IV.4. Validation of the results accuracy

Radioactivity measurement for both Th-232 and U-238 are compared to the value obtained by Instrumental Neutron Activation Analysis (INAA) which is reported to be the more sensitive and non-destructive nuclear technique and generally used as a reference method to test the accuracy of other analytical methods.

IV.4.1. Instrumental Neutron Activation Analysis

To determine the accuracy and reliability of our technique. only 5 samples from different layer were selected measured using INAA. 80 mg of each phosphate sample were placed in small aluminum packs (1 cm × 1 cm).

Figure IV.8. *Sample preparation for INAA analysis*

The samples were prepared and packed together with standard reference material in a capsule and simultaneously irradiated in NUR reactor under a thermal – epithermal flux of $5.22\ 10^{12}$ ncm^{-2} s^{-1} during 04 hours for medium lived radionucleid. The irradiated samples were measured for 3000s using gamma-ray spectrometry technique based on HPGe detector after a cooling time of 5 days. The relative méthode was used for the determination of uranium using the energy 277.59 of Np-239 following the formula II.13. And absolute method for thorium concentration via the energy 311.9 keV of Pa-233 using the formula II.12. The results are given in ppm and converted to Bq/kg via the following relation:

$$-\frac{dN}{dt} = -\frac{ln\,2}{(t_{1/2})}\frac{m\theta N_A}{M_R}$$

With : θ isotopic abundance, N_A: Avogadro Number, M_R: atomic mass

Table IV.5. Gamma spectrometry versus INAA result for uranium and thorium

	^{238} U (Bq/kg)		^{232} Th (Bq/kg)	
Sample code	**G.S**	**INAA**	**G.S**	**INAA**
BEH-4	428.81	504.91	54.99	65.78
BEH-5	687.95	558.1	53.48	62.94
BEH-7	940.44	975.03	38.78	43.45
BEH-10	710.13	694.2	69.14	66.39
BEH-15	627.69	619.01	71.48	73.5

A good agreement was found between the results of ^{232}Th and ^{238}U obtained by Gamma spectrometry and INAA.
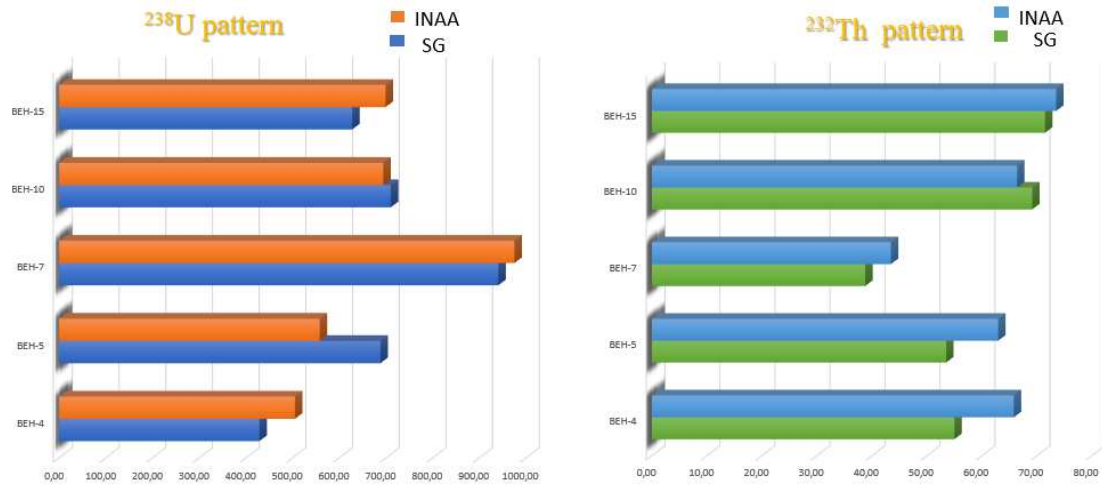

Figure IV.9. INAA vs. Gamma spectrometry results

A good correlation is observed which confirms the authenticity of Gamma Spectrometry technique/procedure used for the determination of ^{232}Th . ^{238}U in phosphate samples.
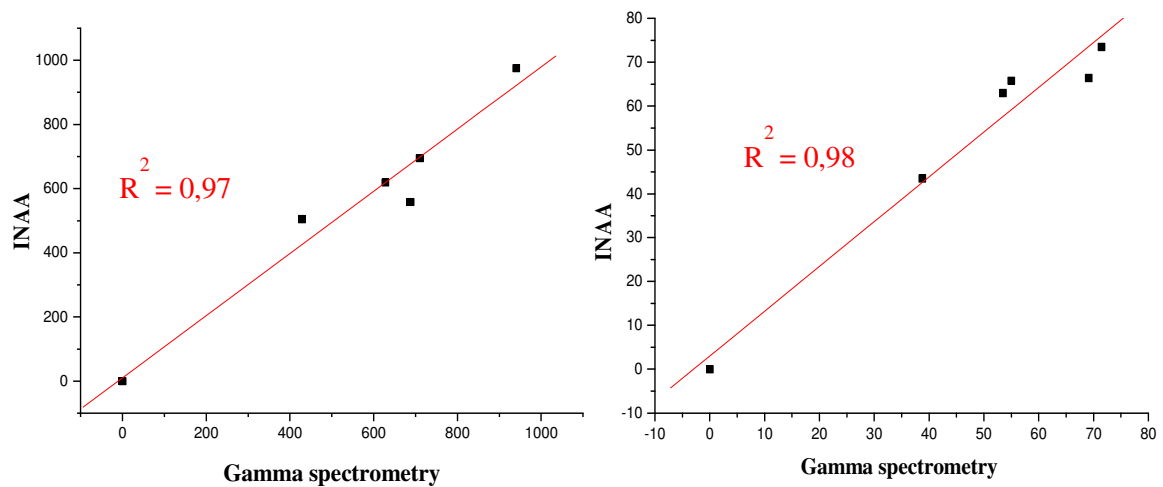

Figure IV.10. INAA vs. Gamma spectrometry correlations

IV.4.2. Interpolation of the radiological maps

In this study. the spatial variations of natural radionuclide concentrations in phosphate were interpolated and mapped by means of ArcGIS® software by Esri. It provides a variety of methods. where. each of them is more applicable for specific data types. The geostatistical methods such as kriging are more advanced and are based on statistical models that include autocorrelation making them capable of providing some measure of the certainty of the interpolation [64]. This method utilizes the neighbouring measurements weighted by direction and distance while building its own spatial correlation configuration when predicting of the interpolated locations. Combining the use of kriging as an interpolation technique; with high-resolution gamma spectrometry measurements was an approach that enabled the generation of smooth maps for the identified radionuclides concentrations for the mining site. In this study. the spatial distribution of natural radionuclide activity concentrations in Bled El-Hadba deposit. were interpolated and mapped by means of ArcGIS™.

Table IV.6 . Distribution of radioelements according to the type of sedimentary phosphate

Type of sedimentary phosphate	No. station	\(^{40}\)K	\(^{235}\)U	\(^{238}\)U	\(^{232}\)Th	\(^{226}\)Ra
		Activity concentration				
phosphate limestone; top layer of the deposit	4	106 ± 58	93 ± 98	1383 ± 1499	62 ±17	934 ±961
loose and friable phosphate limestone	1	176	44	652.62	85	487
Brownish phosphate limestone	1	143	48	859.1	66	586
Phosphate limestone (main layer)	1	87	30	428.81	55	365
Phosphate limestone (main horizon of the Thanetian)	2	105 ± 56	35 ± 19	634± 242	56 ± 18	437 ± 328
Main limestone layer extending to the surface	5	54 ± 8	42 ± 3	665 ± 48.7	73 ± 3	458 ± 20
Phosphate limestone	6	59 ±10	50 ± 9	726 ± 149	72 ± 4	594 ±125
Phosphate (basal layer)	1	42	7	133	14	82

* $\overline{X} \pm t_{ddl}^{\alpha=0.05}\left(\dfrac{SD}{\sqrt{N}}\right)$ t: one tail probability at 0.05 ddl : degree of freedom equal to (N-1). sd: standard deviation.

N: number of similar station

Table IV.6. and the interpolated maps in Figure IV.11 to IV.15. show widespread distributions of the measured data of the radionuclides ^{226}Ra. ^{235}U. ^{238}U. ^{232}Th and ^{40}K due to varied phosphate types. geology. and geographical configurations.
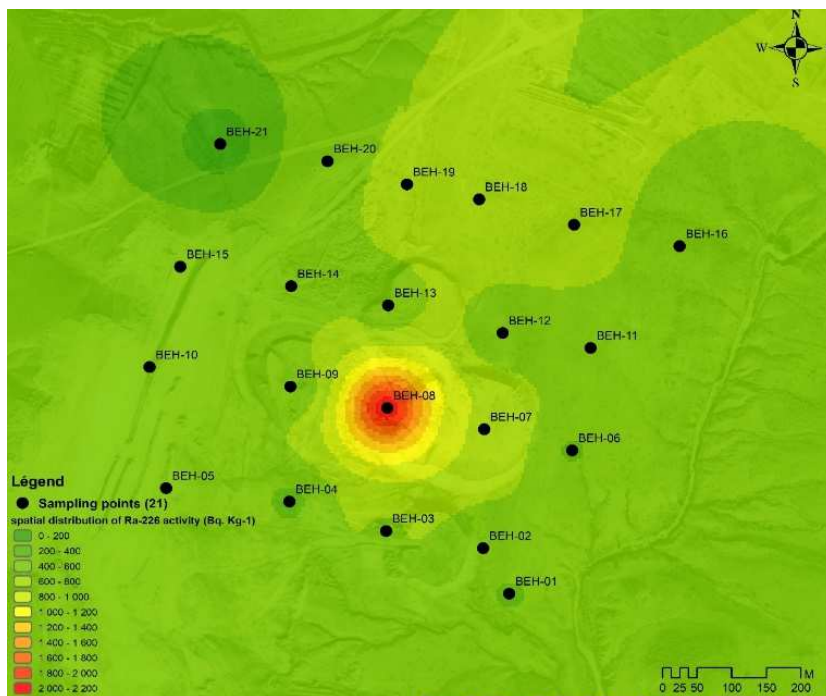
Figure IV.11.*Radium spatial distribution*
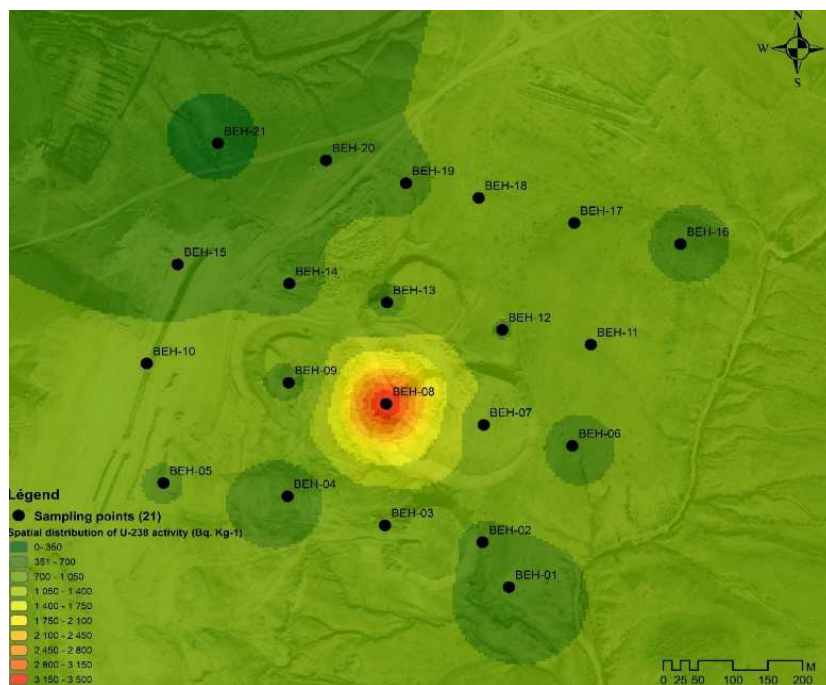
Figure IV.12.*U-238 distribution*
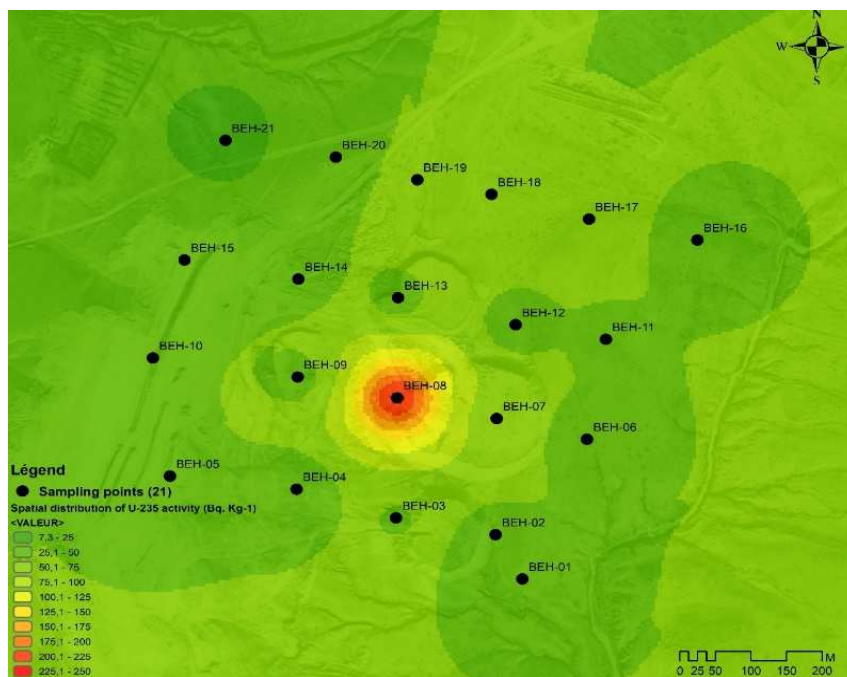
***Figure IV.13**.U-235 distribution*

Figures above shows that. in general. ^{226}Ra. ^{235}U. ^{238}U. activity is increasing from the basal layer to the uppermost phosphate beds. This is mainly due to the spread of P_2O_5-rich rock compositions. The spatial distributions of thorium and potassium in Figure below. seem to depend also on the sedimentological aspect of the open pit mine.
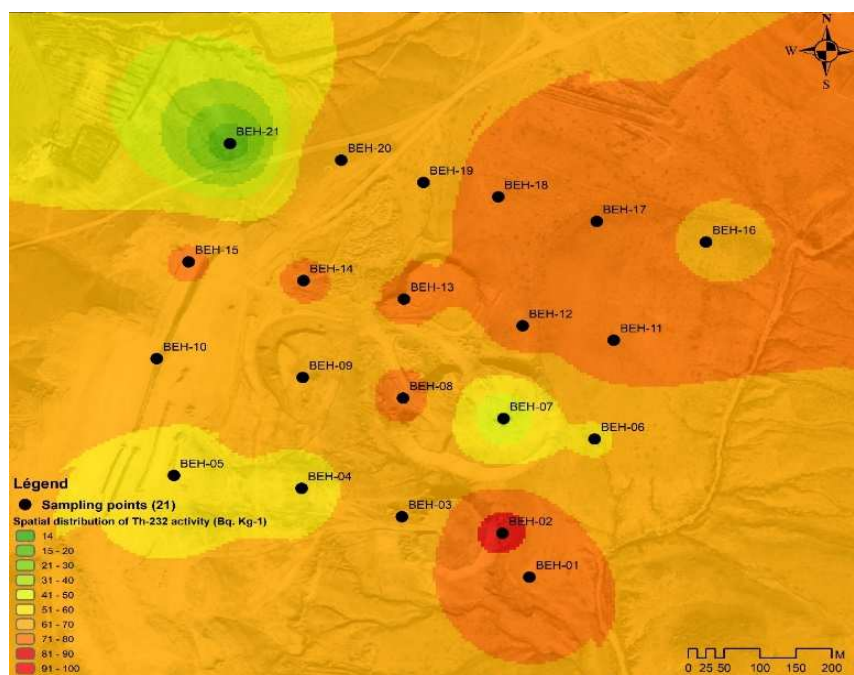
***Figure IV.14.**.Th-232 distribution*
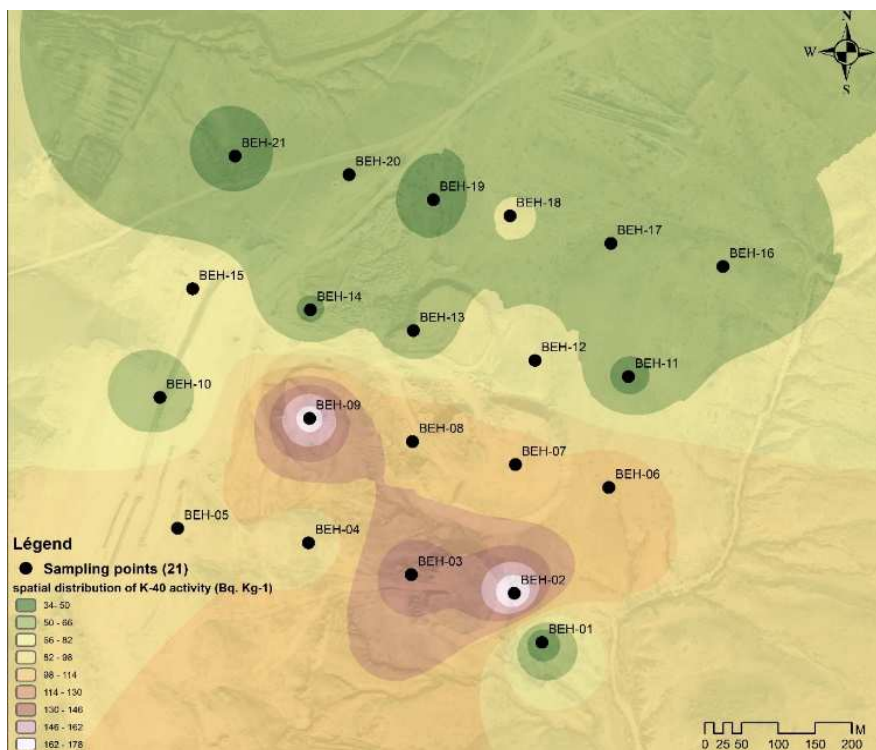
Figure IV.15..K-40 distribution

The highest concentration of ^{232}Th and ^{40}K was detected in the loose and friable phosphate limestone layer. Activity concentration values of NORMS in phosphate deposits from various countries of the world vary from country to other and region to region even within same country. Table IV.3 allows one to compare the activity concentrations of ^{238}U. ^{232}Th and ^{40}K in phosphate samples of Bled El-Hadba mine to contents from other studies for different phosphate deposits in the world.

IV.5. Determination of radiological hazards

The humans working in the open-pit mine area involved in mining. milling and processing of Phosphate rock are affected from the radiological hazard of NORM by various means. Radiological hazard is assessed by taking into account the measured activity concentration of ^{238}U. ^{232}Th and ^{40}K. Radiologic hazard can be estimated through various criteria. In the present study. only outdoor external dose rates and the associated annual effective dose was considered for the mineworker.

IV.5.1. Outdoor external dose rate

The measured activity of ^{238}U. ^{232}Th and ^{40}K were converted into doses by applying the factors 0.462. 0.604 and 0.0417 respectively following the equation [65-67]:

$$\text{D (nGy/h)} = 0.462 \ A_{Ra} + 0.604 \ A_{Th} + 0.0417 \ A_{K} \qquad \text{(IV.3)}$$

These factors were used to calculate the external gamma dose rate (D) at 1.0 m above ground level. Based on the calculated dose rate values. the annual effective dose was determined for the mineworkers of the study area.

IV.5.2. Effective dose

The annual effective dose from external exposure to gamma rays emitted from Phosphate rock can be determined using the following relation [65]:

$$\text{E (mSv/y)} = D \ (nGy \ .h^{-1}) \times 8760 \ (h/y) \times 0.7 (Sv.Gy^{-1}) \times 0.4 \times 10^{-6} \qquad \text{(IV.4)}$$

The annual estimated average effective dose received by a member is calculated using a conversion factor of 0.7 Sv·Gy^{-1} which is used to convert the absorbed rate to an annual effective dose. Miners in the area spends about 9h working. equivalent to an outdoor occupancy of 40% [29.33-36]. The dose parameters obtained from the 21 phosphate samples are presented in figure IV.16. The measured Outdoor external dose rates in air at 1 m above ground level that are due to the activity concentrations of ^{238}U. ^{232}Th. and ^{40}K are listed in Table IV.7.
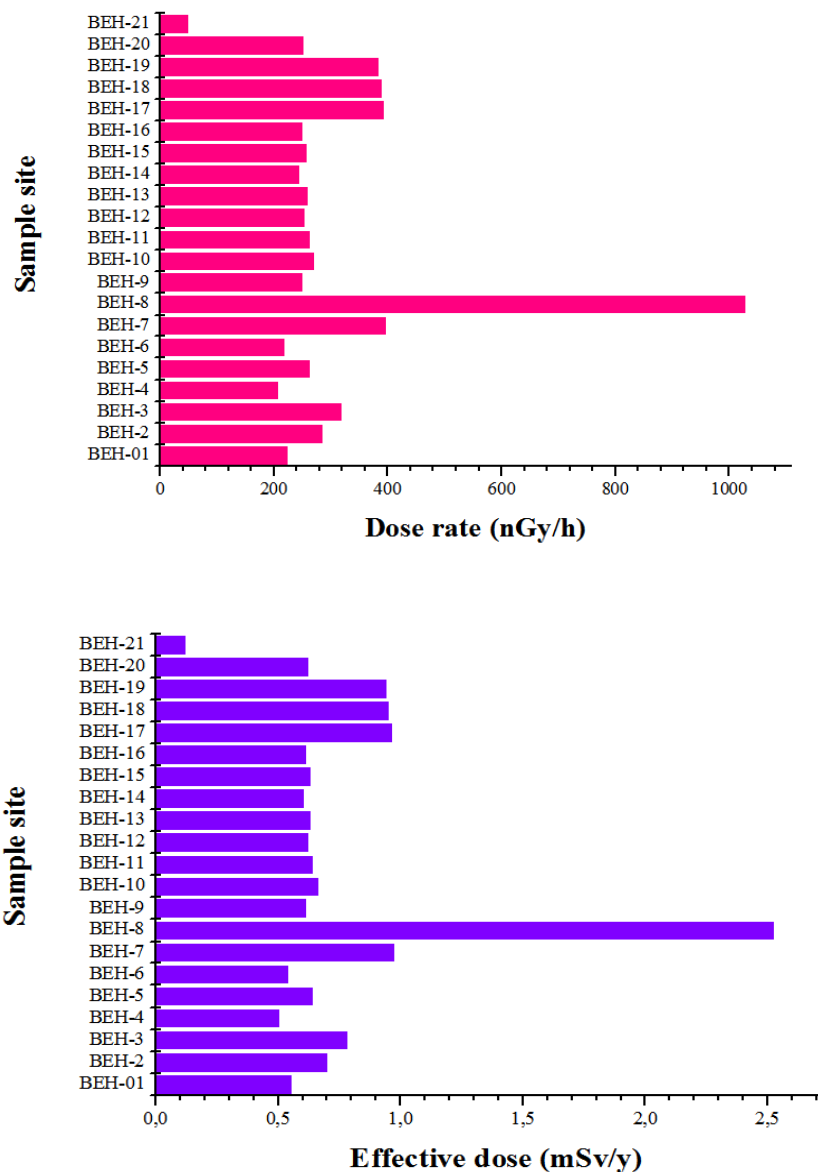
Figure IV.16: hazards distribution in BEH open pit mine

The results range from 49 ± 3 to 1026 ± 75 nGy·h^{-1} with an average dose of 307 ± 79 nGy·h^{-1}. According to UNSCEAR. the world dose rate average value is 59 nGy·h^{-1}.

This shows that the average value for the present study is higher than the world average value reported by UNSCEAR especially for BEH-8 which represents 17 times the world average value.

The Annual effective dose from external exposure to gamma rays received by the workers is calculated using equations (IV.4).

For our 21 samples. the Annual effective dose outdoor values displayed in Table IV.7 vary between 0.12 ± 0.04 and 2.52 ±0.18 mSv/y with an average of 0.75 ± 0.19 mSv/y. All values are higher than the world average value of 0.08 mSv/y given in the report of UNSCEAR [58.59].

Table IV.7. outdoor external dose (D). Annual effective dose (E) from Bled El-Hadba deposit

	D (nGu/h)			E mSv/y		
BEH-1	222	±	14	0.55	±	0.03
BEH-2	284	±	18	0.70	±	0.04
BEH-3	317	±	21	0.78	±	0.05
BEH-4	206	±	13	0.50	±	0.03
BEH-5	262	±	18	0.64	±	0.04
BEH-6	218	±	14	0.54	±	0.03
BEH-7	395	±	28	0.97	±	0.07
BEH-8	1026	±	75	2.52	±	0.18
BEH-9	249	±	16	0.61	±	0.04
BEH-10	270	±	18	0.66	±	0.04
BEH-11	262	±	17	0.64	±	0.04
BEH-12	253	±	16	0.62	±	0.04
BEH-13	258	±	17	0.63	±	0.04
BEH-14	244	±	16	0.60	±	0.04
BEH-15	257	±	16	0.63	±	0.04
BEH-16	249	±	16	0.61	±	0.04
BEH-17	392	±	26	0.96	±	0.06
BEH-18	389	±	26	0.95	±	0.06
BEH-19	382	±	26	0.94	±	0.06
BEH-20	251	±	16	0.62	±	0.04
BEH-21	49	±	3	0.12	±	0.04
Mean	307	±	79	0.75	±	0.19

This exceedance in these sites is due to the high concentration of radionuclides. The results obtained in this investigation are closely similar to those of Pakistan/ Hazara phosphate deposit. The average outdoor external dose rate and the effective dose were found to be respectively (276 ±94) and (0.85± 0.29) as reported by Tufail et al. [41].

IV.6. Statistical approach

The statistical analysis of the activity concentrations of natural radionuclides was processed using free statistical software JASP 0.14.1. for Windows. The method of univariate and multivariate statistics involving cluster analysis and Pearson correlation were applied to deal with the analytical data in terms of their distribution. In addition. correlations between the obtained statistical data were brought to sight in an attempt to identify potential relationships - between pairs of the studied parameters. and to determine the origin of the phosphate samples.

IV.6.1. Basic statistics

The statistical analysis for the measured data was performed using JASP software [70-72] and is featured in Table 5 which includes the ranges (max-min). arithmetic standard deviation (SD). median. skewness. and kurtosis for the radionuclides for the bulk of 21 phosphate samples.

Table IV. 8. Statistical characteristics of radioactive variables BEH phosphate deposit.

Descriptive statistics	^{40}K	^{235}U	^{238}U	^{232}Th	^{226}Ra
Valid	21	21	21	21	21
Mean	81	51	788	65	570
Standard deviation	41	42	643	15	387
Skewness	1.1	3	3	-2	3
Kurtosis	0.4	16	17	5	13
Minimum	35	7	133	14	82
Maximum	176	229	3475	85	2114

According to the obtained results. all the radionuclides exhibit positive skewness values which is an indication of an asymmetric distribution except for Thorium which shows a negative skewness.

Negative value for the skewness of Th (-2) indicates that the peak of the distribution is left of the mean value [64, 65]. Furthermore. potassium and thorium have a positive kurtosis which indicates relatively peaked distribution whereas higher kurtosis values ranging from 13 to 17

were found for Uranium and Radium. The data sets showing high kurtosis values tend to have heavy tails and outliers [66].

IV.6.2. Histograms

The density distribution of the radioactive elements particularly in phosphate deposits. is not clear in the existing literature.
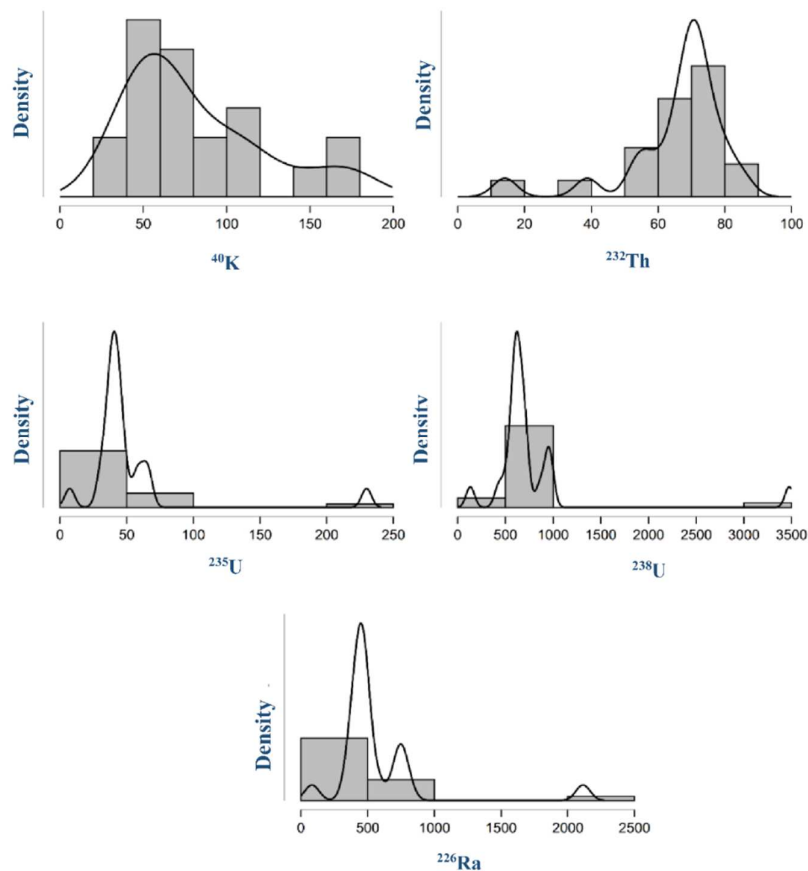
Figure IV.17. Density distribution of the radioactive variables in BEH phosphate deposits.

The density distribution for all radioactive variables in phosphate samples were analyzed. as illustrated by the histograms given in Figure V.16.

The graph of ^{40}K shows that radionuclides demonstrate a normal (bell-shape) distribution. But ^{238}U and ^{232}Th. ^{235}U and ^{226}Ra exhibited some degree of multi-modality. This multi-modal feature of the radio elements observed may be attributed to complicating influence of geological factors

IV.6.3. Pearson's correlation coefficient analysis

Correlation analysis has been carried out. as a bi-variation statistic in order to determine the mutual relationships and strength of association between pairs of variables through calculation of the linear Pearson correlation coefficient.

Results for Pearson correlation coefficients between all the studied radioactive variables are shown in Table.6. high positive correlation coefficient was absorbed between ^{226}Ra **-** ^{238}U. ^{238}U - ^{235}U and ^{235}U- ^{226}Ra This implies that very strong relationship between Uranium family in phosphate.

The variation of ^{238}U content appears to be generally correlated by the variation of ^{235}U (r =0.993). moderate positive correlation was found between uranium and thorium ($\sim$0.25). and between uranium and potassium ($\sim$0.2). Loose correlation was detected between potassium and thorium ($\sim$0.07).

Table IV.9. Pearson's correlation coefficients between radioactive variables BEH phosphate deposit.

Variable	^{40}K	^{238}U		^{226}Ra		^{235}U	^{232}Th
^{40}K	1						
^{238}U	0.231	1					
^{226}Ra	0.201	0.978	***	1			
^{235}U	0.199	0.993	***	0.990	***	1	
^{232}Th	0.078	0.254		0.261		0.253	1

* p < .05. ** p < .01. *** p < .001

For the sake of better visualizing multiple relationships between radioelements. a series of scatter variation diagrams for the studied radioelements were drawn and illustrated in Figure IV.18.

Relatively good correlations were observed between ^{238}U. ^{235}U and ^{226}Ra in BEH phosphate. However. almost all of the scatter plots between U-series and other variables are relatively noisy.

The strong correlations that were observed between the activities indicate that the individual result for anyone of the radionuclide concentration in each pair is a good predictor of the concentration of the other and that they have the same origin [73].
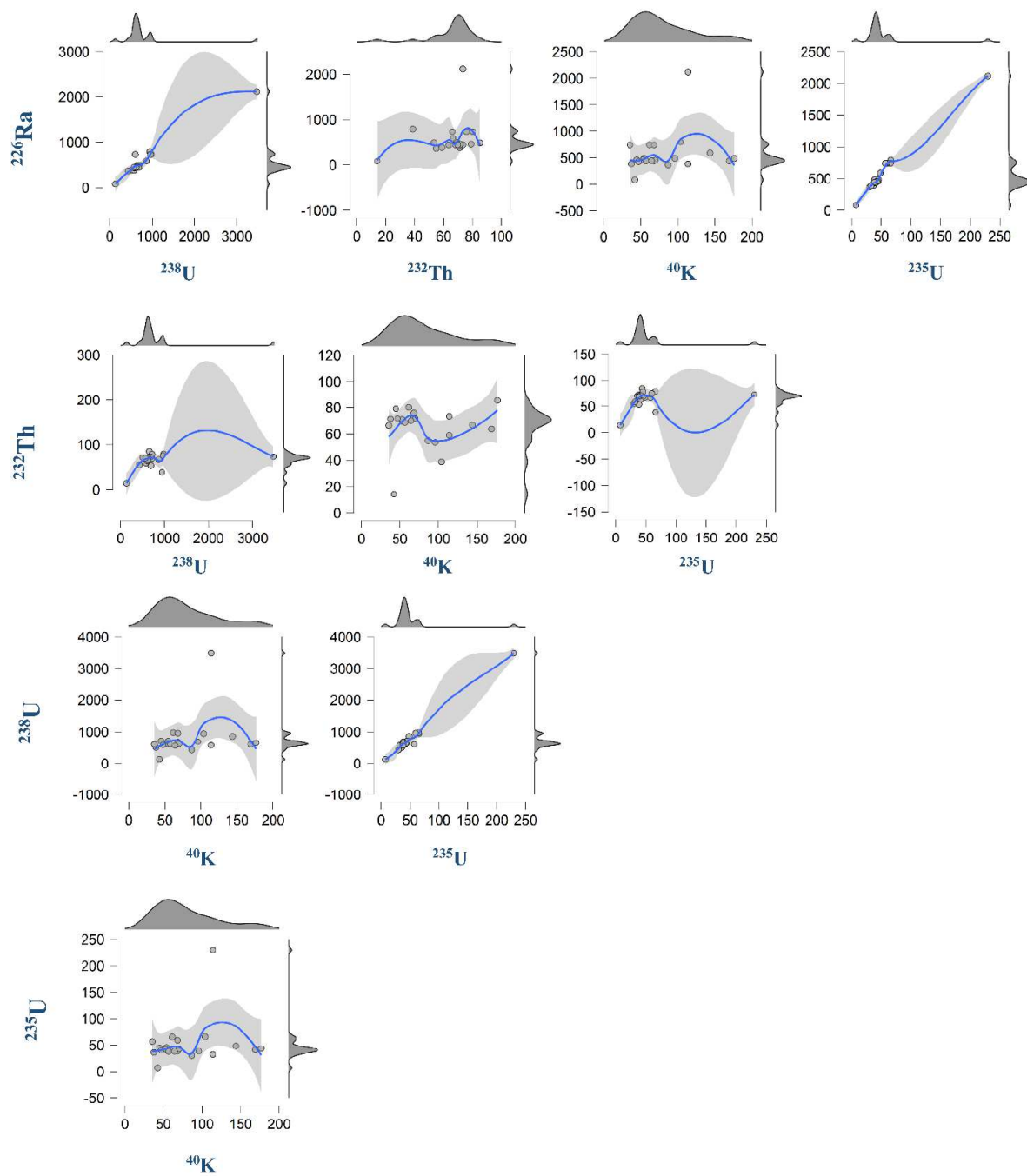
Figure IV.18. Scatter variation diagrams of radioelements in BEH phosphate deposits.

IV.6.4. Hierarchical Cluster Analysis (HCA)

Cluster analysis (CA) is one of the multivariate techniques used in identifying and classifying groups with similar features in a new group of observations [74].

Cluster analysis was carried out through axes in order to identify similar characteristics among natural radioisotopes in BEH phosphate deposits (Figure IV.19). It was also meant to investigate the statistical dependencies between sampling points in different geological formations (Figure V.20).
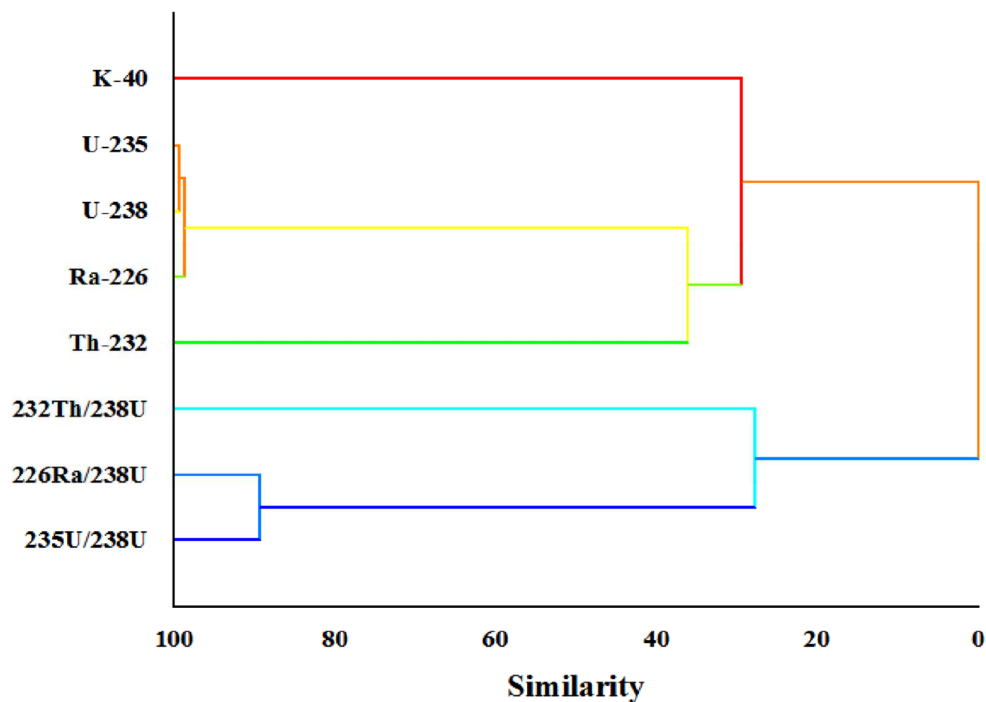
Figure IV.19. Dendrogram showing the clustering of radionuclides and their ratios for BEH phosphate.

As shown in the dendrogram of Figure V.19. all 8 parameters were grouped into two statistically significant clusters. The first group includes $^{235}U/^{238}U$. $^{226}Ra/^{238}U$. $^{232}Th/^{238}U$ activity ratios and the relationships within this group appear to be weak.

The second group is formed by the variables ^{235}U. ^{238}U. ^{226}Ra. ^{232}Th. ^{40}K (activities). It is divided in three sub-groups. one including ^{235}U. ^{238}U. ^{226}Ra and the relationships within this sub-group seem to be strong. When considering also potassium and thorium. the relationships within the group become loose.
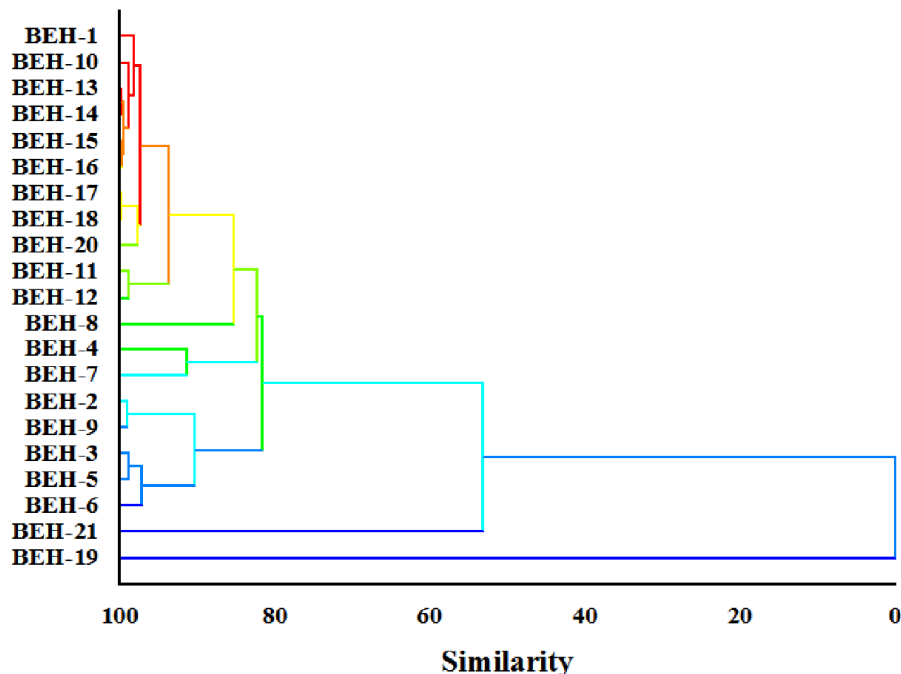
Figure IV.20. Dendrogram showing the clustering of geological features for BEH phosphate deposits.

Moreover. in this dendrogram (Figure V.20). the 21 sampling sites are grouped into two clusters according to the nature of the sedimentary phosphate layer where they occur. The first group encloses BEH-19 belonging to the phosphate limestone. This sample is considered as an outlier since it exhibits a radium concentration higher than that of uranium [75].

The second group is formed by subgroups indicating the similarity of samples which belong to the same phosphate layer. BEH-08 is represented as an outlier. which has the highest values for U-series to which are grafted sites belonging to the phosphate limestone layer that exhibit a high value for the U or Th. The similarity between these points is in fact related to the high radioelements' content [76].

Conclusion

      With increased computational power, Monte Carlo simulations of detector systems have increasingly become an alternative or complement to experimental efficiency calibrations. In this work, we locally developed a reliable computational procedure suitable for the routine analysis by gamma spectrometry of large samples usually encountered in environmental applications. A mathematical model for a HPGe detector has been created and refined using the general MC Code (MCNP5). Different factors and parameters affecting the model accuracy have been investigated. The two factors which found to have the main effect and which could be used to adjust and refine the model are the thickness of the dead layer of the detector and its hole depth. An approach for model refinement is considered. The approach depends on the variation of detector response with respect to dead layer thickness and hole depth of the detector. The nominal dimensions of the detector were optimized using point sources (^{241}Am, ^{137}Cs, and ^{60}Co, ^{133}Ba, and ^{152}Eu). By adjusting the dead- layer and hole length, the discrepancy between experimental and simulated efficiencies is $\leq 3\%$, in average, in the photon energy range of 50–1836 keV for point source and extended source. This verifies that the procedure is effective in building simulation model of the gamma spectrometer using a p-type HPGe detector. Subsequently, the geometric model developed was validated by comparison between the calculated efficiency obtained and the experimental measurements using mixed standard source. The optimized model could be used to accurately determine the radioelement activity for the environmental monitoring.

      As future perspective, the results will be incorporated into our Genie2000 software, which is employed for routine counting of environmental samples. MCNP5 takes into consideration all physical processes involved Y-ray detection, including coincidence summing. Thus, we expect that by employing a proper combination of available simulation programs, we should be able to make accurate determinations of radioactivities present in any material in any counting geometry, without recourse to radioactive standards

      The optimized detector was used to compute efficiency with accuracy in order to generate a first of its kind pre-mining database for the new exploited Algerian phosphate deposit of Bled El-Hadba. A total 21 samples were collected from different geological facies layers and measured for NORMs using a High purity Germanium detector. The quantified activity concentrations of primordial radioelements in these samples recorded an average level of

significance from the radioactivity point of view. The obtained data revealed that the main radioactivity content is due to ^{238}U series. Due to the chemical complexes that Uranium forms with phosphate, phosphate deposits enclose uranium natural radioactivity levels higher than its background one. The present study reveals that the highest concentrations of Uranium-series were found in the phosphate limestone (top layer of the deposit) caused by the increase in the spread of P_2O_5. Otherwise, our results are typically lower, comparable, or higher than most of the data reported by the literature worldwide. The geological features of the worldwide deposits are the main reason for the occurrence of high specific activities.

The mapping of background radioactivity measurements in this work can be used for the development and future integration of a national radiological map for radiation distribution. Activity ratios were evaluated to serve as sensitive indicators of sedimentary processes or environments. From the obtained result no anthropogenic pollution by radiation was detected.

Radiological hazard of the NORM in the BEH phosphate deposites was evaluated on the basis of models for radiation dose calculation. The Outdoor external dose and the associated annual effective dose Outdoor were found to be higher than the world average value reported by UNSCEAR and this is mainly due to higher concentrations of ^{226}Ra and ^{232}Th in phosphate samples or also attributed to the geology of the study area. consequently, the high occupational radiation exposure for workers involved in mining industry must be examined periodically. Radiological hazard can be controlled through protective measures.

This study demonstrates the usefulness of multivariate statistical analysis in the characterization of BEH deposit. From the statistical approach, the distribution of ^{226}Ra, ^{238}U, ^{235}U, and ^{232}Th with multimodality shows the complexity characteristic of sedimentary phosphate. The Pearson's correlation coefficient analysis suggested that strong correlation exists between uranium series and in good agreement with thorium. Significant positive correlation was found between radioelement distribution and the type of sediment layers. According to the obtained results, it seems clear that BEH phosphate deposit has the lowest activity levels of exploited phosphate deposits of sedimentary origin in northern Africa and relatively the minimum radiological dose and environmental impacts through processing. The study provides a detailed statistical evaluation coupled to radionuclide distribution mapping that should allow a sound and safe management and exploitation of BEH mining field.

References

[1]   M. Taha, H. Tulsidas. Application of UNFC to phosphate rock-uranium resources: A case study of the el-sebaeya projects, Nile valley, Egypt, In: Application of the United Nations Framework Classification for Resources: Case Studies, United Nations, 2020, pp. 18-28.   https://doi.org/10.18356/ae5e7da5-en

[2]   H. Rogner, R.F. Aguilera, R. Bertani, C. Bhattacharya, M.B. Dusseault, L. Gagnon, V. Yakushev, Energy resources and potentials, in: Global Energy Assessment: Toward a Sustainable Future, Cambridge: Cambridge University Press, 2012, pp. 425-512. https://doi.org/10.1017/CBO9780511793677.013

[3]   A.E. Ulrich, E. Schnug, H.M. Prasser, E. Frossard. Uranium endowments in phosphate rock. Science of the total environment. 478 (2014) 226-234. https://doi.org/10.1016/j.scitotenv.2014.01.069

[4]   D. Boumala, C. Mavon, A. Belafrites, A. Tedjani, J.E. Groetz. Evaluation of radionuclide concentrations and external gamma radiation levels in phosphate ores and fertilizers commonly used in Algeria. Journal of Radioanalytical and Nuclear Chemistry, 317(1) (2018) 501-510. https://doi.org/10.1007/s10967-018-5871-8

[5]   N. Benabdeslam, N. Bouzidi, F. Atmani, R. Boucif, A. Sakhri. The Effect of the Parameters of the Grinding on the Characteristics of the Deposit Phosphate Ore of Kef Es Sennoun, Djebel Onk-Tébessa, Algeria. International Journal of Materials and Metallurgical Engineering, 12(7) (2018) 319-326. https://doi.org/10.5281/zenodo.1317342

[6]   H. Mezghache, A. Toubal, T. Bouima. Typology of Phosphate Ores in Deposits of the Djebel Onk Mining Basin (Eastern Algeria). Phosphorus Research Bulletin, 15 (2004) 5-20. https://doi.org/10.3363/prb1992.15.0_5

[7]   M. Dass Amiour, H. Mezghache, B. Elouadi. The use of three physico-chemical methods in the study of the organic matter associated with the sedimentary phosphorites in Djebel Onk Basin, Algeria. Arabian Journal of Geosciences, 6(2) (2013) 309-319. https://doi.org/10.1007/s12517-011-0381-9

[8]   S. Chinnaesakki, S. Bara, S. Sartandel, R. Tripathi, V. Puranik. Performance of HPGe gamma spectrometry system for the measurement of low level radioactivity. Journal of Radioanalytical and Nuclear Chemistry, 294(1) (2012) 143-147. https://doi.org/10.1007/s10967-011-1607-8

[9]   IAEA, Radiation protection and management of NORM residues in the phosphate industry, Safety Reports Series N°78., Vienna, 2013

[10]   B. Zohuri. Nuclear fuel cycle and decommissioning. In Nuclear Reactor Technology Development and Utilization, 2020, pp. 61-120. Woodhead Publishing.. https://doi.org/10.1016/B978-0-12-818483-7.00002-0

[11]   A. El-Taher, S. Makhluf. Natural radioactivity levels in phosphate fertilizer and its environmental implications in Assuit governorate, Upper Egypt, 2010.

[12]   C. Lakehal, M. Ramdhane, A. Boucenna. Natural radionuclide concentrations in two phosphate ores of east Algeria. Journal of environmental radioactivity, 101(5) (2010) 377-379. https://doi.org/10.1016/j.jenvrad.2010.02.008

[13]   Y. Sui, R. Ding, H. Wang. A novel approach for occupational health and safety and environment risk assessment for nuclear power plant construction project. Journal of Cleaner Production, 258 (2020) 120945. https://doi.org/10.1016/j.jclepro.2020.120945

[14]   A.S. Rood, H.A. Grogan, H.J. Mohler, J.R. Rocco, E.A. Caffrey, C. Mangini, J. Cartwright, T. Matthews, C. Shaw, M.E. Packard, J.E. Till. Use of Routine Environmental Monitoring Data to Establish a Dose-based Compliance System for a Low-level Radioactive Waste Disposal Site. Health Physics, 118(1) (2020) 1-17. https://doi.org/10.1097/hp.0000000000001116

[15]   J. B. Neris, D.M.M. Olivares, C.S. Santana, P.C. Emenike, F.G. Velasco, S.F.R. Andrade, C.M. Paranhos,. HERisk: An improved spatio-temporal human health risks assessment software. Science of the Total Environment, 772 (2021) 145044. https://doi.org/10.1016/j.scitotenv.2021.145044

[16]   A. Bollhöfer, A. Beraldo, K. Pfitzner, A. Esparon, C. Doering. Determining a pre-mining radiological baseline from historic airborne gamma surveys: A case study. Science of the total environment, 468 (2014) 764-773. https://doi.org/10.1016/j.scitotenv.2013.09.001

[17]   A. Azbouche, M. Belamri, T. Tchakoua. Study of the germanium dead layer influence on HP (Ge) detector efficiency by Monte Carlo simulation. Radiation Detection Technology and Methods, 2(2) (2018) 1-6. https://doi.org/10.1007/s41605-018-0074-y

[18]   A. Azbouche, M. Belgaid, H. Mazrou. Monte Carlo calculations of the HPGe detector efficiency for radioactivity measurement of large volume environmental samples. Journal of environmental radioactivity, 146 (2015) 119-124.

[19]   T. Azli, Z. Chaoui. Performance revaluation of a N-type coaxial HPGe detector with front edges crystal using MCNPX. *Applied Radiation and Isotopes*, 2015, vol. 97, p. 106-112.

[20]   J. Rodenas, , Pascual, A., Zarza, I., Serradell, V., Ortiz, J., & Ballesteros, L. (2003). Analysis of the influence of germanium dead layer on detector calibration simulation for environmental radioactive samples using the Monte Carlo method. *Nuclear Instruments and Methods in Physics Research Section A: Accelerators, Spectrometers, Detectors and Associated Equipment*, *496*(2-3), 390-399.

[21]   Sang, T. T., Chuong, H. D., & Tam, H. D. (2019). Simple procedure for optimizing model of NaI (Tl) detector using Monte Carlo simulation. *Journal of Radioanalytical and Nuclear Chemistry*, *322*(2), 1039-1048.

[22]   Abd El Gawad, K., Zhijian, Z., & Hazzaa, M. H. (2020). Improving the analysis performance of gamma spectrometer using the Monte Carlo code for accurate measurements of uranium samples. *Results in Physics*, *17*, 103145.

[23]   Conti, C. C., Salinas, I. C. P., & Zylberberg, H. (2013). A detailed procedure to simulate an HPGe detector with MCNP5. *Progress in Nuclear Energy*, *66*, 35-40.

[24]   Ba, V. N., Thien, B. N., & Loan, T. T. H. (2021). Effects of element composition in soil samples on the efficiencies of gamma energy peaks evaluated by the MCNP5 code. *Nuclear Engineering and Technology*, *53*(1), 337-343.

[25]   Knoll, Glenn F. Radiation detection and measurement. John Wiley & Sons, 2010.

[26]   Tsoulfanidis, Nicholas, and Sheldon Landsberger. Measurement & detection of radiation. CRC press, 2021.

[27]   Abbasi, F., Nabbi, R., Pooth, O., & Thomauske, B. (2016). Monte Carlo based modeling and simulation of neutron flux distribution and activity map of the German research reactor FRJ-2 (No. RWTH-2016-04096). Fachgruppe für Rohstoffe und Entsorgungstechnik.

[28]   Azbouche, Ahmed. Développement d'une méthodologie d'analyse par spectrométrie gamma et par activation neutronique pour l'étude de la distribution des radio-traceurs et des terres rares dans le sol. Diss. USTHB, 2015.

[29]   Evans, Robley D. "The Atomic Nucleus. McGraw-Hill." New York 19552 (1955): 785-793.

[30]   JB Birks: The Theory and Practice of Scintillation Counting Pergamon Press. 1964, 662 , 16× 23cm, 7,200 .20.5 (1965): 373-374.

[31]   Davisson, C. M. "Interaction of γ-radiation with matter." Alpha-, beta-and gamma-ray spectroscopy. Elsevier, 1968. 37-78.

[32]   Tyler, A. N. (1994). Environmental influences on gamma ray spectrometry (Doctoral dissertation, University of Glasgow).

[33]   Verma, Hem Raj. Atomic and nuclear analytical methods. Springer-Verlag Berlin Heidelberg, 2007.

[34]   R. Kechiched, R. Laouar, O. Bruguier, S. Salmi-Laouar, L. Kocsis, D. Bosch, H. Larit. Glauconite-bearing sedimentary phosphorites from the Tébessa region (eastern Algeria): Evidence of REE enrichment and geochemical constraints on their origin. Journal of African Earth Sciences, 145 (2018) 190-200. https://doi.org/10.1016/j.jafrearsci.2018.05.018

[35]   N. Bezzi, D. Merabet, N. Benabdeslem, H. Arkoub. (2001). Caracterisation physico-chimique du minerai de phosphate de Bled El-Hadba—Tébessa. In Annales de Chimie Science des Matériaux, 26(6) (2001) 5-23. No longer published by Elsevier.

[36] R. Kechiched, R. Laouar, O. Bruguier, S. Laouar-Salmi, O. Ameur-Zaimeche, A. Foufou. Preliminary data of REE in Algerian phosphorites: a comparative study and paleo-redox insights. Procedia Engineering, 138 (2016) 19-29. https://doi.org/10.1016/j.proeng.2016.02.048

[37] L. Visse. Genesis of the southeasterly Algerian–Tunisian phosphatic deposits, in: XIX International Geological Congress set 1, no. 27, Algiers, Algeria, 1952, pp. 60.

[38] I. Galfati, A.B. Sassi, A. Zaier, J.L. Bouchardon, E. Bilal, J.L. Joron, S. Sassi. Geochemistry and mineralogy of Paleocene-Eocene Oum El Khecheb phosphorites (Gafsa-Metlaoui Basin) Tunisia. Geochemical Journal, 44(3) (2010) 189-210. https://doi.org/10.2343/geochemj.1.0062

[39] N. Bezzi, T. Aïfa, D. Merabet, J.Y. Pivan. Magnetic properties of the Bled El-Hadba phosphate-bearing formation (Djebel Onk, Algeria): Consequences of the enrichment of the phosphate ore deposit. Journal of African Earth Sciences, 50(2-4) (2008) 255-267. https://doi.org/10.1016/j.jafrearsci.2007.09.019

[40] R. Rebbah, J. Duarte, O. Djezairi, M. Fredj, J.S. Baptista. A tunnel under an in-pit mine waste dump to improve environmental and landscape recovery of the site. Minerals, 11(6) (2021) 566. https://doi.org/10.3390/min11060566

[41] M. Tufail, M. Asghar. Hazard of NORM from phosphorite of Pakistan. Journal of Hazardous Materials, 176 (1-3) (2010) 426-433. https://doi.org/10.1016/j.jhazmat.2009.11.047

[42] I. Gaafar, A. El-Shershaby, I. Zeidan, L.S. El-Ahll. Natural radioactivity and radiation hazard assessment of phosphate mining, Quseir-Safaga area, Central Eastern Desert, Egypt. NRIAG Journal of Astronomy and Geophysics, 5(1) (2016) 160-172. https://doi.org/10.1016/j.nrjag.2016.02.002

[43] M. Azouazi, Y. Ouahidi, S. Fakhi, Y. Andres, J.C. Abbe, M. Benmansour. Natural radioactivity in phosphates, phosphogypsum and natural waters in Morocco. Journal of Environmental Radioactivity, 54(2) (2001) 231-242. https://doi.org/10.1016/S0265-931X(00)00153-3

[44] P.O. Ogunleye, M.C. Mayaki, I.Y. Amapu. Radioactivity and heavy metal composition of Nigerian phosphate rocks: possible environmental implications. Journal of environmental radioactivity, 62(1) (2002) 39-48. https://doi.org/10.1016/S0265-931X(01)00149-7

[45] A. Aksoy, M. Ahmed, W. Matter, Z. El-Naggar. Gamma-ray spectroscopic and PIXE analysis of selected samples from the phosphorite deposits of Northwestern Saudi Arabia. Journal of radioanalytical and nuclear chemistry, 253(3) (2002) 517-521. https://doi.org/10.1023/a:1020450310197

[46] A.K. Sam, E. Holm. The natural radioactivity in phosphate deposits from Sudan. Science of the total environment, 162(2-3) (1995) 173-178. https://doi.org/10.1016/0048-9697(95)04452-7

[47] T. Akyüz, S. Akyüz, A. Varinlioglu, A. Kose. Radioactivity of phosphate ores from Karatas-Mazidag phosphate deposit of Turkey. Journal of Radioanalytical and Nuclear Chemistry, 243(3) (2000) 715-718. https://doi.org/10.1023/A:1010678521556

[48] A. Ghadeer, A. Ibrahim, M.S. Al-Masri. Geochemistry of uranium and thorium in phosphate deposits at the Syrian coastal area (Al-Haffah and Al-Qaradaha) and their environmental impacts. Environmental Geochemistry and Health, 41(5) (2019) 1861-1873. https://doi.org/10.1007/s10653-018-0221-x

[49] J. A. D Santos Junior, R. D. S. Amaral, J. D. Bezerra, K. F. R. Damascena, C.M. Silva, J. V. M. D. Oliveira, R. C. B. Bispo, E. A. Rocha. 232 Th/238 U in a uranium mobility estimate in an agricultural area in the municipality of Pedra-Pernambuco-Brazil, in: international nuclear atlantic conference, Brazil, October 24-28, 2011.

[50] Z. H. Fernandez, J.A.D. Santos Junior, R.D.S. Amaral, J.M.D.N. Santos, K.F.R. Damascena, N.V.D.S. Medeiros, A.A.D. Silva. Study of the uranium availability through the research method Th/U, in: international nuclear atlantic conference, Brazil, October 4-9, 2015.

[51] N.G. Grozeva, J. Radwan, C. Beaucaire, M. Descostes. Reactive transport modeling of U and Ra mobility in roll-front uranium deposits: Parameters influencing 226Ra/238U disequilibria. Journal of Geochemical Exploration, (2022), https://doi.org/10.1016/j.gexplo.2022.106961

[52] M. Condomines, O. Loubeau, P. Patrier. Recent mobilization of U-series radionuclides in the Bernardan U deposit (French Massif Central). Chemical Geology, 244(1-2) (2007) 304-315. https://doi.org/10.1016/j.chemgeo.2007.06.020

[53] M. Sattouf. Identifying the origin of rock phosphates and phosphorus fertilisers using isotope ratio techniques and heavy metal patterns, doctoral dissertation, Braunschweig Techn, 2007. https://doi.org/10.24355/dbbs.084-200709180200-0

[54] Fujikawa, Y., Fukui, M., Sugahara, M., Ikeda, E., & Shimada, M. (2000). Variation in Uranium Isotopic Ratios 234 U/238U and 235U/total-U in Japanese Soil and Water Samples—Application to Environmental Monitoring. *Proceeding IPRA*, *10*.

[55] Ghadeer, A., Ibrahim, A., & Al-Masri, M. S. (2019). Geochemistry of uranium and thorium in phosphate deposits at the Syrian coastal area (Al-Haffah and Al-Qaradaha) and their environmental impacts. *Environmental geochemistry and health*, *41*(5), 1861-1873.

[56] Snelling, A. A. (2017). Determination of the decay constants and half-lives of uranium-238 (238U) and uranium-235 (235U), and the implications for U-Pb and Pb-Pb radioisotope dating methodologies. Answers Research Journal, 10, 1-38.

[57] El Mamoney, M. H., & Khater, A. E. (2004). Environmental characterization and radio-ecological impacts of non-nuclear industries on the Red Sea coast. Journal of Environmental Radioactivity, 73(2), 151-168.

[58] Al-Hamarneh, Ibrahim. "Radiometric investigation of uranium isotopic ratio in the Jordanian environment." *Dirasat, Pure Sciences* 33.1 (2006): 49-59.

[59] Awudu, A., and E. Darko. "234 U/238 U and 235 U/238 U ratios in domestic water from the environs of Obuasi mine in Ghana." Journal of Radioanalytical and Nuclear Chemistry 287.1 (2011): 129-134.

[60] Olszewski, Grzegorz, Alicja Boryło, and Bogdan Skwarzec. "Uranium (234U, 235U and 238U) contamination of the environment surrounding phosphogypsum waste heap in Wiślinka (northern Poland)." Journal of Environmental Radioactivity 146 (2015): 56-66.

[61] Strumińska-Parulska, D., Olszewski, G., Moniakowska, A., Zhang, J., & Falandysz, J. (2020). Bolete mushroom Boletus bainiugan from Yunnan as a reflection of the geographical distribution of 210Po, 210Pb and uranium (234U, 235U, 238U) radionuclides, their intake rates and effective exposure doses. Chemosphere, 253, 126585.

[62] Długosz-Lisiecka, M., Tyborowski, D., & Krystek, M. (2021). Radioactive fossils: The uranium anomaly and its paleobiological implications. *Chemosphere*, *285*, 131444

[63] Schwarcz, Henry P. "Uranium series dating of Quaternary deposits." *Quaternary International* 1 (1989): 7-17.

[64] K.F. Al-Shboul, A.E. Alali, A.W. Al-Shurafat, A.A. Arrasheed, S.A. Al-Shboul. Spatial evaluation of radionuclide concentrations and the associated radiation hazards using the Kriging method. Journal of Radioanalytical and Nuclear Chemistry, 317(3) (2018) 1285-1297. https://doi.org/10.1007/s10967-018-6015-x

[65] UNSCEAR Sources and Effects of Ionizing Radiation, United Nations Scientific Committee on the Effect of Atomic Radiation, United Nations, New York, 2000.

[66] M. Akpanowo, I. Umaru, S. Iyakwari, E.O. Joshua, S. Yusuf, G.B. Ekong. Determination of natural radioactivity levels and radiological hazards in environmental samples from artisanal mining sites of Anka, North-West Nigeria. Scientific African, 10 (2020) e00561. https://doi.org/10.1016/j.sciaf.2020.e00561

[67] R. Ravisankar, K. Vanasundari, A. Chandrasekaran, A. Rajalakshmi, M. Suganya, P. Vijayagopal, V. Meenakshisundaram. Measurement of natural radioactivity in building materials of Namakkal, Tamil Nadu, India using gamma-ray spectrometry. Applied Radiation and Isotopes, 70(4) (2012) 699-704. https://doi.org/10.1016/j.apradiso.2011.12.001

[68] S.A. Onjefu, S.H. Taole, N.A. Kgabi, C. Grant, J. Antoine. Assessment of natural radionuclide distribution in shore sediment samples collected from the North Dune beach, Henties Bay, Namibia. Journal of radiation research and applied sciences, 10(4) (2017) 301-306. https://doi.org/10.1016/j.jrras.2017.07.003

[69] M. SureshGandhi, R. Ravisankar, A. Rajalakshmi, S. Sivakumar, A. Chandrasekaran, D.P. Anand. Measurements of natural gamma radiation in beach sediments of north east

coast of Tamilnadu, India by gamma ray spectrometry with multivariate statistical approach. Journal of Radiation Research and Applied Sciences, 7(1) (2014) 7-17. https://doi.org/10.1016/j.jrras.2013.11.001

[70] H. Loerts, W. Lowie, B. Seton. Essential statistics for applied linguistics: Using R or JASP, second ed., Red Globe Press, London, 2020.

[71] J. Love, R. Selker, M. Marsman, T. Jamil, D. Dropmann, J. Verhagen, E.J. Wagenmakers. JASP: Graphical statistical software for common statistical designs. Journal of Statistical Software, 88 (2019) 1-17.

[72] M.J. Blanca, J. Arnau, D. López-Montiel, R. Bono, R. Bendayan. Skewness and kurtosis in real data samples. Methodology, (2013).

[73] G. Bouhila, A. Azbouche, F. Benrachi, M. Belamri. Natural radioactivity levels and evaluation of radiological hazards from Beni Haroun dam sediment samples, northeast Algeria. Environmental Earth Sciences, 76(20) (2017) 1-8. https://doi.org/10.1007/s12665-017-7061-3

[74] A.M.A. Adam, M.A.H. Eltayeb. Multivariate statistical analysis of radioactive variables in two phosphate ores from Sudan. Journal of environmental radioactivity, 107 (2012) 23-43. https://doi.org/10.1016/j.jenvrad.2011.11.021

[75] M.M. Makweba, E. Holm. The natural radioactivity of the rock phosphates, phosphatic products and their environmental implications. Science of the Total Environment, 133(1-2) (1993) 99-110. https://doi.org/10.1016/0048-9697(93)90115-M

[76] A. Shahrokhi, M. Adelikhah, S. Chalupnik, T. Kovács. Multivariate statistical approach on distribution of natural and anthropogenic radionuclides and associated radiation indices along the north-western coastline of Aegean Sea, Greece. Marine Pollution Bulletin, 163 (2021), 112009. https://doi.org/10.1016/j.marpolbul.2021.112009

APPENDIX

MCNP Input file

```
c     Created on: Sunday, February 07, 2021 at 15:59
   1     1   -5.32 ((1 -8 -5 ):(8 -6 -7 ):-9 )
   2     0         (1 -2 -100 ):(-200 1 -3 ):-300
   4     0         (35 -25 -29 )#1 #2
   3     1   -5.32 (1 -10 -5 2 ):(10 2 -12 -100 ):(10 -5 11 -8)
             (8 14 -6 -7 ):(-9 15 8 (14 :7 )):(100 3 -48 -200)
   5     0         (22 -23 1 -16 ):(23 -24 -16 17 )
             (23 -24 -18 19 ):(23 -24 -20 21 )
   6     2  -2.702 (35 25 -26 -37 ) $Al
   7     5    -1.6 (-25 -28 29 ) $epoxy
   8     0         (-25 28 -37 ):(37 -26 -31 ) cover
   9     3   -0.93 ((26 -33 30 -32 ):(-26 31 -32 ))
  10     4   -1.18 (-41 -38 40 32 ):(32 -43 -39 )
             (40 -39 -42 43 )
  11    10   -1.56 43 -46 -40  $ ech
  12     6 -0.0012 (-39 42 -44 ):(-40 46 -42 )
  13     4   -1.18 (41 -45 -38 39 ):(-45 44 -39 )
  14     8  -7.287 (49 -1 60 -52 ):(60 1 -61 -62 )
             (1 62 -53 -58 ):(63 -58 53 -54 ):(64 -65 -54 )
  15     7   -8.96 (49 -61 55 -60 ):(55 61 -56 -57 ): $cu
Shielding
             (57 -62 -50 61 ):(62 -50 58 -54 ):(-54 50 -64 )
  16     9  -11.34 (49 -1 52 -53 ):(53 -54 49 -63 )
  17     9  -11.34 (65 -51 -54 )
  18     0         -34 #1 #2 #3 #4 #5 #6 #7 #8 #9 #11 #10 #12
#13 #15 #14 #16
                 #17
  19     0         34

   1         pz 0
   2         cz 0.6
   3         pz 5.1
   5         cz 3.025
   6         pz 6.1


  10         pz 0
  11         cz 2.725
  12         cz 0.8
  14         pz 6.085
  15         tz 0 0 5.6 2.525 0.2 0.2
  47         tz 0 0 5 0.5 0.3 0.3
  48         pz 5.3
```

```
16          pz 5.85   $Elec 1 Top
17          pz 5.72   $Elec 1 int
18          pz 4.45   $Elec 2 Top
19          pz 3.59   $elec 2 int
20          pz 1.66   $Elec 3 top
21          pz 0.79   $elec 3 int
22          cz 3.075  $vide 1
23          cz 3.155  $start elec (int)
24          cz 3.345  $fin electrode (ext)
25          cz 3.845  $int casing Al
26          cz 3.995  $ext casing Al
28          pz 6.65   $ epoxy window top
29          pz 6.6  $top int casing Al
37          pz 6.65  $top ext casing Al
30          pz 5.4
31          pz 6.68
32          pz 6.78
33          cz 4.095
34          so 85
35          pz -0.5
38          cz 4.15  $external
39          cz 4.025  $interna medium
40          cz 4  $internal
41          pz 8.5
42          pz 9.45
43          pz 6.88
44          pz 9.5
45          pz 9.6
46          pz 8.7
49          pz -11.4
50          pz 40.6
51          pz 52.05
52          cz 6.05
53          cz 13.95
54          cz 23.95
c     Cu
55          cz 5.83
56          pz 0.26  $cu
57          cz 13.69  $cu int
58          pz 40.44  $cu up
c     tin
60          cz 5.99
61          pz 0.1  $tin
62          cz 13.85  $tin int
63          pz 40.34  $tin up
64          pz 40.76  $Cu cover
65          pz 40.86  $tin cover

mode   p
```

```
m1     32000.                    1    $Ge
m2     13000.                    1    $Al
m3     1000.           0.66662   $plastic cover
       6000.           0.33338
m4     6000.              0.5    $petrie
       1000.              0.5
m5     6000.                1    $carbon epoxy
m6     8000.              0.3    $air
       7000.              0.7
m7     29000.               1    $Cu
m8     50000.               1    $sn
m9     82000.               1    $Pb
m10    15000.            0.125   $phosphate beige
       8000.            0.432 6000.              0.016 16000.
0.0124
       20000.            0.35 12000.            0.0048 26000.
0.00267
       13000.          0.00218 11000.          0.00778 19000.
0.00083
       14000.          0.00863 1000.            0.0025 9000.
0.037
imp:p      1 18r            $ 1, 18
sdef   cel=11   rad= d1  ext=d2  axs= 0 0 1  par=2    erg= 0.059
si1 0 1
si2 6 7
f8:p  1
e8 0 1e-4  1024i  1.85
cut:p  j 0.01
nps 100000000
```

Valorizations

The scientifique contribution of the work carried out during the period of this thesis can be divided into two part papers and communication

Internationals Publications

- **S. BENAROUS**, A. AZBOUCHE, B. BOUMEHDI, S. CHEGROUCHE, N. ATAMNA, R. KHELIFI. Establishing a pre-mining baseline of natural radionuclides distribution and radiation hazard for the Bled El-Hadba sedimentary phosphate deposits (North-Eastern Algeria). Nuclear engineering and technology journal. https://doi.org/10.1016/j.net.2022.06.006.
  - **S. BENAROUS**, A. AZBOUCHE, R. KHELIFI. Monte Carlo simulation of measurement parameters to improve the accuracy of P-type HPGe gamma spectrometry for environmental application, (**In progress**).

International Communications

- **BENAROUS Samiha**, AZBOUCHE Ahmed, ADDALI Sabah El Houda, MELZI Zaida, ARABI Azzedine, CHEGROUCHE Salah, BOUMEHDI Boualem, KHELIFI Rachid. Gamma Spectrometry Versus Instrumental Neutron Activation Analysis (INAA) Accuracy in the Analysis of Uranium and Thorium content in Algerian Phosphate deposits. 3 INTERNATIONAL GOBEKLITEPE SCIENTIFIC STUDIES CONGRESS. 17-18 december 2021/ şanliurfa.

- **BENAROUS Samiha**, AZBOUCHE Ahmed, CHEGROUCHE Salah, ARABI Azzedine, MELZI Zaida, BOUNEMIA Louisa, BOUMEHDI Boualem, MELIKCHI Radouane, AMARA Bessam, BENCHAABANE Mounia, KHELIFI Rachid. Investigation of Cd and Major/Trace Elements contents in Algerian Phosphate deposits using EDXRF: Intercomparaison with Instrumental Neutron Activation Analysis INAA. 3. INTERNATIONAL GOBEKLITEPE SCIENTIFIC STUDIES CONGRESS. 17-18 december 2021/ şanliurfa.

- M. Benchabane, A. Azbouche, L. Bounemia, S. Chegrouche, B. Boumehdi, B. Amara, Z. Melzi, **S. BENAROUS**, A. Arabi, R. Melekchi, Minors and trace elements distribution in phosphate deposits using X-ray fluorescence, XIV. International Conference on Nuclear Structure Properties, NSP2021 2-4 June 2021, Selcuk University, Konya, Turkey.

- ADDALI Sabah El Houda, AZBOUCHE Ahmed, **BENAROUS Samiha**, CHEGROUCHE Salah, AMARA Bessam, BOUMEHDI Boualem, MELZI Zaida, ARABI Azzedine, MELIKCHI Radouane, BOUNEMIA Louisa, BENCHAABANE Mounia, KHELIFI Rachid. The determination of REEs concentration in Algerian phosphates using Instrumental Neutron Activation Analysis. 3. INTERNATIONAL GOBEKLITEPE SCIENTIFIC STUDIES CONGRESS. 17-18 december 2021/ şanliurfa.

National Communications

•   **BENAROUS, S**, AZBOUCHE.A, CHEGROUCHE.S, BOUNEMIA.L, AMARA.B, BOUMEHDI.B, MELZI.Z, ARABI.A, MELIKCHI.R, BENCHAABANE.M, KHELIFI. R, Occupational health and safety, and environment radiological risk assessment in the Algerian phosphate mining field, presentation Orale au JRSrr'01, au Centre de Recherche Nucléaire de Birine le 16 et 17 Juin 2021.

Others:

- **S. BENAROUS**, A. Azbouche, M. Belamri, A. Hamoudi, B. Morsli, Z. Melzi, Spatial distribution of major, minor and trace element in semiarid land of western Algeria, XIV. International Conference on Nuclear Structure Properties, NSP2021 2-4 June 2021, Selcuk University, Konya, Turkey

- **S. BENAROUS**, A. Azbouche, S.A. Yala, S. Ouarezki, Assessment of Natural and Artificial Radionuclides in Sediment Samples Collected from Two Hypersaline Algerian sites: Chott Melghir and Guelta Al-Hamra, INTERNATIONAL ASIAN CONGRESS ON CONTEMPORARY SCIENCES-V June 1-2, 2021 / Nakhchivan State University, Azerbaijan.

- L. Baba Ahmed, B. Beladel, **S. BENAROUS** (2017). Selenium contents in wheat. Modern Arabic Review of Fundamental & Applied Physics.

- L. Baba Ahmed, M.E.A. Benamar, M. Belamri, A. Azbouche, **S. BENAROUS**, A. Benkhalifa (2018). Natural Radioactivity Levels in Sediments in Algiers Bay using Instrumental Neutron Activation Analysis. Radiochimica Acta. https://doi.org/10.1515/ract-2018-2926.

- Certified training on EDX QUANTX (ED-XRF technique). 2022

- Co-supervision of a master's degree, Option: Radiation Physics. USDB 1. Title: Etude de l'impact radiologique due à la radioactivité naturelle dans le gisement de phosphate de Kef-Essenoun, bassin versant du Djebel Onk.